Modulation-enhanced localization microscopy

Using patterned illumination for super-resolution microscopy: from the localization of single molecules to the description of nano-structures.

Loïc Reymond

TESI DOCTORAL UPF / 2023
Departamento de Medicina y Ciencias de la Vida

THESIS SUPERVISOR
Dr. Verena Ruprecht
Cell and Tissue Dynamics (Cell and Developmental Biology)
The Centre for Genomic Regulation – CRG

THESIS CO-SUPERVISOR
Dr. Stefan Wieser
Super-resolution light microscopy and nanoscopy
The Institute of Photonic Sciences – ICFO

upf. Universitat Pompeu Fabra Barcelona

> Si nous ne trouvons pas des choses agréables, nous trouverons du moins des choses nouvelles.
>
> Voltaire — *Candide ou l'Optimisme*

Funding

I received support from “la Caixa” Foundation (ID 100010434, code LCF/BQ/IN18/11660032) and funding from the European Union’s Horizon 2020 research and innovation programme under the Marie Skłodowska-Curie grant agreement No.713673.

Abstract

This thesis introduces SIMPLE (Structured Illumination based Point Localization Estimator), a novel super-resolution technique in fluorescence microscopy. By combining standing-wave patterned illumination with single-molecule localization microscopy (SMLM), SIMPLE achieves significant improvements in localization precision. Experimental results demonstrate a 2-fold enhancement in localization precision over a 400 μm^2 field of view, validating the practical effectiveness of SIMPLE.

Additionally, this thesis presents meLM (Modulation-Enhanced Localization Microscopy) as a broader concept that encompasses techniques like MINFLUX, SIMPLE, and others. The simulations conducted in this study confirm the theoretical predictions of SIMPLE's improved localization precision throughout the field of view.

Furthermore, the thesis proposes an extension of SIMPLE for direct size measurement of sparse nano-structures, which has the potential to overcome limitations imposed by SMLM. Although actual size measurements have not been performed, this proposal highlights the promising application of SIMPLE in nano-structure sizing experiments.

In summary, SIMPLE demonstrates the power of patterned illumination in advancing super-resolution imaging. The thesis establishes SIMPLE as a key technique within the broader framework of meLM, and suggests its potential for precise nano-sizing experiments.

Resumen

Esta tesis presenta SIMPLE (Estimador de Localización Puntual basado en Iluminación Estructurada), una nueva técnica de superresolución en microscopía de fluorescencia. Al combinar la iluminación con ondas estacionarias patroneadas y la Microscopía de Localización de Moléculas Únicas (SMLM), SIMPLE logra mejoras significativas en la precisión de localización. Los resultados experimentales demuestran un incremento de 2 veces en la precisión de localización sobre un campo de visión de 400 μm^2, validando la efectividad práctica de SIMPLE.

Además, esta tesis presenta meLM (Microscopía de Localización Mejorada por Modulación) como un concepto más amplio que abarca técnicas como MINFLUX, SIMPLE y otras. Las simulaciones realizadas en este estudio confirman las predicciones teóricas de la mejora en la precisión de localización de SIMPLE en todo el campo de visión.

Además, la tesis propone una extensión de SIMPLE para la medición directa del tamaño de nanoestructuras dispersas, lo cual tiene el potencial de superar las limitaciones impuestas por SMLM. Aunque no se han realizado mediciones reales de tamaño, esta propuesta resalta la prometedora aplicación de SIMPLE en experimentos de dimensionamiento de nanoestructuras.

En resumen, SIMPLE demuestra el poder de la iluminación estructurada en el avance de la imagen de superresolución. La tesis establece a SIMPLE como una técnica clave dentro del marco más amplio de meLM y sugiere su potencial para experimentos precisos de dimensionamiento de nanoestructuras.

Résumé

Cette thèse présente SIMPLE (Estimateur de Localisation Ponctuelle basé sur l'Illumination Structurée), une nouvelle technique de super-résolution en microscopie de fluorescence. En combinant une illumination structurée à ondes stationnaires avec la Microscopie de Localisation de Molécules Simples (SMLM), SIMPLE permet d'obtenir des améliorations significatives de la précision de localisation. Les résultats expérimentaux démontrent une amélioration de la précision de localisation de deux fois sur un champ de vision de 400 μm^2, validant ainsi l'efficacité pratique de SIMPLE.

De plus, cette thèse présente meLM (Microscopie de Localisation Améliorée par Modulation) en tant que concept plus large englobant des techniques telles que MINFLUX, SIMPLE, et d'autres. Les simulations réalisées dans cette étude confirment les prédictions théoriques de l'amélioration de la précision de localisation de SIMPLE sur l'ensemble du champ de vision.

En outre, la thèse propose une extension de SIMPLE pour la mesure directe de la taille de nanostructures peu denses, ce qui permettrait de surmonter les limitations imposées par SMLM. Bien que des mesures de taille réelles n'aient pas été effectuées, cette proposition met en évidence l'application prometteuse de SIMPLE dans les expériences de dimensionnement de nanostructures.

En résumé, SIMPLE démontre le pouvoir de l'illumination structurée dans le domaine de l'imagerie de super-résolution. La thèse établit SIMPLE en tant que technique clé dans le cadre plus large de meLM et suggère son potentiel pour des expériences précises de dimensionnement de nanostructures.

Resum

Aquesta tesi presenta SIMPLE (Estimador de Localització de Punts basat en Illuminació Estructurada), una nova tècnica de super-resolució en microscòpia de fluorescència. Mitjançant la combinació d'una il·luminació estructurada amb ones estacionàries i la Microscòpia de Localització de Molècules Úniques (SMLM), SIMPLE aconsegueix millores significatives en la precisió de localització. Els resultats experimentals demostren un increment del doble en la precisió de localització sobre una àrea de visualització de 400 μm^2, validant l'efectivitat pràctica de SIMPLE.

A més, aquesta tesi presenta meLM (Microscòpia de Localització Millorada per Modulació) com a concepte més ampli que engloba tècniques com MINFLUX, SIMPLE i altres. Les simulacions realitzades en aquest estudi confirmen les prediccions teòriques sobre la millora en la precisió de localització de SIMPLE a tota l'àrea de visualització.

A més a més, la tesi proposa una ampliació de SIMPLE per a la mesura directa de les dimensions de nanoestructures disperses, la qual cosa té el potencial per superar les limitacions imposades per SMLM. Encara que no s'han realitzat mesures reals de les dimensions, aquesta proposta posa de manifest l'aplicació prometedora de SIMPLE en els experiments de mesura de nanoestructures.

En resum, SIMPLE demostra el poder de la il·luminació estructurada en l'avanç de la imatge de super-resolució. La tesi estableix SIMPLE com una tècnica clau dins del marc més ampli de meLM i suggereix el seu potencial per a experiments de mesura precisa de dimensions de nanoestructures.

Contents

List of Acronyms xv

List of Symbols xvii

I Fundamentals in Optical Microscopy 1
- I.1 Introduction . . . 1
- I.2 The resolution . . . 3
- I.3 Fluorescence . . . 5

II Super-resolution optical microscopes 9
- II.1 Modelling the fluorescent signal . . . 9
- II.2 Total internal reflection fluorescence . . . 11
- II.3 Stimulated emission-depletion . . . 13
- II.4 Structured illumination microscopy . . . 16
- II.5 Single-molecule localization microscopy . . . 23

III SIMPLE – SIM-based Point Localisation Estimator 27
- III.1 Point emitters in patterned illumination . . . 30
- III.2 Illumination's properties . . . 31
  - III.2.1 Patterns/Signal summation . . . 31
  - III.2.2 Homogeneity criterion . . . 33
  - III.2.3 m-b_o equivalence . . . 33
  - III.2.4 Pixel integration . . . 34
  - III.2.5 Homogeneous phase-shifts $\xi = 1$ . . . 35
  - III.2.6 Reduced-amplitude phase-shifts $\xi < 1$ . . . 38
- III.3 Localisation precision limits . . . 40

III.3.1 Uncertainty propagation (UP) 41
Homogeneous phase-shifts – $\xi = 1$ 42
Reduced phase-shifts – $\xi < 1$ 44
III.4 Cramér-Rao lower bound (CRLB) 45
III.4.1 The Fisher information matrix (FIM) 46
III.4.2 Read-out noise as a Poisson variable 48
III.4.3 Shot-noise as a Gaussian variable 49
III.4.4 A Poisson-Normal mixed model 50
III.4.5 CRLB applied to SIMPLE 50
Equidistant phase-shifts with $\xi < 1$ 51
Homogeneous phase-shifts: $\xi = 1$ 52
Spatial spreading of the fluorescence 54
III.4.6 Comparison of localization precision limits 58
III.5 Numerical simulations 59
III.5.1 Model/simulation comparison 64
Homogeneous phase-shifts with $K = 3$ 64
High-gain SIMPLE: $\xi < 1$ 70

IV Perspective: patterned illumination for nano-sizing **73**
IV.1 From individual emitters to sparse nano-structures . . . 76
IV.1.1 Emitter pair 76
IV.1.2 Complex structures 82

Conclusion **87**

Appendices

A SIMPLE: Structured illumination based point localization estimator with enhanced precision **93**

B Modulation-enhanced localization microscopy **107**

C Structured illumination microscopy **121**

Bibliography **131**

List of Figures

I.1 Diffraction-limit 4
I.2 eGFP's emission & absorption spectra 5
I.3 Fluorescence - Jablonski diagram 6

II.1 TIRF illumination 12
II.2 TIRF image sequence 14
II.3 Stimulated emission-depletion (STED) 16
II.4 Moiré patterns 18
II.5 TIRF-SIM 19
II.6 3D-SIM 19
II.7 Illumination pattern 20
II.8 Structured illumination microscopy (SIM) 21
II.9 Localisation precision limit - Thompson vs Mortensen . . 24

III.1 MINFLUX 27
III.2 SIMPLE – single emitter in 2D standing-wave illumination 28
III.3 Principle of SIMPLE 29
III.4 Pixelation effects on SIM images 34
III.5 Emitter's phase position retrieval 37
III.6 Signal amplitude at fixed N – Peak and valley 38
III.7 Illumination and pixel grid's coordinates 54
III.8 SIMPLE with spatial spreading 55
III.9 Image simulation workflow 61
III.10 Binning masks 61
III.11 SIMPLE - Fitting routine 62
III.12 SIMPLE - Localisation precision and gain 65

III.13 Spatial dependency of the localization precision 67
III.14 SIMPLE - Effect of noise 68
III.15 SIMPLE - The effect of the modulation 69
III.16 High-gain SIMPLE - Spatial dependency 71

IV.1 Pixel vs vector based images 75
IV.2 $\{A \times m \times \phi\}$-space 77
IV.3 Centroid wiggling of an emitter pair 79
IV.4 $\{A \times m \times \phi\}$ dependency on emitters pair's distance . . 80
IV.5 Schematic of a neural network 81
IV.6 Pseudo-vectorial description of complex structures . . . 83

List of Tables

III.1 Phase position uncertainty for three evenly-spaced phase shifts 58
III.2 Average and limit phase uncertainty for three evenly-spaced phase shifts 59

List of Codes

III.1 Localization precision calculation using uncertainty propagation (UP) 45
III.2 SIMPLE simulation pipeline – MATLAB 63

List of Acronyms

NA	numerical aperture
CRLB	Cramér-Rao lower bound
DMD	digital micro-mirror device
FIM	Fisher information matrix
FOV	field of view
GFP	green fluorescent protein
GSD	ground-state depletion
GT	ground truth
HiLo	highly inclined and laminated optical sheet
LLS	lattice light-sheet
LS	least-square
meLM	modulation-enhanced localization microscopy
MINFLUX	minimal photon fluxes
ML	machine-learning
NN	neural network
OM	optical microscopy
OTF	optical transfer function
PALM	photoactivated localization microscopy
PDF	probability density function
PINN	physics-informed neural network
PSF	point-spread function
RESOLFT	reversible saturable/switchable optical linear fluorescence transitions
RMS	root-mean-square

ROI	region of interest
SIM	structured illumination microscopy
SIMPLE	SIM based localization estimator
SLM	spatial-light modulator
SMLM	single-molecule localization microscopy
SNR	signal-to-noise ratio
SPT	single-particle tracking
SR	super-resolution
SRM	super-resolution microscope
STD	standard deviation
STED	stimulated emission-depletion
STORM	stochastic optical reconstruction microscopy
TIRF	total internal reflection fluorescence
TWINZ	twinkle-wiggle nano-sizer
UP	uncertainty propagation
WF	widefield

List of Symbols

	Description	Unit	Range
A	Illumination pattern's amplitude		$\mathbb{R}_+$
a	Pixel size	nm	meLM
b_o	Background offset	$\varphi_{/\text{px}}$	$\mathbb{R}_+$
$\mathcal{J}$	Bessel $\mathcal{J}$ function	meLM	meLM
$\Delta_\bullet$	Uncertainty of the quantity $\bullet$	$[\bullet]$	
δ	Kronecker delta function	meLM	meLM
δL	Pattern shift: $\delta\psi \cdot \lVert\boldsymbol{\ell}\rVert^{-1}$	nm	meLM
$\delta\psi$	Pattern phase shift	rad	meLM
η	Intensity of fluorescence	φ	$\mathbb{N}$
$\mathcal{F}$	Fourier transform's operator	–	meLM
$\mathcal{G}$	Precision gain	–	$\mathbb{R}_+$
$\mathcal{N}$	Normal/Gaussian distribution		
$\mathcal{H}_{\text{PSF}}$	Integrated point-spread function	–	$\mathbb{N}^d \to [0, 1]$
h_{PSF}	Point-spread function	–	$\mathbb{R}^d \to [0, 1]$
$\mathbf{I}$	Fisher information matrix		
$\mathcal{I}$	Illumination function		$\mathbb{R}^d \to [0, A]$
K	Number of phase shifts: $\Omega(\Theta)$	–	$\mathbb{N}^*$
$\mathbf{k}$	Vector in the reciprocal space	nm^{-1}	meLM
κ	Phase shifts' index	–	$1, \ldots, K$
L	Pattern period	nm	$\mathbb{R}_+$
$\boldsymbol{\ell}$	Coordinate along the pattern	nm^{-1}	meLM
$\mathcal{L}$	Likelihood function		

	Description	Unit	Range
m	Signal's modulation	–	$[0, 1]$
N	Total number of photons	φ	$\mathbb{R}_+$
n	Refractive index	–	$\mathbb{R}_+$
O_{OTF}	Optical transfert function	nm^d	meLM
Ω	Cardinality operator	–	meLM
P	Number of emitters	–	$\mathbb{N}^*$
p	Emitters' index	–	$1, \dots, P$
ϕ	Phase position relative to the illumination	rad	$(-\pi, \pi]$
φ	Unit representing a number of photons	φ	
$\mathcal{P}$	Poisson distribution		$\mathbb{R}_+^* \to \mathbb{N}$
Ψ	Set of phases $\{\psi_\kappa\}$		$(-\pi, \pi]$
ψ	Phase of the illumination pattern	rad	$(-\pi, \pi]$
ψ_0	Pattern's phase at the point $(0, 0)$	rad	$(-\pi, \pi]$
$\mathcal{R}$	Fluorescent response function	φ	$\mathbb{R}_+ \to \mathbb{R}_+$
ρ	Emitters' fluorescence density	nm^{-d}	$\mathbb{R}^d \to [0, 1]$
Σ	Background noise per ROI	φ/px	$\mathbb{R}_+$
$\sigma_\bullet$	Standard deviation of $\bullet$	$[\bullet]$	$\mathbb{R}_+$
σ_b	Background noise per pixel	φ/px	$\mathbb{R}_+$
$\sigma_\odot$	Localisation precision	nm	$\mathbb{R}_+$
ς	Fluorescence signal	φ	$\mathbb{R}^d \to \mathbb{R}_+$
V	Number of frames	–	$\mathbb{N}^*$
T	Number of pattern orientations:	–	$\mathbb{N}^*$
ν	Frame index	–	$1, \dots, V$
τ	Pattern orientation index	–	$1, \dots, T$
Θ	Set of pattern orientations $\{\theta_\tau\}$	–	meLM
θ	Pattern orientation	rad	$[0, 2\pi)$
λ	Excitation/emission wavelength	nm	$\mathbb{R}_+$
$\mathbf{x}$	Position vector	nm	meLM
ξ	Shift factor	–	$(0, 1]$
$\overline{\xi}$	Reduced shift factor	–	$(0, \frac{2\pi}{K}]$

Chapter I

Fundamentals in Optical Microscopy

I.1 Introduction

The invention of the microscope in the 16th century revolutionized our understanding of the natural world by enabling scientists to observe previously unseen structures such as microorganisms, cells, and even individual subcellular components [1–4]. Over the centuries, the development of microscopy has not ceased to transform and extend our knowledge of the biological world.

In the late 19th century, Ernst Abbe formulated the diffraction limit of light, which imposed a fundamental limit on the resolution of conventional fluorescence microscopy [5]. This limit states that objects smaller than half the wavelength of light cannot be resolved. It was only in the 1930s, with the development of electron microscopy, that scientists were able to achieve a resolution beyond the diffraction limit of light. However, electron microscopy requires samples to be fixed, stained, and imaged in a vacuum, making it unsuitable for imaging living cells.

In the 1950s, the invention of the first fluorescence microscope enabled visualization of living cells and tissues [6]. The use of fluorescent dyes and probes allowed researchers to observe specific structures and molecules within cells, such as the cytoskeleton or DNA. The discovery

and use of green fluorescent protein (GFP) in the 1990s marked a major advance in the field [7], enabling the visualization of dynamic processes in living cells, such as protein trafficking and cell division.

The development of confocal microscopy in the 1950s [6, 8] and TIRF microscopy in the 1980s [9] allowed for improved details and image contrast by reducing out-of-focus fluorescence and illuminating only a thin section of the sample, respectively.

Driven by the discovery and use of GFP, the 1990s saw the flourishing of new techniques by-passing Abbe's resolution limit. The invention of stimulated emission-depletion (STED) microscopy [10] provided a significant improvement in resolution by successively using two laser beams to selectively quench fluorescence, effectively narrowing the fluorescent volume and enabling resolution beyond the diffraction limit. Alternatively, single-molecule localization microscopy (SMLM), using the spatio-temporal sparsity of emitters and subsequent fitting routine to achieve high resolution, was proposed by Betzig, Moerner and Orrit [11–14]. And at about the same time, structured illumination microscopy (SIM) was being developed by Gustafsson; relying on Moiré interferences with the illumination's structure, unlocking resolution-doubling in live cells with minimal sample preparation [15].

With each one of these technological advances, researchers are better equipped to observation tissues, cells, sub-cellular structures and even single molecules. This is key to answer many fundamental biological questions and further our understanding of life, hence a direct drive and motivation to push further into breaking the limitations of existing techniques. Towards this ambitious goal, I will present *SIM based localization estimator (SIMPLE)*; a novel technique at the nexus of SIM and SMLM that improves the localisation precision of single molecules by a factor two.

This thesis, presented as a compendium of articles I co-authored [16–18] (listed in appendices A to C), will go through the basic concepts and limitations of conventional microscopes, describe the state-of-the-art super-resolution microscopes, introduce the idea of modulation-enhanced localization microscopy (meLM) focusing on SIMPLE (theory,

simulations & experimental results) and finally overview the potential of this class of techniques as a method for sizing nanometric structures.

I.2 The resolution

Despite its significant capabilities, traditional fluorescence microscopy is limited by the diffraction of light, first described by Ernst Abbe in (1873) [5]*, and commonly known as the *diffraction limit*, which restricts the resolution to around 200–300 nm for visible light, preventing the visualization of structures on the nanoscale. This limit, which was formalised only after Abbe's death [19], imposes that objects smaller than half the wavelength of illumination λ divided by the numerical aperture (NA) cannot be resolved:

$$d_{\text{Abbe}} = \frac{\lambda}{2n\sin\alpha} = \frac{\lambda}{2\text{NA}} \tag{I.1}$$

where Abbe defined the numerical aperture as $\text{NA} = n\sin\alpha$, with n the refractive index of the medium, and α the objective's semi-angular aperture.

It is however a closely related derivative of this limit that is used in practice as measure of resolution in microscopy: the *Rayleigh criterion* [20]:

$$d_{\text{Rayleigh}} = \frac{\mathcal{J}^0_{1,1}}{2\pi}\frac{\lambda}{\text{NA}} \simeq 0.61\frac{\lambda}{\text{NA}} \tag{I.2}$$

where $\mathcal{J}^0_{1,1}$ is the first zero of the Bessel $\mathcal{J}$ function of the first kind.

While these limits are similar, Abbe's equation sets a *limit inherent to the wave-like properties of light*, whereas the Rayleigh criterion is a convenient yet arbitrary limit above which two objects can be distinguished.

*For the English translation of Abbe's original paper and a comprehensive analysis of the historical development of microscopy, see 19.

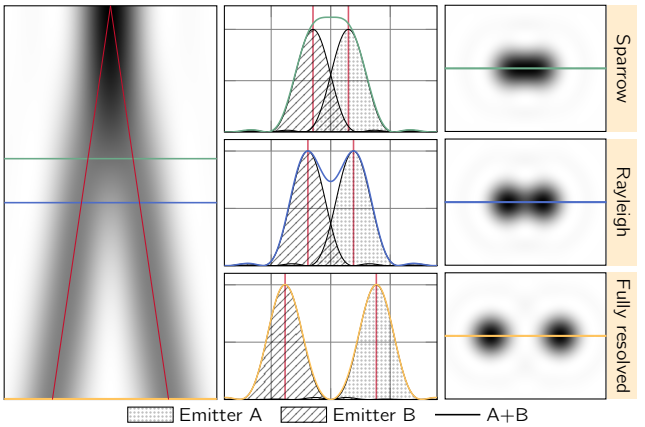

Figure I.1 – *Diffraction-limit: Comparison of the resolution criteria.*

A third resolution measure is defined by Sparrow [21] as the distance cancelling the intensity dip between two point-sources:

$$d_{\text{Sparrow}} \simeq 0.48\frac{\lambda}{\text{NA}} \tag{I.3}$$

This result is obtained assuming that, at the limit, the second derivative of the intensity at the centre of the emitters vanishes. Hence, using the derivation properties of Bessel functions, with $2r = d_{\text{Sparrow}}$, one obtains:

$$\frac{9\mathcal{J}_1(r)^2}{r^2} - \frac{6\mathcal{J}_0(r)\mathcal{J}_1(r)}{r} + \frac{3\mathcal{J}_0(r)^2 - 4\mathcal{J}_1(r)^2 + \mathcal{J}_2(r)^2}{4} = 0 \tag{I.4}$$

Those limits are represented in figure I.1, where one can see that because of the diffraction limit, past a certain distance two objects will merge and become indistinguishable. The case described as "fully resolved" allows the signal to completely vanish between the emitters as they separate by twice the Rayleigh limit [22].

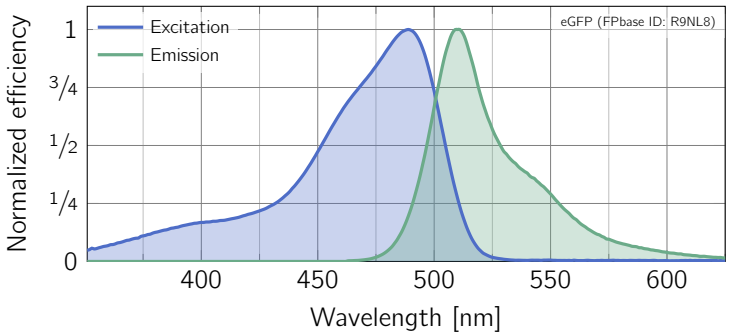

Figure I.2 – *Emission & absorption spectra of eGFP. The peak excitation efficiency is around* 488 nm*, and the fluorescence around* 510 nm*. The Stokes shift is the energy/wavelength difference between the absorbed and emitted light.*

I.3 Fluorescence

One of the key concepts that revolutionized light microscopy and allowed it to play a major role in research is fluorescence. Unlike in bright-field microscopy, where the light is simply shone through the sample, fluorescence enables the selective study of specific sub-parts of a sample. In bright-field microscopy, the whole object is illuminated and the observed signal results from the unspecific light-sample interaction, which limits contrast, resolution, and makes it impossible to study individual structures.

However, with the development of fluorescent dyes and later genetically encoded fluorescent proteins, researchers were able to study specific structures of interest. These fluorescent proteins are produced *in-situ* by the cell and can be specifically attached to a protein complex through genetic manipulation, enabling selective study of individual structures.

Fluorescence is a phenomenon in which a molecule transiently absorbs a photon and then re-emits it at a longer wavelength (see figure I.2). This process involves the molecule transitioning from its ground state (S_0) to an excited (S_n) state upon absorbing a photon. The excited state being unstable, it quickly relaxes back to the ground state, emit-

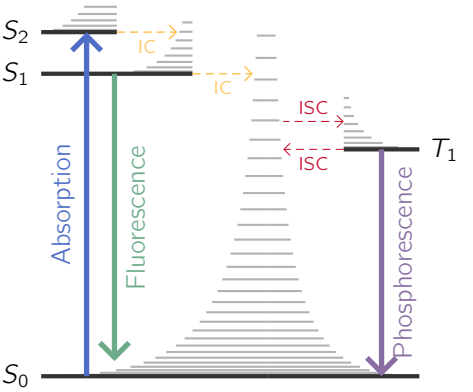

Figure I.3 – *Jablonski diagram of the various energy transfer processes potentially happening in a fluorophore. The fluorescence, and phosphorescence are both radiative transitions, whereas the internal conversion (IC) and inter-system crossing (ISC) are not.*

ting a photon in the process; this emitted light is known as *fluorescence*. Phosphorescence, is a slightly different process where the fluorophore relaxes to a meta-stable state called the triplet-state before a photon is emitted to release the remaining energy acquired.

When in an excited state, the molecule can undergo a process called inter-system crossing, where it transitions from a singlet state (S_n) to a triplet state (T_m): a relatively long-lived, excited state of the molecule. From the triplet state, the molecule can either non-radiatively relax back down to the ground state or undergo a process called phosphorescence, where it emits a photon of even longer wavelength than fluorescence.

Jablonksi diagrams (figure I.3) are often used to visualize the energy level transitions involved in fluorescence. These diagrams show the ground state, excited state, and triplet state of the molecule, as well as the various energy level transitions that can occur, including vibrational relaxation, fluorescence and phosphorescence.

Depending on the stability of the different excited states, the time it takes the fluorophore to relax towards the ground state can vary. This so called fluorescence lifetime typically varies from nanoseconds to mi-

croseconds depending on the fluorophore's chemical structure and the surrounding environment. When taken into account, these dependencies can be used to gain precious insight about the sample [23].

In summary, fluorescence is a powerful tool in microscopy, as it allows specific structures within a sample to be visualized with high sensitivity and specificity. By using fluorophores with distinct spectral properties (*i.e.* excitation and emission wavelengths), multiple structures can be visualized simultaneously in a single sample.

Chapter II

Super-resolution optical microscopes

This chapter's purpose is to present the relevant microscopy modalities necessary for the understanding of the chapters to come. It should give the reader the context and an overall understanding of the state-of-the-art fluorescent microscopes (TIRF, STED, SIM, and SMLM)*.

II.1 Modelling the fluorescent signal

In order to understand the innovative techniques invented to overcome the limitations of the diffraction limit and implemented in STED, SIM, and SMLM, it is first necessary to model the fluorescence signal.

We first define the density of fluorescent emitters attached to a sample's structure of interest as $\rho(\mathbf{x})$. Those fluorophores will then be activated using an excitation illumination; whose spatio-temporal representation is given by $\mathcal{I}(\mathbf{x})$. Furthermore, in order to keep the model as general as possible, one needs to account for the response $\mathcal{R}$ of the emitters to said excitation.

*For an extensive description and comparison of the main techniques used in microscopy, please see the excellent review article L. Schermelleh et al., "A guide to super-resolution fluorescence microscopy", Journal of Cell Biology **190**, 165–175 (2010).

One defines the fluorescent emission η as the product of the emitter's density ρ and the response $\mathcal{R}$ to a given excitation $\mathcal{I}$:

$$\eta(\mathbf{x}) = \rho(\mathbf{x})\,\mathcal{R}\big(\mathcal{I}(\mathbf{x})\big) \tag{II.1}$$

This emission does not yet account for the limited resolution of the microscope, that spreads the signal by convolving it with h_{PSF}, the functional representation of the point-spread function (PSF). One defines the signal ς, as follows:

$$\begin{aligned}\varsigma(\mathbf{x}) &= \Big[h_{\text{PSF}} \otimes \eta\Big](\mathbf{x}) \\ &= h_{\text{PSF}}(\mathbf{x}) \otimes \Big[\rho(\mathbf{x})\,\mathcal{R}\big(\mathcal{I}(\mathbf{x})\big)\Big]\end{aligned} \tag{II.2}$$

Ultimately, this "ideal" signal will be collected by a detector, or detector-array (sCMOS, EMCCD, PMT, SPAD, etc.), effectively integrating the signal over a portion of space. Here, individual detectors' cells of surface $S_{u,v}$ are indexed as u, v:

$$\varsigma_{u,v} = \int_{\mathbf{x}\in S_{u,v}} \varsigma(\mathbf{x})\,\mathrm{d}^2\mathbf{x} \tag{II.3}$$

Finally, in order to obtain a result that models accurately real images, one needs to add noise components [25]:

- Shot-noise (Poissonian distribution $\mathcal{P}(\varsigma)$ coming from the photon-counting process)
- Read-out noise (additive Gaussian noise $\mathcal{N}$, from electronic conversion of the signal)
- Dark-current (random charge-hole creation)
- Pattern noise (pixel-to-pixel variation)

In the scope of the presented work, only the shot-noise and read-out noise are taken into account as one supposes that the dark-current and

pattern noise are either negligible or could experimentally be accounted for.

Furthermore, as a convention, the total number of fluorescence's photons N is defined as the signal collected during a group of V successive excitations of index ν.

$$N = \sum_{\nu=1}^{V} \eta_\nu \tag{II.4}$$

II.2 Total internal reflection fluorescence

Total internal reflection fluorescence (TIRF) is a powerful imaging technique used to investigate the interactions between biological molecules at the interface between two media (figure II.1). Its principle is based on the phenomenon of *total internal reflection*, which occurs when a light beam is incident on the interface between two media with different refractive indices n_1, n_2 at an angle θ_i greater than the critical angle θ_c given by Snell's law:

$$\theta_c = \frac{\sin n_1}{\sin n_2} \tag{II.5}$$

Indeed, above this angle, the reflected beam generates an evanescent field that penetrates only a few hundred nanometres into the sample's medium, allowing the selective excitation –and corresponding detection– of fluorescent molecules in the near-field region, *i.e.* at the sample's interface.

The axial dependency of the evanescent field's intensity is given by the following equation [22, 26]:

$$I(z) = I_0 e^{-z/d} \tag{II.6}$$

The evanescent field decreases exponentially in intensity into the second medium; with a penetration depth d given by the following equation:

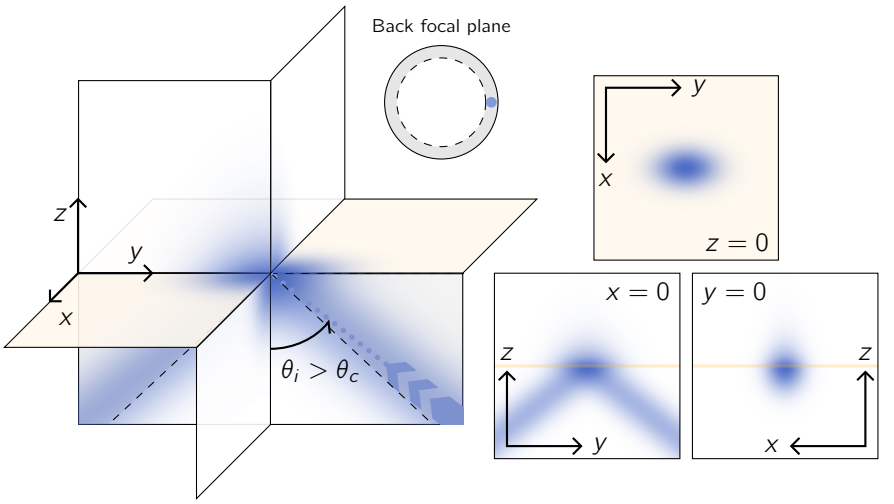

Figure II.1 – *TIRF illumination: For incident angles θ_i greater than the critical angle θ_c, the light is totally reflected. Above the focal plane, only an exponentially-decaying evanescent field (a few hundred nanometres deep) can excite the sample.*

$$d = \frac{\lambda}{4\pi\sqrt{{n_1}^2 \sin^2\theta_i - {n_2}^2}} = \frac{\lambda}{4\pi n_2}\left[\frac{\sin^2\theta_i}{\sin^2\theta_c} - 1\right]^{-1/2} \tag{II.7}$$

where λ is the wavelength of the incident light, n_1 and n_2 are the refractive indices of the first and second media, respectively, and θ_i is the angle of incidence.

Even though usually not considered being a super-resolution technique, one could argue that TIRF offers sub-diffraction information as d can reach values below 50 nm for NA $= 1.7$ objectives, ensuring the very close proximity (much below the standard axial resolution) of the fluorescent molecules.

The first application of total internal reflection microscopy to fluorescence in (1981) was presented by Axelrod [9], who used a prism to generate the evanescent field at the glass-liquid interface [27]. Later, the use of a microscope objectives with a high numerical aperture (NA) (higher than the sample's medium) became the standard method to

achieve TIRF illumination [28].

TIRF has found numerous applications in the study of cell biology [29], including the visualization of the dynamics of cell membrane and cytoskeleton, and used to study the behaviour of single molecules on surfaces. More elaborate implementations have later been proposed improving the techniques by, among others, reducing unwanted signal or bettering illumination homogeneity [30–33].

Figure II.2 shows a time-series of multi-colour TIRF images obtained using a custom-made DMD-based TIRF-SIM microscope I designed and built in-house. The labelled structure are actin (LifeAct-eGFP, greyscale) and myosin (myomCherry, cyan) expressed in a zebrafish progenitor stem cell under a confinement of 7 µm. The images, selected with a 2 s separation, are a subset of a movie acquired at 20 fps with 25 ms exposure time.

II.3 Stimulated emission-depletion

Stimulated emission-depletion (STED) microscopy, a point-scanning technique, was first proposed by Hell and Wichmann in (1994), and the first experimental demonstration of STED microscopy was published in (1999) [34]. Since then, STED microscopy has become a widely used technique in biological imaging, with applications ranging from the study of synapses and neural networks to the imaging of virus particles and intracellular organelles [35–40]. STED microscopy has also been combined with other techniques, such as fluorescence correlation spectroscopy and single-particle tracking, to provide further insights into biological processes at the nanoscale.

The principle of STED microscopy is based on stimulated emission, which is the inverse process of spontaneous emission. Stimulated emission occurs when an excited molecule is stimulated by an additional external photon with the same energy, triggering the radiative relaxation of the excited molecule and the emission of a photon. This process effectively de-activates the molecule and hence reduces the population of

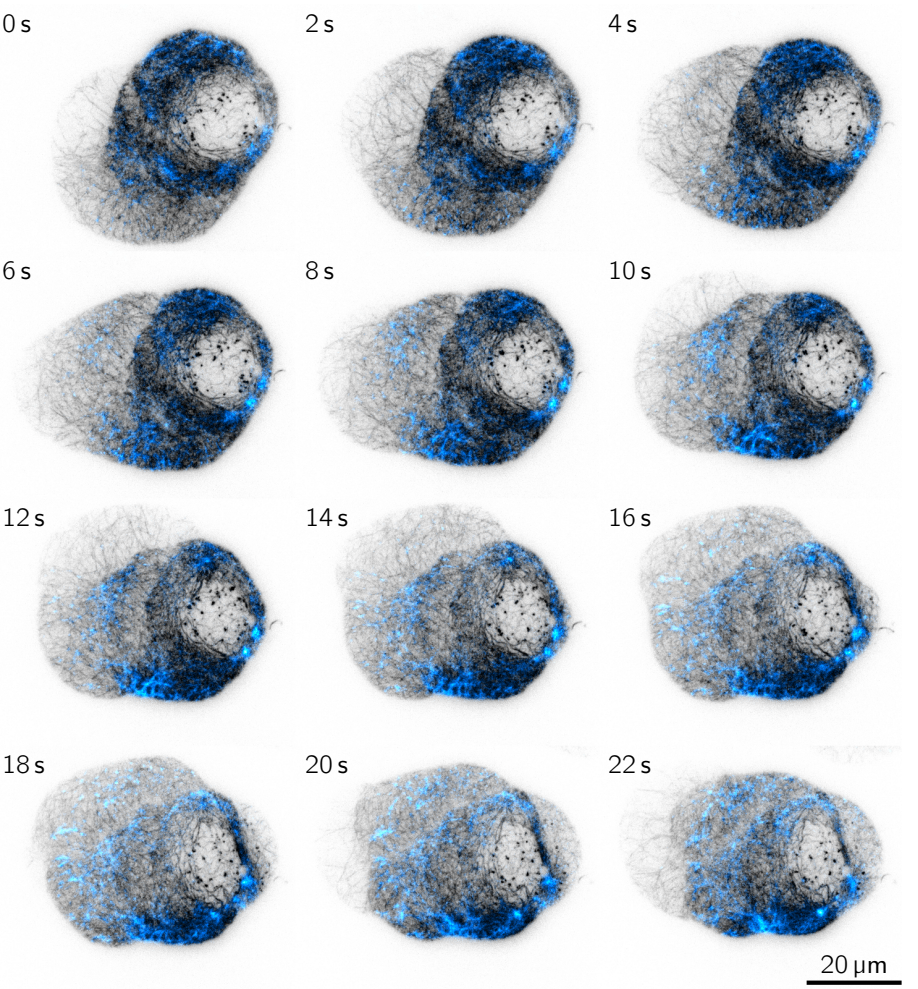

Figure II.2 – *Series of 2-colours TIRF images of a zebrafish progenitor stem cell acquired on a custom build microscope. The cell is confined with a confinement-height of* 7 µm*, and the fluorescently labelled structures are actin (LifeAct-eGFP, greyscale) and myosin (myomCherry, cyan). The displayed images are picked every 40 frames (*2 s*) from a movie acquired at* 20 fps *with* 25 ms *exposure time.*

the excited state, resulting in a localized reduction in the fluorescence emission.

STED microscopy, requires two laser beams to respectively excite and de-excite the fluorophores. The first beam is focused onto the sample, putting fluorophores in an excited state and potentially causing them to fluoresce. The second beam, focused on the same portion of the sample, is spatially modulated into a doughnut-shaped intensity distribution (typically achieved using a phase mask), featuring a central (almost) zero-intensity point. The intensity profile of the second beam is essential as the region with high intensity will have a greater potential for the de-excitation of fluorophores than its dimmer counterparts. The doughnut-shape therefore preserves the signal at its centre but depletes excited fluorophores further away radially, ensuring that the signal comes from a well-defined region at the illumination's centre.

However, as described in section I.2, the achievable resolution of an optical system is fundamentally limited by the diffraction limit, as given by Abbe's formula (I.1). This means that the accuracy with which we can illuminate the sample is constrained by the same limit: both the excitation and depletion beams in STED microscopy are subject to the constraints of diffraction and cannot be arbitrarily small, just like the fluorescent signal. In summary, even though the two laser beams are subject to the diffraction limit, the spot size containing the remaining excited fluorophores can be much smaller.

A visual representation of the excitation, depletion, and effective point-spread function (PSF) can be found in figure II.3.

The intensity of the depletion beam is carefully controlled to achieve the desired resolution improvement, while minimizing the loss of fluorescence signal [37]. The resolution achieved by STED microscopy is given by the formula:

$$d_{\mathrm{STED}} = \frac{\lambda}{2\mathrm{NA}} \frac{1}{\sqrt{1 + I/I_{\mathrm{sat.}}}} \tag{II.8}$$

where $I_{\mathrm{sat.}}$ is the saturation intensity of the fluorophore, and I is the intensity of the depletion beam.

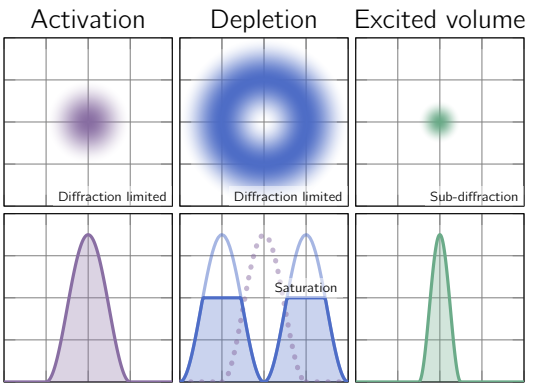

Figure II.3 – *Stimulated emission-depletion (STED): a diffraction limited spot of the sample is first excited (left), then a patterned laser will inactivate the emitters from the edge of this spot (centre), leaving only a restricted portion of the initially active fluorophores able to fluoresce (right). This sub-diffraction spot is called "effective PSF".*

The resolution improvement is proportional to a factor that depends on the ratio of the intensity of the depletion beam and the saturation intensity of the fluorophore [41]. By tuning this ratio, the effective spot size can be made smaller than the diffraction limit, resulting in an increase in resolution down to around 50 nm [42–44]. Finally, this narrow effective-PSF is scanned across the FOV, recording the corresponding signal's intensity.

The STED principle has since been generalised to other types of activation/deactivation not necessarily relying on stimulated depletion – such as reversible saturable/switchable optical linear fluorescence transitions (RESOLFT) or ground-state depletion (GSD)– but the mechanism is similar [45].

II.4 Structured illumination microscopy

Structured illumination microscopy (SIM) is a widefield super-resolution imaging technique that was developed in the late 1990s by Gustafsson

[15]. It is based on the principle of spatial frequency mixing, where a sample is illuminated with a set of sinusoidal patterns (standing waves), resulting in the generation of Moiré interference [46] that contain high-frequency information that is beyond the diffraction limit of conventional microscopy. This information is retrieved by a mathematical reconstruction process typically involving 9 or 15 raw images.

SIM has found widespread use in the field of biology to study a variety of cellular structures and processes. For example, SIM has been used to study the organization of the actin cytoskeleton, the distribution of microtubules and intermediate filaments, and the localization of various proteins and organelles. SIM has also been used to study dynamic processes, such as cell division, vesicle trafficking, and intracellular transport. In addition, SIM has been used in neuroscience to study the morphology and connectivity of neuronal structures, such as dendrites, axons, and synapses. The high spatial resolution and compatibility with live-cell imaging make SIM a powerful tool for studying biological systems at the subcellular level.

SIM can be implemented in 2D ([47–51]) or 3D (figure II.6) [52–56], and has been widely used in the field of biology to study subcellular structures, cellular dynamics, and tissue organization [43, 57–59]. Standard SIM microscopes are limited to a two-fold increase in resolution whereas more advanced implementations, using non-linearity properties (saturation, stimulated depletion, etc.), can reach higher resolutions at the expense of implementation complexity and higher number of frames necessary to reconstruct super-resolution images.

In SIM, a sample is illuminated with a set of spatially modulated patterns generated by interfering two or more laser beams (figure II.6 and figure II.5) [60]. The resulting signal–even though diffraction limited–of the interference between the sample's structure of interest and the known applied illumination pattern encodes usually inaccessible details about the sample. Figure II.4 shows two types of structures (dots and stripes) whose fine details would be lost if imaged directly (see homogeneous grey regions after blurring). However, the super-imposition of this structure with another fine pattern results in large-scale features

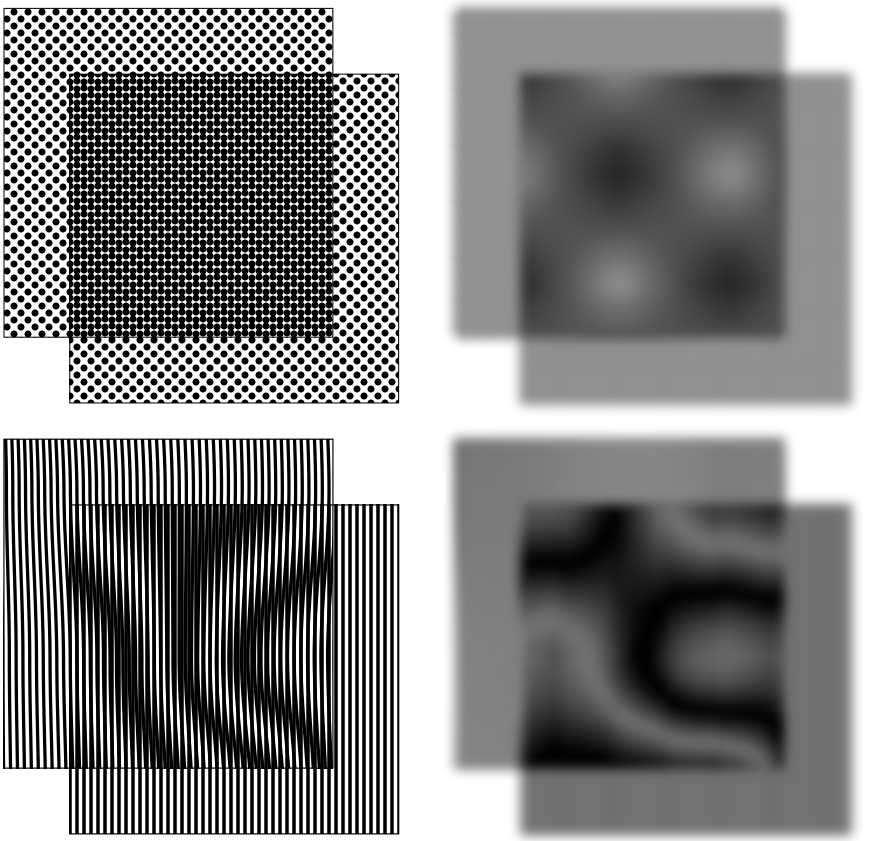

Figure II.4 – *Two different examples of generated Moiré interference: ground truth (left) blurred (right). Dotted pattern with two slightly different periodicity (top). Stripes with minor distortion (bottom).*

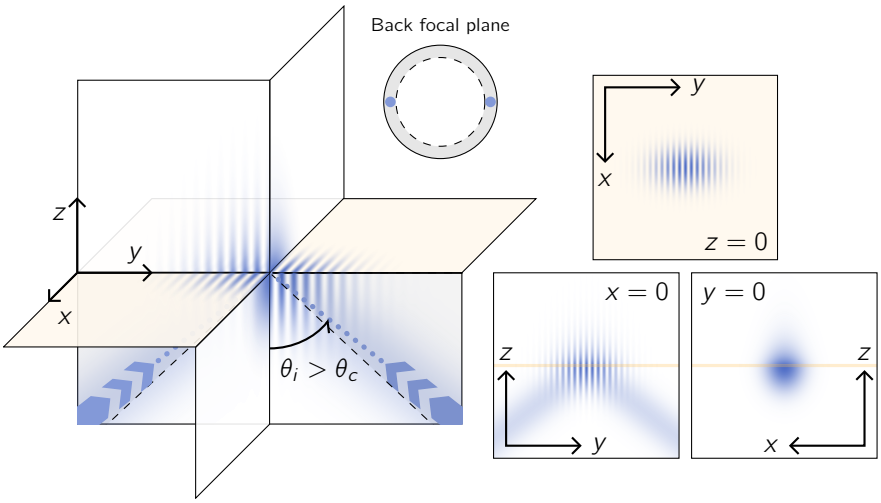

Figure II.5 – *TIRF-SIM: Two beams of equal intensities, oriented in opposite directions, are fully reflected ($\theta_i > \theta_c$) and generate an interference pattern.*

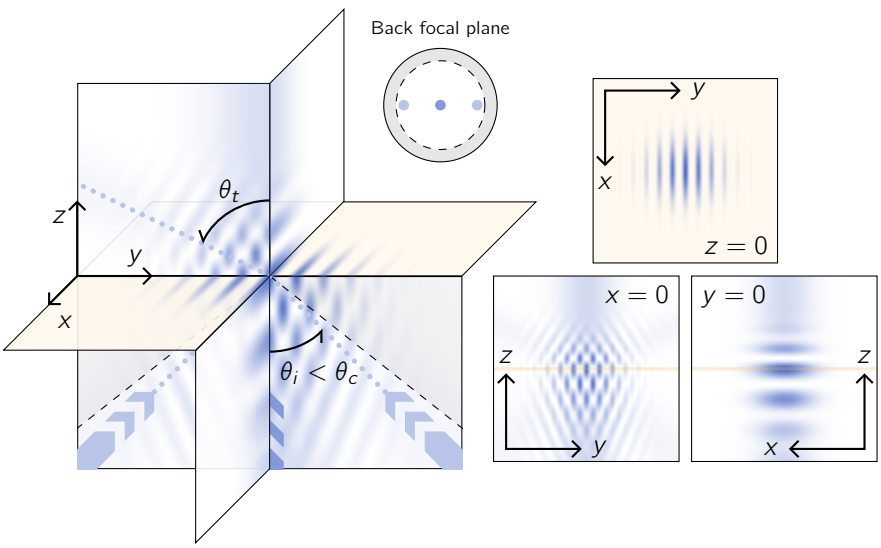

Figure II.6 – *3D-SIM: Three beams (one straight, two oblique) are interfering at the sample's position. The beams' orientation and relative phase can be tuned to generate the right set of typically 15 SIM images.*

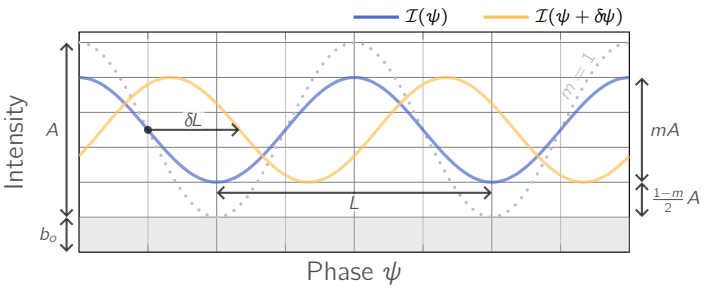

Figure II.7 – *Representation of the sinusoidal illumination $\mathcal{I}$ generated by interfering beams described by equation (II.9). The pattern of period L can be accurately displaced by a known distance δL.*

that are able to be imaged: the high spatial frequencies are shifted towards the standard-resolution frequencies. The subsequent reconstruction process requires a series of these images corresponding to different pattern translations (phase-shifts) and orientations in order to fill homogeneously the now-extended Fourier plane (see figure II.8). This is typically done by applying Fourier analysis to each raw image and combining the resulting frequency-domain information to fill the high-frequency regions of the extended Fourier space. Various algorithms have been developed for this purpose, such as the classical Wiener filter, the maximum likelihood method, iterative reconstruction methods and more recently using machine-learning tools [61–66]. These algorithms aim to minimize nopoisson and artefacts while preserving the fine details of the image.

As detailed in equation (II.2), the fluorescent signal is the product of the emitters' density ρ and the illumination $\mathcal{I}$ convolved with the optical system's PSF. In the case of SIM, the illumination (represented in figure II.7) is assumed to be standing wave described by:

$$\mathcal{I}(\psi) = \frac{A}{2}\Big[1 - m\cos\psi\Big] + b_o \tag{II.9}$$

where A is an amplitude factor converting the emitter's density into signal's intensity, m the modulation depth, ψ is the pattern's phase, and b_o

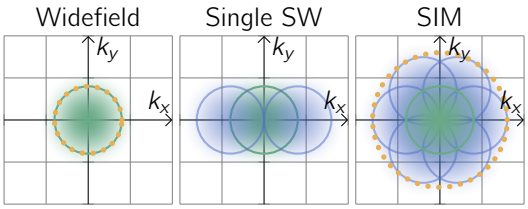

Figure II.8 – *The high spatial frequencies containing the structural details of the sample are cut off by the diffraction limit (left). The standing-wave illumination shifts part of the higher frequency in the transmitted range (centre). By successively rotating the patterned illumination, a quasi-homogeneous filling of the Fourier space can be achieved, effectively doubling the cut-off frequency (right).*

a background offset. The latter has been included for completeness, but will be omitted later on without loss of generality (see section III.2.3). The expressions are simplified using the following definitions:

$$\psi(\mathbf{x}) = \mathbf{x} \cdot \boldsymbol{\ell} - \psi_0 \tag{II.10a}$$

$$\boldsymbol{\ell} = \frac{2\pi}{L} \begin{pmatrix} \cos\theta \\ \sin\theta \end{pmatrix} \tag{II.10b}$$

where ψ,θ, and L respectively denote the pattern's phase, orientation and period. The coordinate along the pattern is designated by $\boldsymbol{\ell}$; further also referred to as $\boldsymbol{\ell}_{\parallel}$ in order to distinguish the parallel ($\boldsymbol{\ell}_{\parallel}$) and perpendicular ($\boldsymbol{\ell}_{\perp}$) components. ψ_0 is the phase at a reference point in the FOV, set for each orientation of the pattern.

The pattern's periodicity reaches its minimal value when:

$$L^{\min} = \frac{\lambda_{ex}}{2\,\mathrm{NA}} \tag{II.11}$$

where λ_{ex} is the excitation wavelength.

From these definitions and in order to understand the shift of high-frequency information towards the lower–and accessible–range, one could look at the Fourier transform $\mathcal{F}$ of the illumination and of the signal (figure II.8):

$$\tilde{\mathcal{I}}(\mathbf{k}) = \delta(\mathbf{k}) - \delta(\mathbf{k}+\boldsymbol{\ell})\frac{m}{2}e^{\mathrm{i}\psi} - \delta(\mathbf{k}-\boldsymbol{\ell})\frac{m}{2}e^{-\mathrm{i}\psi} \tag{II.12}$$

That leads to the following expression for the signal in terms of the optical transfer function (OTF), defined as $O_{\text{OTF}} = \mathcal{F}(h_{\text{PSF}})$:

$$\begin{aligned}
\tilde{\varsigma}(\mathbf{k}) &= O_{\text{OTF}}(\mathbf{k})\,\tilde{\eta}(\mathbf{k}) \\
&= O_{\text{OTF}}(\mathbf{k})\Big[\tilde{\rho}(\mathbf{k}) \otimes \mathcal{F}\big\{\mathcal{R}\big(\mathcal{I}(\mathbf{x})\big)\big\}(\mathbf{k})\Big] \\
&\overset{\mathcal{R}=\mathbb{I}}{=} O_{\text{OTF}}(\mathbf{k})\Big[\tilde{\rho}(\mathbf{k}) \otimes \tilde{\mathcal{I}}(\mathbf{k})\Big] \\
&\overset{\text{(II.9)}}{\propto} O_{\text{OTF}}(\mathbf{k})\Big[\tilde{\rho}(\mathbf{k}) - \frac{m}{2}\tilde{\rho}(\mathbf{k}-\boldsymbol{\ell})e^{\mathrm{i}\psi} - \frac{m}{2}\tilde{\rho}(\mathbf{k}+\boldsymbol{\ell})e^{-\mathrm{i}\psi}\Big]
\end{aligned} \tag{II.13}$$

The end-result of equation (II.13) shows that the periodic illumination effectively duplicates and shifts the frequencies along $\pm\boldsymbol{\ell}$. The phase-dependent factors $e^{\mp\mathrm{i}\psi}$, coming from the relative phase of the illumination, vanish over the series of raw images as the pattern is translated (typically phase-shifted by 0, $\pi/3$, and $2\pi/3$)

Hence, the sample's highest accessible spatial frequency is $\mathbf{k}_{\text{cut-off}} + \boldsymbol{\ell}$, instead of $\mathbf{k}_{\text{cut-off}} = \frac{2\text{NA}}{\lambda_{\text{em}}} = \frac{2\pi}{d_{\text{Abbe}}}$, leading to the expression of the maximum achievable resolution directly depending on the periodicity of the illumination pattern:

$$\begin{aligned}
d_{\text{SIM}} &= \Big[d_{\text{Abbe}}^{-1} + L^{\text{min}}\Big]^{-1} \\
&\overset{\text{(II.11)}}{=} \frac{1}{2\text{NA}}\left[\frac{1}{\lambda_{\text{em}}} + \frac{1}{\lambda_{\text{ex}}}\right]^{-1} = \frac{\lambda_{\text{em}}}{2\left(1 + \frac{\lambda_{\text{em}}}{\lambda_{\text{ex}}}\right)\text{NA}} \\
&\overset{\lambda_{\text{ex}}=\lambda_{\text{em}}}{\Longrightarrow} d_{\text{SIM}} = d_{\text{Abbe}}/2
\end{aligned} \tag{II.14}$$

Due to the Stokes shift, the emission wavelength is longer than the excitation's: $\lambda_{\text{ex}} < \lambda_{\text{em}}$. In the limit case where both wavelengths are equal, one reaches the well-known two-fold resolution increase associated with SIM.

The reduced number of frames necessary for the reconstruction of super-resolved images, the high-speed acquisition, coupled with the low intensity illumination make this technique an ideal candidate for live-cell imaging of dynamic structures around 100 nm [59]. An application-oriented book chapter about this technique [18] explaining the principle, implementations, sample preparation, reconstruction procedure, and artefacts' is provided in appendix C.

II.5 Single-molecule localization microscopy

We have seen that STED and SIM achieve super-resolution using respectively the non-linearity of stimulated-emission and the mathematical properties of Moiré interference. Single-molecule localization microscopy (SMLM) is based on a third, and drastically different concept: the sparsity of emitters.

Indeed, through opto-chemical engineering, one ensures that the active fluorescent molecules tagging a structure are sparse at any given time [11, 13, 14, 67]: buffers can be added to stabilize meta-stable states, delaying the radiative relaxation to the ground state, fluorophores can be photo-activated/deactivated, or fluorescent tags transiently binding to the locus of interest. This allows to express the emitters' density as a sum of punctual sources:

$$\rho(\mathbf{x}) = \sum_p A_p \, \delta(\mathbf{x} - \mathbf{x}_p) \tag{II.15}$$

Using this property jointly with the illumination profile assumed to be homogeneous, the expression of equation (II.2) simplifies as:

$$\begin{aligned} \varsigma(\mathbf{x}) &= h_{\text{PSF}}(\mathbf{x}) \otimes \Big[\rho(\mathbf{x})\, \mathcal{I}(\mathbf{x})\Big] \\ &\overset{\text{(II.15)}}{=} \sum_p h_{\text{PSF}}(\mathbf{x} - \mathbf{x}_p) \cdot \eta_p \end{aligned} \tag{II.16}$$

The signal is therefore described by the sum of diffraction limited

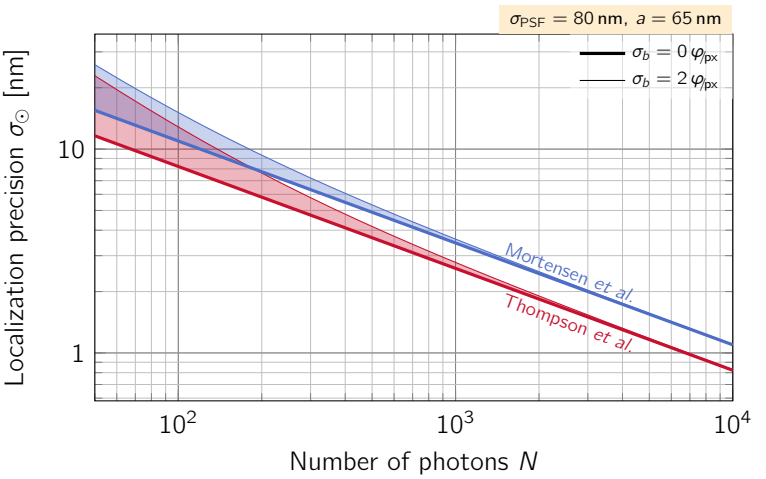

Figure II.9 – *Localisation precision limit according to Thompson et al. [74] and Mortensen et al. [75]. The thick lines correspond to the noiseless read-out, the thin lines assume* $\sigma_b = 2\,\varphi_{/px}$.

spots of intensities η_p. If those spots are far enough one from another, they can be treated individually and, given the functional form h_{PSF} of the PSF, retrieve the source's origin with only a few nanometres accuracy. This process is iterated on a long sequence of images in which a large fraction of the fluorophores will have provided an unambiguous signal.

SMLM describes the process of a whole class of techniques that isolate emitters and reconstructs point-by-point a super-resolution image; such as photoactivated localization microscopy (PALM), stochastic optical reconstruction microscopy (STORM) or other PSF engineering techniques [42, 43, 68–71]. Moreover, a variety of data analysis tools are now available to process and filter the localizations obtained from the raw images of sparse emitters [72, 73].

The absolute limits of this technique, inherent to the statistical randomness of the measuring of the signal (shot-noise), was first theorised by Thompson et al. [74], later by Ober et al. [76] and corrected by Mortensen et al. [75], giving rise to the well-established Mortensen's

formula:

$$\begin{aligned} {\sigma_{\odot}}^2 &= \frac{\sigma_a^2}{N}\left[1+\int_0^1 \frac{\log(t)}{1+t/\tau}\,\mathrm{d}t\right]^{-1} \\ &\simeq \frac{\sigma_a^2}{N}\left[\frac{16}{9}+\frac{8\pi {\sigma_b}^2\sigma_a^2}{a^2\,N}\right] \end{aligned} \tag{II.17}$$

This expression (represented alongside Thompson et al.'s limit in figure II.9) provides a localization precision limit $\sigma_{\odot}$ as a function of N the number of photons, σ_b the background noise per pixel, and σ_a, the corrected PSF accounting for the finite pixel size a: $\sigma_a^2 = \sigma_{\mathrm{PSF}}^2 + \frac{a^2}{12}$. Note that Abbe's diffraction limit expressed in terms of standard deviation

$$\sigma_{\mathrm{PSF}}^{\mathrm{min}} = \frac{\sqrt{2}}{2\pi}\frac{\lambda_{\mathrm{em}}}{\mathrm{NA}} \tag{II.18}$$

The equation (II.17) is crucial to this work and will be systematically taken as localization precision reference and compared to throughout the rest of this thesis.

Chapter III

SIMPLE – SIM-based Point Localisation Estimator

A non-trivial but natural step, aiming at improving current microscopy modalities and relaxing some of their limits, is to combine (part of) existing techniques.

Introduced as minimal photon fluxes (MINFLUX) [77], Balzarotti et al. makes use of the doughnut-shaped illumination –traditionally used in STED– to resolve single molecules with unprecedented precision, breaking the nanometre barrier.

To achieve that, a molecule's fluorescence intensity is recorded over time as the illumination is shifted around it. Initially, the molecule is positioned at the centre of the doughnut where the illumination and the signal are the dimmest. By repeatedly off-centring the excitation with

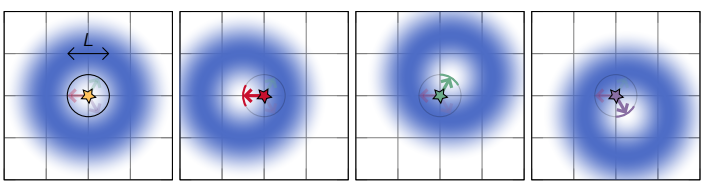

Figure III.1 – *Illustration of the principle of MINFLUX: a doughnut-shaped illumination is displaced around a fluorescent emitter. The change in signal intensity is recorded and the emitter's localization is retrieved through triangulation.*

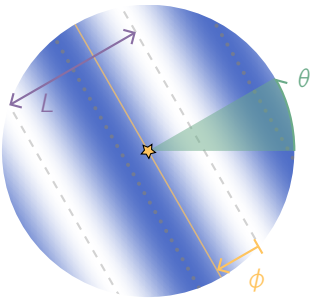

Figure III.2 – *Representation of the illumination parameters: orientation θ, period L and the phase position ϕ of a single emitter with respect to the pattern (closest trough).*

respect to the emitter, the now increasing signal will provide key information about its location (figure III.1). With only a few photons, one can triangulate the position of said molecule with an accuracy $\leq$1 nm.

Unfortunately, this extreme precision comes at the cost of a limited field of view (FOV); the extra information embedded in each received photon comes from the "unlikeliness" of it being emitted, which is confined to the trough of the excitation. MINFLUX's implementations cope with this restriction by fast scanning of the FOV.

In order to mitigate the spatio-temporal restrictions imposed by the doughnut excitation, the proposed approach –SIMPLE– parallelises MINFLUX by using a SIM-like standing-wave illumination in place of STED's doughnut (figure III.2). As a result, the precision gain is limited but generalised to the whole FOV.

The principle of SIMPLE is illustrated in figure III.3: the illumination (blue stripes) is sequentially shifted, and the emitters' intensity varies, driven by the pattern displacement. The fluorescence amplitude is recorded and matched to the sinusoidal form of the illumination in order to retrieve the relative positions of the fluorescent sources with respect to the illumination profile.

This process provides improved localization information along the direction of the sinusoidal pattern and can be repeated using various ori-

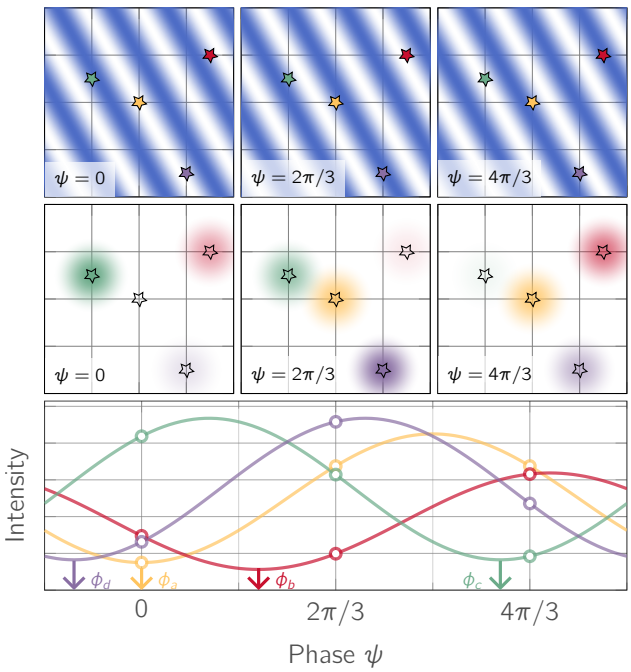

Figure III.3 – *A standing-wave excitation (blue stripes) is precisely shifted over the sample (top row), driving the variation in fluorescence intensity (centre row). The signal of individual sources is then matched to the intensity pattern, allowing the retrieval of the emitter's position ϕ.*

entations for an isotropic gain. Two perpendicular pattern orientations are sufficient to achieve an $x - y$ homogeneous localization precision.

The theoretical limits of the maximal precision achievable, experimentally verified in the publication introducing SIMPLE [16] attached as appendix A, will be derived (section III.3) before the results are validated through numerical simulations (section III.5). Independent research teams have reached similar results, enabling the increase of lateral and/or axial resolution using a standing-wave illumination [78–81].

Notation conventions

In order to simplify the notation and to make a clear distinction between the phase of the pattern ψ (that can be tuned) and the *position relative to the phase* of the emitter, one notes:

$$\psi(\mathbf{x}_p) = \phi_p, \qquad \eta(\mathbf{x}_p) = \eta_p \tag{III.1}$$

Furthermore, to refer to different parameters, we introduce a series of subscript to prevent confusion. The subscripts are displayed only in case of possible ambiguity, each having a different meaning:

- p identifies emitters, $p = 1, \ldots, P$
- κ corresponds to the pattern's phases $\{\psi_\kappa \in \Psi \mid \kappa = 1, \ldots, K\}$
- τ denotes the pattern's orientations $\{\theta_\tau \in \theta \mid \tau = 1, \ldots, T\}$
- ν indexes the frame, $\nu = 1, \ldots, V$ (usually $V = K \cdot T$)

III.1 Point emitters in patterned illumination

Much like MINFLUX, SIMPLE uses the convenience of dealing with isolated emitters. As seen in equation (II.16), the expression of the emission η and its corresponding signal ς can be drastically simplified using punctual emitters (equation (II.15)). The Dirac deltas in the expression of the

density reduce the convolution to a standard product, much easier to deal with. Using a standing-wave illumination, the signal becomes:

$$\begin{aligned} \varsigma(\mathbf{x}, \psi_\kappa) &= h_{\text{PSF}}(\mathbf{x}) \otimes \Big[\rho(\mathbf{x})\, \mathcal{R}\Big(\mathcal{I}\big[\psi(\mathbf{x}) - \psi_\kappa\big]\Big)\Big] \\ &\overset{(II.15)}{=} \sum_p h_{\text{PSF}}(\mathbf{x} - \mathbf{x}_p)\, \eta_p(\psi_\kappa) \\ \text{with} \quad \eta_p(\psi_\kappa) &= \frac{A_p}{2}\Big[1 - m\cos(\phi_p - \psi_\kappa)\Big] \end{aligned} \tag{III.2}$$

where ψ_κ is a tunable phase-shift. In the case where only a single emitter is considered, and in order not to overload the notation, one writes $\eta_p(\psi_\kappa) = \eta_\kappa$.

From equation (III.2), one notes that the contribution of each emitter is simply a diffraction-limited spot, whose intensity is defined (and modulated) by its location ϕ on the standing-wave illumination. The overall image is then obtained by summing the contribution of individual fluorescent sources.

III.2 Illumination's properties

In order to set the foundations necessary to derive the theoretical limits of SIMPLE, it is useful to define some key properties of the illumination. These mathematical properties will lead to simplifications of the results and provide some intuitive understanding of otherwise rather abstract formulas.

III.2.1 Patterns/Signal summation

The *harmonic addition theorem* [82] states that the sum of sinusoidal functions of period L and with amplitudes a_κ and phases ψ_κ can be expressed as another sinusoid of period L. This result, widely used in electrical engineering [83] and serving as foundation of phasor arithmetic, can be trivially extended to the sum of illuminations $\mathcal{I}_\kappa$ (or its

corresponding fluorescence η_κ) as follows:

$$\begin{aligned}\langle \mathcal{I} \rangle_\kappa &= \frac{1}{K}\sum_{\kappa=1}^{K}\frac{a_\kappa}{2}\Big[1 - m\cos(\psi_\kappa - \psi(\mathbf{x}))\Big] \\ &= \frac{1}{2K}\left[\sum_{\kappa=1}^{K} a_\kappa - m\sum_{\kappa=1}^{K} a_\kappa \cos\big(\overline{\psi} - \psi(\mathbf{x})\big)\right] \\ &= \frac{A}{2}\Big[1 - \overline{m}\cos\big(\overline{\psi} - \psi(\mathbf{x})\big)\Big]\end{aligned} \tag{III.3}$$

which has an identical form to that in equation (II.9), given the parameters' definitions below*:

$$\begin{cases} \overline{a}^2 = \sum_{i,j} a_i a_j \cos(\psi_i - \psi_j) \\ \tan\overline{\psi} = \dfrac{\sum_\kappa a_\kappa \sin(\psi_\kappa)}{\sum_\kappa a_\kappa \cos(\psi_\kappa)} \\ A = \dfrac{1}{K}\sum_\kappa a_\kappa \\ \overline{m} = m\dfrac{\overline{a}}{A} \end{cases} \tag{III.4}$$

This result also implies that for a linear response of the fluorophore to the excitation, the emission η is *parametrically equivalent* to the illumination $\mathcal{I}$, *i.e.* $\eta \equiv \mathcal{I}$. As this hypothesis is assumed to be true in the scope of this work, η and $\mathcal{I}$ will, depending on the context, be used interchangeably upon correct modification of the multiplicative constant to ensure the physical correctness of the units.

*Interestingly, these expressions are identical to the *mean direction* and *resultant length* of a cardioid distribution, defined in the context of circular statistics [84, 85] which will be fundamental later on for the deducing of the analytical expression of the phase retrieval in SIMPLE.

III.2.2 Homogeneity criterion

From equation (III.3), one notes that the resulting pattern has a spatial dependency through the phase term $\psi(\mathbf{x})$. This leads to the definition of the *homogeneity criterion*, $\overline{m} = 0$, that has to be fulfilled in order to prevent the spatial dependency of the illumination. Besides the trivial case where $m = 0$, homogeneity is achieved when $\overline{m} = 0 \Leftrightarrow \overline{a}^2 = \sum_{i,j} a_i a_j \cos(\psi_i - \psi_j) = 0$.

Such a condition can be artificially constructed by forcing the parameters of one of the illuminations, $\mathcal{I}_i$, to cancel out the collective behaviour of the $K-1$ other illuminations, denoted $\mathcal{I}_{\kappa\neq i}$. Therefore, the amplitude of $\mathcal{I}_i$ should match the one of $\mathcal{I}_{\kappa\neq i}$, with opposite phase:

$$\begin{aligned} a_i &= \overline{a}_{\kappa\neq i} \\ \psi_i &= \overline{\psi}_{\kappa\neq i} \pm \pi \end{aligned} \tag{III.5}$$

These conditions are naturally satisfied for equally spaced phase-shifts spanning over a whole period, *i.e.* $\psi_\kappa = 2\pi(\kappa-1)/K$, if the amplitudes a_κ are all identical, which is usually assumed in SIM, for example.

III.2.3 m-b_o equivalence

Next, we show the equivalence between an offset b_o in the illumination and an alteration of the modulation depth m (see figure II.7). This equivalence is used to avoid including the offset terms and focus instead on the modulation that is physically more relevant; the harmonic addition theorem gives an expression of the modified modulation and amplitude when various contributions to the signal are mixed.

$$\mathcal{I}(A, m, b_o) = \mathcal{I}(A^*, m^* = 1, {b_o}^*) = \mathcal{I}(A^\bullet, m^\bullet, {b_o}^\bullet = 0) \tag{III.6}$$

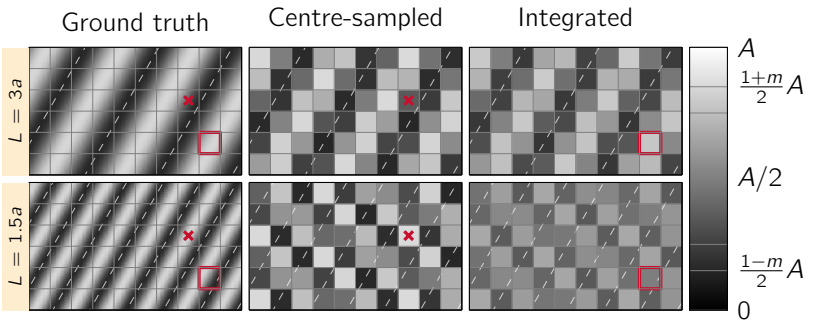

Figure III.4 – *The finite size of pixels impacts the effective modulation. Whether the pattern is sampled punctually at the centre of pixels or integrated over a pixel strongly impacts the output, eventually erasing the original pattern.*

with the equivalence ensured by the following parameter transformation:

$$\begin{cases} A^* = mA, & \text{and} \quad {b_o}^* = b_o + \dfrac{1-m}{2}A \\ A^\bullet = A + 2b_o, & \text{and} \quad m^\bullet = m\dfrac{A}{A+2b_o} \end{cases} \tag{III.7}$$

III.2.4 Pixel integration

The harmonic addition theorem can also be applied using continuous averaging, replacing sums with integrals, which is particularly useful in order to understand the effect of pixelation on the modulation (superscript $\square$). For each pixel indexed by u,v, of centre $\mathbf{x}_{u,v}$ and area $S_{u,v}$ one has:

$$\begin{aligned} \mathcal{I}_{u,v} &= \frac{1}{S^{\text{px}}_{u,v}} \int\limits_{\mathbf{x}\in S^{\text{px}}_{u,v}} \mathcal{I}(\mathbf{x})\,\mathrm{d}^2\mathbf{x} \\ &= \frac{A}{2}\Big[1 + m^{\square}\cos\big(\psi_\theta(\mathbf{x}_{u,v})\big)\Big] \end{aligned} \tag{III.8}$$

for square pixels of dimensions $a \times a$, the modulation is expressed as:

$$m^{\square} = 2m \frac{\sin\left[\pi a \cos\theta\right] \sin\left[\pi a \sin\theta\right]}{\pi^2 a^2 \sin 2\theta} \tag{III.9}$$

Simulated SIM images based on pre-existing images–like training datasets used in machine-learning (ML) algorithms [65, 66]– would have to account for that effect to be accurate. The resulting image can vary greatly, especially if the pixel size and pattern's wavelength are of similar order of magnitude (see figure figure III.4). The effective contrast is lower when the signal is integrated, and the striped pattern can vanish if the sampling is insufficient to accurately represent it.

By taking this effect into consideration, the simulated images would better model random samples: in its current implementation (centre-sampled), the training sets over-estimate the modulation and do not account for the point-like nature of the fluorophores; further propagating on the quality of reconstruction on real data. An alternative would be to randomly place point-like emitters on the images and adjust their intensity based on the local grey-scale pixel value as well as the illumination intensity.

III.2.5 Homogeneous phase-shifts $\xi = 1$

The simplest illumination sequence, borrowed from standard SIM modalities, consists in taking a series of translated–phase shifted–illumination patterns that result in a flat intensity profile once summed up. Typically, one has equidistant shifts dividing a whole period in K phases:

$$\delta\psi_\kappa = 2\pi\left(\frac{\kappa - 1}{K} - \frac{K - 1}{2K}\right), \qquad \kappa = 1, \ldots, K \tag{III.10}$$

where κ indexes the applied phases, which has been centred on 0, to consistently keep $\psi = 0$ referring to the trough of the illumination.

Using equations (III.3), (III.5) and (III.10), one gets the convenient following expressions:

$$\langle \mathcal{I} \rangle_\kappa \equiv \bar{\eta} = \frac{A}{2} \tag{III.11a}$$

$$\mathrm{std}_\kappa(\mathcal{I}) \equiv \sigma_\eta = \frac{mA}{2\sqrt{2 - \frac{2}{K}}} \tag{III.11b}$$

which lead to a formulation of the amplitude-related illumination parameters (A and m) in function of the K recorded intensities η_κ:

$$\begin{cases} A = 2\,\bar{\eta} = \dfrac{2N}{K} \\ m = \dfrac{\sigma_\eta}{\bar{\eta}}\sqrt{2 - \dfrac{2}{K}} \end{cases} \tag{III.12}$$

The localization information of the emitter–the core interest of this thesis–is encoded in the "phase-position" (see figure III.3), and therefore, expressing this phase, ϕ, in terms of η_κ is crucial.

The phase-shift applied to the illumination is often described hence interpreted as a translation (and is indeed equivalent). However, much like the aforementioned phasors (see section III.2.1), due to its periodic nature, the phase is better represented in polar coordinates. Here, as the phase-shifts occur (change in azimuth), the intensity of the signal (radial distance) is modulated (see figure III.5).

The field of directional statistics [85], and more precisely of circular statistics [84], provides very useful results that can be applied here (see also section III.2.1) as the emission dependency on the pattern's phase is parametrically equivalent to a cardioid distribution $\mathcal{C}$:

$$\begin{aligned} &\begin{cases} \eta\,(\psi|m,\phi) \propto 1 - m\cos(\psi - \phi) \\ \mathcal{C}(\psi|\rho,\theta) \propto 1 + 2\rho\cos(\psi - \theta) \end{cases} \\ \Longrightarrow\ &\begin{cases} m = \dfrac{\rho}{2} : \text{mean resultant length} \\ \phi = -\theta : \text{average direction} \end{cases} \end{aligned} \tag{III.13}$$

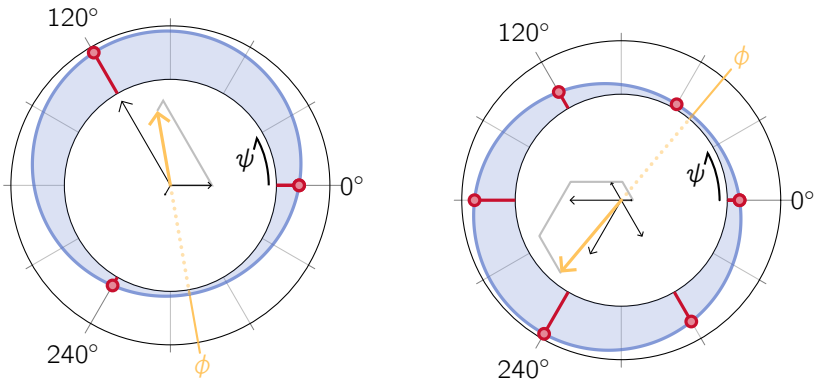

Figure III.5 – *Schematic representation of the construction of equation* (III.14a)*: the sum of the vectors (in black, defined by a the pattern's phase and the corresponding signal intensity) allows the obtention of the emitter's phase (yellow ϕ) and modulation (length of the resultant vector, see equation* (III.14b)*). The results stay valid $\forall K \geq 3$.*

Thanks to this direct correspondence and the results for the *mean resultant length* and *average direction* derived in [84], the main parameters can be expressed in a very simple form as:

$$\phi = \arctan(C, S) \tag{III.14a}$$

$$m = 2\sqrt{\overline{C}^2 + \overline{S}^2} \tag{III.14b}$$

where one used the following standard definitions:

$$\begin{cases} C = \sum_{\kappa=1}^{K} \eta_\kappa \cos\psi_\kappa & S = \sum_{\kappa=1}^{K} \eta_\kappa \sin\psi_\kappa \\ \overline{C} = C / \sum_{\kappa=1}^{K} \eta_\kappa & \overline{S} = S / \sum_{\kappa=1}^{K} \eta_\kappa \end{cases} \tag{III.15}$$

The results of equation (III.15) hold true assuming a homogeneously sampled phase covering a whole 2π-period, but can be generalised to

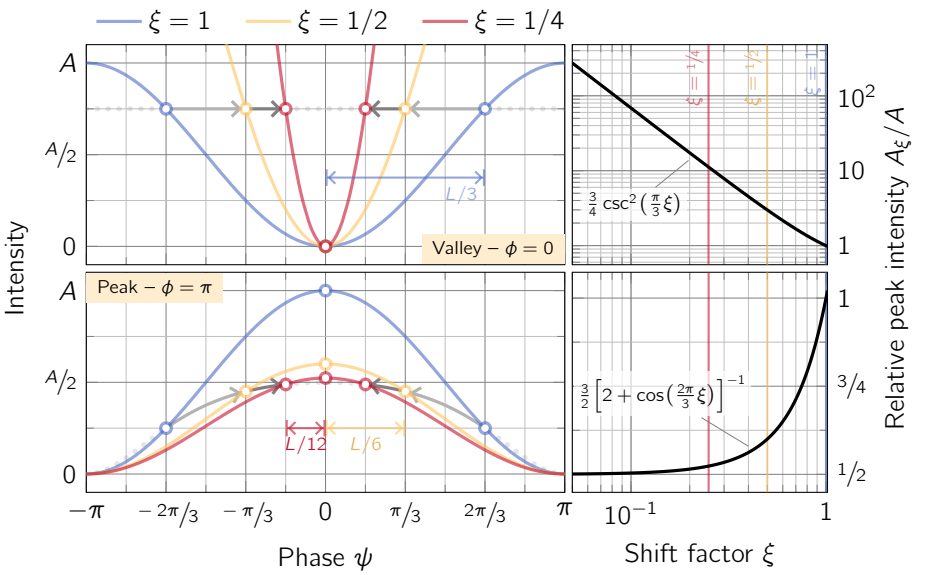

Figure III.6 – *Effect of the shift factor ξ on the illumination amplitude in order to conserve the total signal intensity. When the emitter is placed at the trough of the illumination (upper panels), the amplitude has to be increased as the spacing between the phase shifts is reduced. Inversely, if located on an illumination peak, the intensities will tend to reach identical values for $\xi \ll 1$, effectively cancelling the signal's modulation.*

the case where the phase span is reduced by a factor $\xi \in (0, 1]$, further referred to as *shift factor*.

III.2.6 Reduced-amplitude phase-shifts $\xi < 1$

Similarly to MINFLUX, one can also limit the portion of the FOV where the localization information is confined, and "condense" it to those regions: enhanced precision is achieved at the expense of the covered volume. In summary, in the regions with low average illumination intensities, each detected photons will carry more information about the emitter's location.

In the case of the standing-wave illumination used in SIMPLE, this localized high-precision is achieved by applying phase-shifts of reduced amplitude (see figure III.6):

$$\delta\psi_\kappa = 2\pi\,\xi\left(\frac{\kappa-1}{K}-\frac{K-1}{2K}\right), \qquad \kappa = 1,\dots,K \tag{III.16}$$

The total illumination's amplitude will therefore not be homogeneous and can be written as a generalised version of equation (III.12):

$$A_\xi = \frac{2N}{K_\xi} \tag{III.17}$$

where a few parameters have been introduced to simplify the notation, and will be extensively used in the following sections.

$$\left.\begin{aligned}\mu_\xi &= m\,\frac{\sin(\pi\xi)}{\sin\left(\frac{\pi\xi}{K}\right)}\\ K_\xi &= K-\mu_\xi\cos\phi\\ \beta_\xi &= 1+K_\xi\Sigma^2/N\end{aligned}\right\} \xrightarrow[\xi\to 1]{\lim} \begin{cases}\mu_\xi = 0\\ K_\xi = K\\ \beta_\xi = 1+K\Sigma^2/N\end{cases} \tag{III.18}$$

Note that for $\xi < 1$, the reduced-modulation μ_ξ does not vanish, and K_ξ, respectively A_ξ, have an explicit dependency on ϕ. The relative amplitude change necessary to conserve N, depending on the shift factor ξ, is shown in figure III.6 for two extremal cases: when the emitter is centred at the trough (valley) and at the peak of the illumination.

In addition, one can also generalise equation (III.14a), to the following expression:

$$\phi = \arctan\left[\tan\left(\frac{\pi}{K}\right)C_\xi, \tan\left(\frac{\pi}{K}\xi\right)S_\xi\right] \tag{III.19}$$

using the modified coefficients from equation (III.15) C_ξ and S_ξ :

$$\begin{cases} C_\xi = \displaystyle\sum_{\kappa=1}^{K}\eta_\kappa\cos\left(\psi_\kappa\,\xi^{-1}\right)\\ S_\xi = \displaystyle\sum_{\kappa=1}^{K}\eta_\kappa\sin\left(\psi_\kappa\,\xi^{-1}\right)\end{cases} \tag{III.20}$$

One can intuitively understand the generalised formula (equation (III.19)) by viewing the multiplication by ξ^{-1} as the stretching of the phases, to compensate for the initial squeezing induced by ξ. Then, to account for this stretch, the amplitude is corrected by the ratio of the factors $\tan\left(\frac{\pi}{K}\right)$ and $\tan\left(\frac{\pi}{K}\xi\right)$, leading to the final expression.

In the case of three intensity measurements ($K = 3$), respectively denoted η_L (left), η_C (centre), and η_R (right), the emitter's phase position, signal amplitude and modulation can be obtained through the following expressions (with $\bar{\xi} = \frac{2\pi}{3}\xi$):

$$\begin{cases} \phi = \arctan\left[\tan\left(\bar{\xi}/2\right)\dfrac{\eta_L - \eta_R}{\eta_L - 2\eta_C + \eta_R}\right] & \text{(III.21a)} \\ A = 2\eta_C + \dfrac{1}{2}(\eta_L - 2\eta_C + \eta_R)\csc^2\bar{\xi} & \text{(III.21b)} \\ m = \sec\left(\bar{\xi}/2\right)\dfrac{\sqrt{3{\sigma_\eta}^2 + (\eta_C - \eta_L)(\eta_C - \eta_R)\left[1 + 2\cos\bar{\xi}\right]}}{\eta_L - \eta_C\cos\bar{\xi} + \eta_R} & \text{(III.21c)} \end{cases}$$

III.3 Localisation precision limits

In this section, the localization precision limits of SIMPLE will be derived using the principle of uncertainty propagation (UP) (as presented in [16]) and by deriving the Cramér-Rao lower bound (CRLB). These mathematical developments provide essential information regarding the maximum achievable precision of the class of techniques using patterned illumination for single-molecule localization. We call this class of techniques *modulation-enhanced localization microscopy (meLM)* [17], but other acronyms have later surfaced such as meSMLM [86] or MILM [87], that also convey the key idea of the improved localization power of SMLM achieved by modulating the signal spatio-temporally.

We will provide these limits in their most general form and explore in more details some specific cases of interest.

III.3.1 Uncertainty propagation (UP)

Commonly used in physics and engineering, the uncertainty propagation (UP) formula –also called *error propagation law*– allows for the deduction of the variability of a quantity derived from parameters, themselves subject to random fluctuations (whether inherent to the physical nature of the quantity or to the measuring process itself) [88–91].

Indeed, the uncertainty of a function f, depending on the parameters $x_i \pm \Delta_{x_i}$ is expressed as the collective effect of the perturbations $\Delta_{\mathbf{x}}$ on f, where the sensitivity to said perturbations is given by the function's gradient $\boldsymbol{\nabla} f(\mathbf{x})$:

$$\Delta_f^{\mathrm{UP}}(\mathbf{x}) = \left\| \boldsymbol{\nabla} f(\mathbf{x}) \Delta_{\mathbf{x}} \right\|_2 = \sqrt{\sum_i \left| \frac{\partial}{\partial x_i} f(\mathbf{x}) \cdot \Delta_{x_i} \right|^2} \tag{III.22}$$

where the covariance term is omitted as it vanishes under the assumption of independence of the x_i. Deduced from a Tailor expansion, this formula relies on the regularity of f (continuity, smoothness) that is well satisfied in our case.

Specifically to the context of localization precision estimation, the measured quantities are numbers of photons, which are subject to Poisson and read-out noise. By introducing Σ, the background noise over a given region of interest (ROI), the variance associated to the quantity η can be expressed as ${\Delta_\eta}^2 = \eta + \Sigma^2$ (see [74, equation 19], and the equation (III.41) thereafter).

The application of this formula to the equations (III.11a), (III.14a) and (III.14b)

$$\begin{cases} \dfrac{\partial \phi}{\partial \eta_i} = \dfrac{C\,\partial_{\eta_i} S - S\,\partial_{\eta_i} C}{C^2 + S^2} \\ \qquad \overset{\xi=1}{=} \dfrac{2\cos(\psi_i - \phi)}{mN} \end{cases} \tag{III.23a}$$

$$\begin{cases} \dfrac{\partial m}{\partial \eta_i} = \dfrac{1}{N}\left[\dfrac{C\,\partial_{\eta_i} C + S\,\partial_{\eta_i} S}{\sqrt{C^2 + S^2}} - m\right] \\ \qquad \overset{\xi=1}{=} \dfrac{2\cos(\psi_i - \phi) - m}{N} \end{cases} \tag{III.23b}$$

$$\frac{\partial N}{\partial \eta_i} = 1 \tag{III.23c}$$

where the partial derivatives of C and S with respect to η_i are given by:

$$\partial_{\eta_i} C = \cos\psi_i \qquad \partial_{\eta_i} S = \sin\psi_i \tag{III.24}$$

Homogeneous phase-shifts – $\xi = 1$

The uncertainty, in the case of homogeneous phase-shifts (*i.e.* $\xi = 1$), is finally given by the following form using the parameters defined in equation (III.18) for compactness:

$$\Delta_\phi^{\text{UP}} = \frac{1}{m\sqrt{N}} \begin{cases} \sqrt{2\beta_\xi + m\cos(3\phi)} & \text{if} \quad K = 3 \\ \sqrt{2\beta_\xi} & \text{if} \quad K \geq 4 \end{cases} \tag{III.25a}$$

$$\Delta_m^{\text{UP}} = \frac{1}{\sqrt{N}} \begin{cases} \sqrt{(2+m^2)\,\beta_\xi - 2m^2 + m\cos(3\phi)} & \text{if} \quad K = 3 \\ \sqrt{(2+m^2)\,\beta_\xi - 2m^2} & \text{if} \quad K \geq 4 \end{cases} \tag{III.25b}$$

$$\Delta_N^{\text{UP}} = \sqrt{N\,\beta_\xi} \tag{III.25c}$$

Where for $K = 3$, equations (III.25a) and (III.25b) depend on the emitter's position: the uncertainty will oscillate between two extreme values reached at $\phi = 0$ and $\phi = \pi/3$. The average localization precision can be calculated by integrating equation (III.25a) over ϕ, and its result can

be expressed in function of the complete elliptic integral of the second kind $\mathcal{E}(\alpha) = \int_0^{\pi/2} \sqrt{1 - \alpha \sin^2\theta}\, \mathrm{d}\theta$[†]:

$$\begin{aligned} \left\langle \Delta_\phi^{\mathrm{UP}} \right\rangle_\phi &= \frac{2}{\pi} \frac{\sqrt{2\beta_\xi - m}}{m\sqrt{N}}\, \mathcal{E}\left(\frac{2m}{m - 2\beta_\xi}\right) \\ &= \frac{\sqrt{2\beta_\xi}}{m\sqrt{N}} \left[1 - \frac{m^2}{64{\beta_\xi}^2} + \mathcal{O}\left(m^4\right)\right] \\ &\underset{m=1}{\overset{\Sigma=0}{\Longrightarrow}} = \sqrt{\frac{2}{N}} \left(1 - \frac{1}{64}\right) \end{aligned} \tag{III.26}$$

where we used the following identity:

$$\frac{1}{2\pi} \int_{-\pi}^{\pi} \sqrt{c + m\cos(K\phi)}\, \mathrm{d}\phi = \frac{2}{\pi} \sqrt{c - m}\, \mathcal{E}\left(\frac{2m}{m - c}\right) \tag{III.27}$$

Finally, to switch from phase-like position (in rad) to direct space (in nm) along the pattern's orientation ℓ, one has that:

$$\sigma_\odot^{\mathrm{SIMPLE}} = \frac{L}{2\pi} \Delta_\phi^{\mathrm{UP}} \tag{III.28}$$

where $\sigma_\odot^{\mathrm{SIMPLE}}$ describes the localization precision associated with SIMPLE. This is clear from these expressions that optimal results can be achieved by:

- increased signal intensity ($N \uparrow$)
- low background noise ($\Sigma \to 0$)
- high modulation depth ($m \to 1$)
- short pattern period ($L \to L^{\min}$)
- minimum number of frames ($K = 3$)

[†] An identical reasoning can be applied to calculate $\left\langle \Delta_m^{\mathrm{UP}} \right\rangle_\phi$

To compare the capabilities of SIMPLE compared to the ones of standard SMLM, the most telling quantity is the localization precision gain $\mathcal{G}$ –and its homologue in "ideal" conditions $\mathcal{G}^0$, omitting the noise contribution, and taking both the optimal PSF width, and shortest pattern wavelength:

$$\mathcal{G} = \frac{\sigma_{\odot}^{\text{SMLM}}}{\sigma_{\odot}^{\text{SIMPLE}}} \implies \mathcal{G}^0 = \mathcal{G}\Big|_{\substack{\sigma_b=0 \\ \sigma_{\text{PSF}}=\sigma_{\text{PSF}}^{\min} \\ L=L^{\min}}} \tag{III.29}$$

Using the results in equations (II.17) and (III.25a):

$$\mathcal{G}^0 = \frac{\lambda_{\text{em}}}{\lambda_{\text{ex}}} m \cdot \begin{cases} \dfrac{8}{3\sqrt{2 - m\cos(3\phi)}} & \text{if} \quad K = 3 \\ \dfrac{8}{3\sqrt{2}} \simeq 1.9 & \text{if} \quad K \geq 4 \end{cases} \tag{III.30}$$

For $K = 3$, the average gain reads:

$$\begin{aligned} \left\langle \mathcal{G}^0 \right\rangle_{\phi} &= \frac{1}{2\pi} \int_{-\pi}^{\pi} \mathcal{G}^0 \, \mathrm{d}\phi = \frac{\lambda_{\text{em}}}{\lambda_{\text{ex}}} m \cdot \underbrace{\frac{16\,\mathcal{K}\left(\frac{2m}{m-2}\right)}{3\pi\sqrt{2-m}}}_{\xrightarrow[m=1]{} \simeq 2} \\ &= \frac{\lambda_{\text{em}}}{\lambda_{\text{ex}}} m \left(\frac{4\sqrt{2}}{3} + \frac{m^2}{8\sqrt{2}} + \mathcal{O}\left(m^4\right) \right) \end{aligned} \tag{III.31}$$

In absence of Stoke's shift (*i.e.* $\lambda_{\text{em}} = \lambda_{\text{ex}}$), the minimal requirement to reach an *average* gain of ≥ 1 is to have a modulation of $m = 0.52$. The presence of Stoke's shift will soften this requirement, as in the case of fluorescence, the emission wavelength is larger than the excitation. Similarly, to reach a gain of *at least* 1 all over the FOV, a modulation of $m = 0.61$ is necessary.

Reduced phase-shifts – $\xi < 1$

Despite the very straight-forward core procedure leading to the uncertainty of each parameter, it can give rise to rather intricate formulas. For

the case of three reduced phase-shift ($K = 3$ and $\xi \leq 1$), one obtains:

$$\Delta_\phi^{\mathrm{UP}} = \frac{\csc\left(\bar{\xi}/2\right)\csc\bar{\xi}}{2\sqrt{6}m\sqrt{N}}\sqrt{3 - m\left(1+2\cos\bar{\xi}\right)\cos\phi} \cdot \sqrt{\boldsymbol{\Xi}^{\mathsf{T}}\begin{pmatrix} 12\beta_\xi & -3m\,\beta_\xi & -6\beta_\xi & 3m\left(\beta_\xi+1\right) \\ 6\beta_\xi & -3m\left(2\beta_\xi+1\right) & -12\beta_\xi & m\left(4\beta_\xi-1\right) \\ 0 & 3m & 0 & 2m\left(\beta_\xi-1\right)\end{pmatrix}\boldsymbol{\Phi}} \tag{III.32}$$

$$\text{with} \quad \boldsymbol{\Xi} = \begin{pmatrix} 1 \\ \cos\bar{\xi} \\ \cos 2\bar{\xi}\end{pmatrix}, \quad \boldsymbol{\Phi} = \begin{pmatrix} 1 \\ \cos\phi \\ \cos 2\phi \\ \cos 3\phi\end{pmatrix}, \text{and} \quad \bar{\xi} = \frac{2\pi}{3}\xi$$

For non-analytical results, the use of symbolic calculation software and subsequent numerical evaluation is recommended.

Code III.1 – *Mathematica source code allowing the calculation of the localization precision of the SIMPLE method using uncertainty propagation (UP). On line 15, the number of phases* **k$**, *the shift factor* **x$**, *the background noise* **b$**, *and modulation* **m$** *can be given a numerical value or kept as algebraic quantity (using the equal-dot syntax: "=.").*

```
(* === Setting validity domain of parameters === *)
$Assumptions = {A>0, 0<m<=1, 0<x<=1, n>0, b>=0, Element[{k,i,j},Integers], k>2, 1<=i<=k, 1<=j<=k, -Pi<phi<=Pi,
       Sin[Pi*x]!=0, Cos[2*Pi/k]-Cos[2*Pi*x/k]<0, Csc[Pi*x/2]>=1, m*Cos[phi]*Csc[Pi*x/k]*Sin[Pi*x]<k};

(* === Functions definition === *)
illum[A_,m_,phi_][psi_] := A*(1-m*Cos[psi-phi])/2;
psi[k_,x_:1][i_] := 2*Pi*x(i-1-(k-1)/2)/k;
A[n_,m_,phi_][k_,x_:1] := 2*n/(k-m*Cos[phi]*Csc[Pi*x/k]*Sin[Pi*x]);
s[a_,th_,k_,x_:1] := Sum[a[i]*Sin[th[i]/x],{i,1,k}];
c[a_,th_,k_,x_:1] := Sum[a[i]*Cos[th[i]/x],{i,1,k}];
em[k_,x_:1][illum_,psi_][i_] := illum[psi[k,x][i]];
Dem[n_,b_][i_] := Around[n[i],Sqrt[n[i]+b^2]];
Phi[em_,psi_,k_,x_:1] := ArcTan[-Tan[Pi/k]*c[em,psi,k,x], -Tan[Pi*x/k]*s[em,psi,k,x]];

(* === Calc. of the uncertainty in terms of em[i] & psi[i] === *)
k$ = 3; x$ = 1; b$ =. ; m$ =. ;
tmp = AroundReplace[Phi[em,psi,k$,x$], Map[em[#]->Dem[em,b$][#]&,Range[k$]]]["Uncertainty"];
(* === Uncertainty depending on the illumination parameters === *)
DPhi = Refine[FullSimplify[tmp/.{psi->psi[k$,x$], em->em[k$,x$][illum[A[n,m$,phi][k$,x$],m$,phi]]}]]
```

III.4 Cramér-Rao lower bound (CRLB)

The Cramér-Rao lower bound (CRLB) is a statistical tool that provides a limit for the variance of estimators [92–100]: it sets the minimum uncertainty achievable in the estimation of a quantity. This widely used

procedure, notably in recent advances of super-resolution microscopy [77, 80, 81, 99], will be used to assess the localization power of SIMPLE, and it will be compared to the previously-obtained results from uncertainty propagation.

Analogously to section III.3.1, here too, the parameters to be estimated are as follows:

1. the location of the emitter (initially as a phase-position on the illumination),
2. the signal intensity,
3. the pattern modulation

The values of these quantities can be estimated using the measured photons reaching the surface of the detector. Intrinsically, these intensity measurements –photon-counting– will be random; being subject to shot-noise, and to which the thermally-induced fluctuations of the read-out will additively contribute. The M measured intensities (spread across pixels and/or frames, with index μ) are therefore modelled by random variables Z_μ equal to the sum of the independent random variables X_μ and Y_μ, respectively, the signal and the read-out/background noise.

III.4.1 The Fisher information matrix (FIM)

In order to define the Fisher information matrix, one first requires the definition of the joint probability density f_M of the M independent measurements. Under the assumption of independence of all the measurements, one has:

$$f_M(\mathbf{z}|\boldsymbol{\vartheta}) = \prod_{\mu=1}^{M} f_\mu(z_\mu|\vartheta_\mu) \tag{III.33}$$

where f_μ is the marginal distribution of the measurement μ, z_μ its associated random variable, and $\boldsymbol{\vartheta}$ the parameter vector of the underlying

model[‡]. Note that the random variables are independent but not necessarily identically distributed, *i.e.* θ_μ can be different for each μ.

The likelihood $\mathcal{L}$ is defined as the conjugate prior of the joint density:

$$\mathcal{L}(\boldsymbol{\vartheta}|\mathbf{z}) = f_M(\mathbf{z}|\boldsymbol{\vartheta}) \tag{III.34}$$

The components of the FIM, which quantify the information content for each parameter, are then described as:

$$\mathbf{I}_{i,j} = \mathbb{E}\left[-\frac{\partial^2 \log(\mathcal{L})}{\partial\vartheta_i \partial\vartheta_j}\right] \tag{III.35}$$

And finally, in the case of an unbiased estimator, the CRLB is defined as the inverse of the FIM:

$$\text{var}\,(\vartheta) \geq \frac{1}{\mathbf{I}_\vartheta} \overset{\text{def.}}{=} \Delta_\vartheta^{\text{CRLB}} \tag{III.36}$$

Given the form of the joint distribution in equation (III.33), the log-likelihood can be expressed as a sum over the M measurements. It can be further rearranged thanks to the commutativity between the sum and derivative operators and the linearity of expectation:

$$\mathbf{I}_{i,j} = \sum_{\mu=1}^{M} \mathbb{E}\left[-\frac{\partial^2 \log(f_\mu)}{\partial\vartheta_i \partial\vartheta_j}\right] \tag{III.37}$$

Another property that will be useful later on relates to the change of parameter/representation. If $\boldsymbol{\vartheta}$ is expressed as a function of $\boldsymbol{\alpha}$ –a secondary parametrization *i.e.* $\boldsymbol{\vartheta} = \boldsymbol{\vartheta}(\boldsymbol{\alpha})$, the FIM can be modified by incorporating the Jacobian of the parameter transformation (from Lehmann and Casella [95, equation 6.16, p.125]):

$$\mathbf{I}_{\boldsymbol{\alpha}} = \mathbf{J}^\intercal \mathbf{I}_{\boldsymbol{\vartheta}} \mathbf{J} \quad \text{with} \quad \mathbf{J} = \boldsymbol{\nabla}_{\boldsymbol{\alpha}} \boldsymbol{\vartheta} \tag{III.38}$$

[‡]The sum of the random variables, corresponding to the total number of photons acquired, is not fixed absolutely. Fixing it would require the use of binomial distribution as the individual measurements would therefore not be independent (see Balzarotti et al. [77]).

and for a scalar transformation:

$$\mathbf{I}_{\alpha} = \mathbf{I}_{\vartheta}\left[\frac{\partial\vartheta}{\partial\alpha}\right]^2 \tag{III.39}$$

III.4.2 Read-out noise as a Poisson variable

We use a modified distribution for the background noise in order to match the Poisson nature of the signal's shot-noise. Doing so simplifies the calculation, as the sum of two Poisson variables also Poissonian: $Z = X + Y$ with $X \sim \mathcal{P}_{\nu_1}$ and $Y \sim \mathcal{P}_{\nu_2} \implies Z \sim \mathcal{P}_{\nu_1+\nu_2} = \mathcal{P}_{\nu}$:

$$\mathcal{P}_{\nu_1} + \mathcal{P}_{\nu_2} = \mathcal{P}_{\nu} \tag{III.40}$$

The read-out noise, initially assumed to be Gaussian, $Y_{\mathcal{N}}$, of mean b_o and standard deviation Σ, is therefore approximated by its Poisson "equivalent": $Y_{\mathcal{P}} \sim \mathcal{P}(\Sigma^2) - \Sigma^2 + b_o$. It is equivalent in that the first two moments of the distributions are such as:

$$\begin{aligned} \mathbb{E}(Y_{\mathcal{P}}) &= \mathbb{E}(Y_{\mathcal{N}}) = b_o \\ \mathrm{var}\,(Y_{\mathcal{P}}) &= \mathrm{var}\,(Y_{\mathcal{N}}) = \Sigma^2 \end{aligned} \tag{III.41}$$

and, $Y_{\mathcal{P}}$ converges in probability towards $Y_{\mathcal{N}}$ for $\Sigma^2 \gg 0$. Without loss of generality, the background offset is set to zero; $b_o = 0$.

Hence the probability density function (PDF), describing the probability for a given measurement μ of obtaining N photon from the noisy signal:

$$f(X + Y = N) = \frac{\left(\eta + \Sigma^2\right)^N}{N!} e^{-\left(\eta+\Sigma^2\right)} \tag{III.42}$$

where the subscript μ indexing the measurement number is omitted. From this PDF, we obtain the log-likelihood:

$$\log(\mathcal{L}) = N\log\left(\eta + \Sigma^2\right) - \eta - \Sigma^2 - \log(N!) \tag{III.43}$$

Assuming that η has a functional dependency on a parameter of interest ϑ and that Σ is itself independent of it, the derivation of the log-likelihood with respect to ϑ gives [§]:

$$\frac{\partial \log(\mathcal{L})}{\partial \vartheta} = \left[\frac{x}{\eta + \Sigma^2} - 1\right]\frac{\partial \eta}{\partial \vartheta} \tag{III.44a}$$

$$\frac{\partial \log(\mathcal{L})}{\partial \vartheta} = 0 \quad \Longrightarrow \quad x = \eta + \Sigma^2 \tag{III.44b}$$

Equation (III.44b) has to be satisfied for the estimated parameters to maximise the likelihood –and consequentially the log-likelihood. By further differentiating, one obtains what is often referred to as "Fisher score":

$$-\frac{\partial^2 \log(\mathcal{L})}{\partial \vartheta^2} = \frac{x}{(\eta + \Sigma^2)^2}\left[\frac{\partial \eta}{\partial \vartheta}\right]^2 + \left(1 - \frac{x}{\eta + \Sigma^2}\right)\left[\frac{\partial^2 \eta}{\partial \vartheta^2}\right] \tag{III.45a}$$

$$\mathbf{I}_\vartheta^{\mathcal{P}} \overset{\text{def.}}{=} \mathbb{E}\left(-\frac{\partial^2 \log(\mathcal{L})}{\partial \vartheta^2}\right) = \frac{1}{\eta + \Sigma^2}\left[\frac{\partial \eta}{\partial \vartheta}\right]^2 \tag{III.45b}$$

III.4.3 Shot-noise as a Gaussian variable

Alternatively, for X and Y to have compatible forms, but instead of describing the noise as a Poisson variable –see section III.4.2– one can approximate the signal by a Gaussian variable. In this case, the read-out noise will be more accurately depicted, trading off with the quality of the description of the signal ($\mathcal{P} \xrightarrow{P} \mathcal{N}$ only for large number of photons).

The procedure involves the same steps as in equation (III.41) leading to $X_\mathcal{N} \sim \mathcal{N}\left(\eta, \sqrt{\eta}\right)$. Then, by summing the read-out noise, one has $Z = X + Y \sim \mathcal{N}\left(\eta, \sqrt{\eta + \Sigma^2}\right)$, where we used the summation property of Gaussian random variables.

[§] Accounting for the functional dependency is not strictly necessary at this point. The change of variable (equation (III.38)) can be performed at the very end by multiplication by the Jacobian. It is included here as an example validating the result of equation (III.39)

By repeating the steps detailed from equation (III.42) to equation (III.45), one finally obtains the Fisher matrix

$$\mathbf{I}_{\vartheta}^{\mathcal{N}} = \left[\frac{1}{\eta + \Sigma^2} + \frac{1}{2(\eta + \Sigma^2)^2}\right]\left[\frac{\partial \eta}{\partial \vartheta}\right]^2 \tag{III.46}$$

III.4.4 A Poisson-Normal mixed model

Recognizing that the first term of equation (III.46) corresponds to the previously obtained result from equation (III.45b), $\gamma \in [0, 1]$ can be introduced as a parameter that allows the "mixing" of those two models:

$$\begin{aligned}\mathbf{I}_{\vartheta}^{\text{Mix.}}(\gamma) &= \left[\frac{1}{\eta + \Sigma^2} + \frac{\gamma}{2(\eta + \Sigma^2)^2}\right]\left[\frac{\partial \eta}{\partial \vartheta}\right]^2 \\ &= \mathbf{I}_{\vartheta}^{\mathcal{P}} \underbrace{\left[1 + \frac{\gamma}{2(\eta + \Sigma^2)}\right]}_{\overset{\text{def.}}{=} \Gamma}\end{aligned} \tag{III.47}$$

For values of γ close to zero, the mixed-model will tend to be purely Poissonian, and for $\gamma \to 1$ it converges towards $\mathbf{I}^{\mathcal{N}}$; the model that describes best the reality most likely lying in-between. Moreover, for high values of signal and read-out noise, the mixed-model converges towards $\mathbf{I}^{\mathcal{P}}$, *i.e.* $\lim_{\eta\to\infty} \Gamma = 1$ and $\lim_{\Sigma\to\infty} \Gamma = 1$, justifying the use of $\mathbf{I}_{\vartheta}^{\mathcal{P}}$ for simpler expressions.

Note that the CRLB is not defined if $\mathbf{I} = \infty$. From equations (III.45b), (III.46) and (III.47) the FIM components will diverge if both the signal η and the noise Σ vanish. Such limit cases can be ignored as they have no practical relevance.

III.4.5 CRLB applied to SIMPLE

It is intuitive to understand that each photon, of each measurement, will contribute to the amount of available information in the system. As mentioned before (see equation (III.37)), if these measurements are

completely independent, the overall FIM is obtained simply by summing the Fisher matrices of individual detections; it is the case here, where every pixel (u, v) and frame $(\nu \leftrightarrow (\kappa, \tau))$, are considered independent, forming a collection of M individual measurements $(\mu \leftrightarrow (u, v, \kappa, \tau))$. To simplify the analysis, we will first consider only the total intensity per frame as the illumination is shifted (subscript κ), for a single orientation θ. The result will then be generalised to a series of pattern orientations and including the pixelation.

Using the expression of the emission η from equations (II.1) and (II.9), the Fisher matrix components associated with the parameters of interest, namely ϕ, m, and N, can be re-written, by expressing $\frac{\partial^2 \eta}{\partial \vartheta^2}$:

$$\left[\begin{aligned}
\mathbf{I}_\phi &= \sum_{\kappa=1}^{K} \frac{\Gamma}{2} \frac{\Big(\big[1 - m\cos(\psi_\kappa - \phi)\big]\partial_\phi A + A\, m \sin(\psi_\kappa - \phi)\Big)^2}{A\big[1 - m\cos(\psi_\kappa - \phi)\big] + 2\Sigma^2} && \text{(III.48a)}\\
\mathbf{I}_m &= \sum_{\kappa=1}^{K} \frac{\Gamma}{2} \frac{\Big(\big[1 - m\cos(\psi_\kappa - \phi)\big]\partial_m A + A\cos(\psi_\kappa - \phi)\Big)^2}{A\big[1 - m\cos(\psi_\kappa - \phi)\big] + 2\Sigma^2} && \text{(III.48b)}\\
\mathbf{I}_N &= \sum_{\kappa=1}^{K} \frac{\Gamma}{2} \frac{\Big(\big[1 - m\cos(\psi_\kappa - \phi)\big]\partial_N A\Big)^2}{A\big[1 - m\cos(\psi_\kappa - \phi)\big] + 2\Sigma^2} && \text{(III.48c)}
\end{aligned}\right.$$

where $A = A(\phi, m, N, \Psi)$ is an amplitude function that ensures an average total signal of N photons, for a given set of phases $\psi \in \Psi$.

Equidistant phase-shifts with $\xi < 1$

In particular, for phase shifts that are equally spaced as describes in sections III.2.5 and III.2.6, we have that $A = A_\xi$ (equation (III.17)). Moreover, recalling the parameter simplification listed in equation (III.18), we obtain:

$$\begin{cases} \mathbf{I}_\phi = N_\tau \alpha_\phi & \Longrightarrow \quad \Delta_\phi^{\text{CRLB}} = 1/\sqrt{\alpha_\phi N_\tau} & \text{(III.49a)} \\ \mathbf{I}_m = N_\tau \alpha_m & \Longrightarrow \quad \Delta_m^{\text{CRLB}} = 1/\sqrt{\alpha_m N_\tau} & \text{(III.49b)} \\ \mathbf{I}_N = \alpha_N / N_\tau & \Longrightarrow \quad \Delta_N^{\text{CRLB}} = \sqrt{N_\tau / \alpha_N} & \text{(III.49c)} \end{cases}$$

The α coefficients are introduced to highlight the dependency on N_τ of the different quantities.

$$\begin{cases} \alpha_\phi = \dfrac{m^2}{{K_\xi}^3} \displaystyle\sum_{\kappa=1}^{K} \dfrac{\left[K \sin(\psi_\kappa - \phi) - \frac{\mu_\xi}{m} \sin\phi + \mu_\xi \sin\psi\right]^2}{\beta_\xi - m\cos(\psi_\kappa - \phi)} & \text{(III.50a)} \\ \alpha_m = \dfrac{1}{{K_\xi}^3} \displaystyle\sum_{\kappa=1}^{K} \dfrac{\left[K \cos(\psi_\kappa - \phi) - \frac{\mu_\xi}{m} \cos\phi\right]^2}{\beta_\xi - m\cos(\psi_\kappa - \phi)} & \text{(III.50b)} \\ \alpha_N = \dfrac{1}{K_\xi} \displaystyle\sum_{\kappa=1}^{K} \dfrac{\left[1 - m\cos(\psi_\kappa - \phi)\right]^2}{\beta_\xi - m\cos(\psi_\kappa - \phi)} & \text{(III.50c)} \end{cases}$$

These coefficients can be numerically evaluated but conveniently simplify in some cases that will be discussed thereafter.

Homogeneous phase-shifts: $\xi = 1$

For the standard SIMPLE scenario, where $\xi = 1$, the pattern is shifted K times, covering the whole 2π-period, and leading to a homogeneous average illumination (see section III.2.2). In this case, the α coefficients are:

$$\begin{cases} \alpha_\phi = \dfrac{m^2}{K}\displaystyle\sum_{\kappa=1}^{K} \dfrac{\sin^2(\psi_\kappa - \phi)}{\beta_\xi - m\cos(\psi_\kappa - \phi)} & \text{(III.51a)} \\ \alpha_m = \dfrac{1}{K}\displaystyle\sum_{\kappa=1}^{K} \dfrac{\cos^2(\psi_\kappa - \phi)}{\beta_\xi - m\cos(\psi_\kappa - \phi)} & \text{(III.51b)} \\ \alpha_N = \dfrac{1}{K}\displaystyle\sum_{\kappa=1}^{K} \dfrac{\left[1 - m\cos(\psi_\kappa - \phi)\right]^2}{\beta_\xi - m\cos(\psi_\kappa - \phi)} & \text{(III.51c)} \end{cases}$$

where the dependency on the phase ϕ can be averaged over the FOV by similar integration to the one performed in equation (III.26):

$$\begin{cases} \langle \alpha_\phi \rangle_\phi = \beta_\xi - \sqrt{\beta_\xi^2 - m^2} & \text{(III.52a)} \\ \langle \alpha_m \rangle_\phi = \dfrac{\beta_\xi}{m^2}\left[\dfrac{\beta_\xi}{\sqrt{\beta_\xi^2 - m^2}} - 1\right] & \text{(III.52b)} \\ \langle \alpha_N \rangle_\phi = 2 - \beta_\xi + \dfrac{(\beta_\xi - 1)^2}{\sqrt{\beta_\xi^2 - m^2}} & \text{(III.52c)} \end{cases}$$

Finally, in order to change representation from "phase" to "position", the FIM is multiplied by the Jacobian of the transformation (using equations (II.10b) and (III.38)). Hence, along the direction of $\boldsymbol{\ell}$:

$$\frac{\partial \phi}{\partial \ell} = \frac{2\pi}{L} \implies \mathbf{I}_\ell = \mathbf{I}_\phi \frac{4\pi^2}{L^2} \tag{III.53}$$

and for the x and y components, $\boldsymbol{\ell}$ is projected onto each axis:

$$\frac{\partial \phi}{\partial \mathbf{x}} = \frac{2\pi}{L}\begin{pmatrix}\cos\theta \\ \sin\theta\end{pmatrix} \implies \mathbf{I}_\mathbf{x} = \mathbf{I}_\phi\left[\frac{2\pi}{L}\begin{pmatrix}\cos\theta \\ \sin\theta\end{pmatrix}\right]^2 \tag{III.54}$$

Note that the "amount of information" embedded in the phase is conserved, as $\cos^2\theta + \sin^2\theta = 1$, and distributed between the components of $\mathbf{x}$ according to the illumination's orientation θ. As long as the

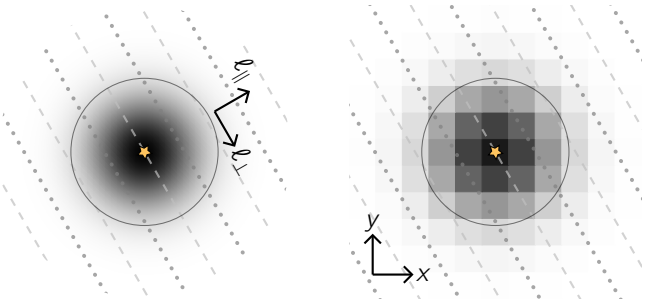

Figure III.7 – *Diffraction-limited spot show with infinitely small pixels (left) and with finite size (right). The illumination pattern (peak and trough represented as dashed and dotted lines) orient the coordinate system* $(\ell_{\parallel}, \ell_{\perp})$ *in absence of pixels. The pixel grid breaks the symmetry and the natural axis become* (x, y)*. The circle has a* $2\sigma_{\text{PSF}}$ *radius around the emitter's centre.*

finite pixel size is not taken into account, the symmetry of the system suggests that $(\ell_{\parallel}, \ell_{\perp})$ are the most natural coordinates to use (see figure III.7).

Spatial spreading of the fluorescence

In the previous derivations, the spatial dispersion of the emission had been left aside. However, the signal is spread spatially over a region defined by the PSF (see figure III.8), and will now be accounted for. To do so ($\eta \rightarrow \varsigma$), only minor changes have to be made to the previous results: according to equation (III.2), including the effect of diffraction limit is achieved solely by a multiplication of each emitters' fluorescence by the system's PSF. This multiplicative refinement suggests –through the "product to sum" effect of the logarithm in the score function– that the information from the PSF will behave additively. This new contribution to the system will be called $\mathbf{I}_{\text{PSF}}$.

For ease of calculation, the PSF is assumed to have a Gaussian shape, a good approximation of the Airy disk [101–105]. One can write, for an emitter p:

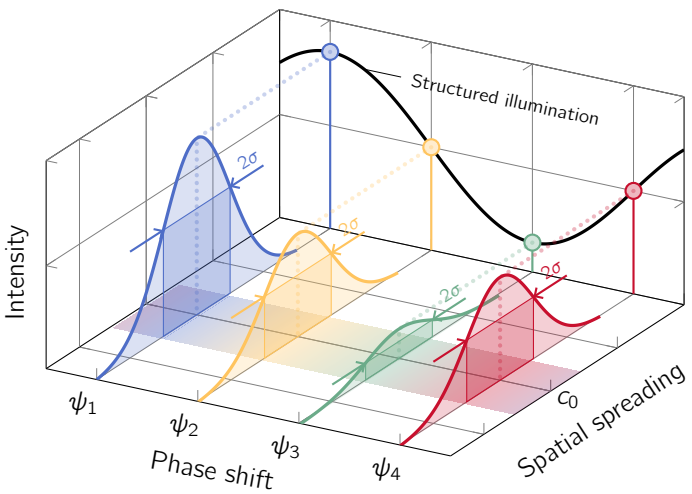

Figure III.8 – *The modulated intensity, driven by the illumination and its applied shifts, alters only the amplitude of the signal: the diffraction limit will consistently spread the signal in space. Both the signal's modulation and spreading contain information about the emitter's location.*

$$\varsigma_p(\mathbf{x}) = \frac{1}{2\pi\sigma_{\text{PSF}}^2}\exp\left(-\frac{(\mathbf{x}-\mathbf{x}_p)^2}{2\sigma_{\text{PSF}}^2}\right)\eta_p(\mathbf{x}) \tag{III.55}$$

In absence of noise ($\Sigma = 0$), the PSF contributes with a term N/σ_{PSF}^2 to the localisation information–corresponding to the expression of the standard error of the mean. Therefore, for each pattern orientation (with subscript τ) the information available both from the spatial spreading and the phase-localisation is given by:

$$\begin{cases} \mathbf{I}_{\ell_{\parallel}^{\tau}} = \dfrac{1}{2}\mathbf{I}_{\text{PSF}} + \mathbf{I}_{\ell_\phi} = \dfrac{N_\tau}{\sigma_{\text{PSF}}^2} + \dfrac{4\pi^2 N_\tau}{L^2}\alpha_\phi \\ \mathbf{I}_{\ell_{\perp}^{\tau}} = \dfrac{1}{2}\mathbf{I}_{\text{PSF}} = \dfrac{N_\tau}{\sigma_{\text{PSF}}^2} \end{cases} \tag{III.56}$$

Consequently, as each pattern orientation is independent, the CRLB resulting of T orientations $\theta \in \Theta$ reads:

$$\begin{cases} \mathbf{I}_x = \displaystyle\sum_{\tau=1}^{T}\left[\mathbf{I}_{\ell_{\parallel}^{\tau}}\cos^2(\theta_\tau) + \mathbf{I}_{\ell_{\perp}^{\tau}}\sin^2(\theta_\tau)\right] \\ \mathbf{I}_y = \displaystyle\sum_{\tau=1}^{T}\left[\mathbf{I}_{\ell_{\parallel}^{\tau}}\sin^2(\theta_\tau) + \mathbf{I}_{\ell_{\perp}^{\tau}}\cos^2(\theta_\tau)\right] \end{cases} \tag{III.57}$$

In the simplest case, where the illumination is rotated T times with equally distributed pattern orientations (*e.g.* $\theta_\tau \in \{\theta, \theta + \pi/2\}$), where $N_\tau = N/T$, the result is symmetrical in x and y and given by:

$$\mathbf{I}_x = \mathbf{I}_y = N\left[\frac{1}{\sigma_{\text{PSF}}^2} + \frac{2\pi^2}{L^2}\alpha_\phi\right] \tag{III.58}$$

By extrapolation, the presented model can be extended to account for finite pixel-size and non-zero background noise. Indeed, the term associated with the PSF, $\mathbf{I}_{\text{PSF}}$, corresponds to the starting point in Thompson's derivations. Logically, this term can be modified using the results developed in the scope of SMLM [75] to gain in generality and accuracy:

$$\mathbf{I}_{\text{PSF}} = \frac{N_\tau}{\sigma_a^2}\left[\frac{16}{9} + \frac{8\pi\sigma_a^2\,{\sigma_b}^2}{N_\tau a^2}\right]^{-1} \qquad \text{where} \quad \sigma_a^2 = \sigma_{\text{PSF}}^2 + \frac{a^2}{12} \tag{III.59}$$

Finally, the pixelation and read-out noise have to be included in the FIM component associated with the patterned illumination. From the previous expressions of $\alpha_{\bullet}$, one sees that, the standing-wave brings extra information through the *intensity* modulation of the signal and not from the signal's spreading. Therefore, the extra variability induced by the pixelation and read-out can simply be embedded in the noise term Σ, and replaced in $\mathbf{I}_\phi$.

The cumulative noise from a circular ROI of radius R is:

$$\Sigma_\circ^2(R) = {\sigma_b}^2\frac{\pi R^2}{a^2} \quad \rightsquigarrow \quad \Sigma_\circ^2(2\sigma_{\text{PSF}}) = {\sigma_b}^2\frac{4\pi\sigma_{\text{PSF}}^2}{a^2} \tag{III.60}$$

This expression corresponds to the pixelation term for the uncertainty of the total number of photon in Thompson et al. [74, equation 19]. A $2\sigma_{\text{PSF}}$ radius around the location of an emitter, which contains most of the signal, is shown in figure III.7.

The localization precision coming from –and along– the pattern can be expressed in rather simple forms by setting some parameters to their limit values (absence of noise, ideal modulation, homogeneous phase-shifts) and limiting the number of phase shifts to $K = 3$.

One has, for three homogeneous phase-shifts:

$$\Delta_\ell^{\text{CRLB}}\Big|_{\substack{K=3\\ \xi=1}} = \frac{L}{2\pi m\sqrt{N_\tau}}\sqrt{\frac{m^3\cos(3\phi) + 3m^2\beta_\xi - 4\beta_\xi^3}{m^2 + m\beta_\xi\cos(3\phi) - 2\beta_\xi^2}} \tag{III.61}$$

And for three reduced phase-shifts ($\xi \leq 1$) without read-out noise ($\Sigma = 0$) and with an ideal modulation ($m = 1$):

$$\Delta_\ell^{\text{CRLB}}\Big|_{\substack{K=3\\ m=1\\ \Sigma=0}} = L\csc\left(\bar{\xi}/2\right)\frac{3 - \left(1 + 2\cos\bar{\xi}\right)\cos\phi}{4\pi\sqrt{2N_\tau\left(2 + \cos\bar{\xi}\right)}} \tag{III.62}$$

From these equations, one gets that increasing the localization precision can be achieved by :

- increasing the number of photons N
- reducing the pattern's displacement and its period L
- keeping the emitter at the trough of the illumination, *i.e.* $\phi = 0$
- improving the modulation
- reducing the noise

III.4.6 Comparison of localization precision limits

In the previous sections III.3.1 and III.4, the theoretical framework of the fundamental limits achievable using SIMPLE has been derived using uncertainty propagation (UP) and Cramér-Rao lower bound (CRLB). In this section, the principal results are summarized in lookup tables allowing an easy comparison between the two. Both models will later on be verified by comparison to simulated data.

Table III.1 – *Uncertainty of the phase ϕ, obtained by using three evenly spaced phase shifts, calculated from equations* (III.25a) *and* (III.61)*. Note the multiplicative constant* $\left(m\sqrt{N}\right)^{-1}$.

$\Delta_\phi = \frac{1}{m\sqrt{N}} \times$	$\phi \in (-\pi, \pi]$	
	CRLB	UP
–	$\sqrt{\frac{m^3\cos(3\phi) + 3m^2\beta_\xi - 4\beta_\xi^3}{m^2 + m\beta_\xi\cos(3\phi) - 2\beta_\xi^2}}$	$\sqrt{2\beta_\xi + m\cos(3\phi)}$
$m = 1$	$\sqrt{\frac{\cos(3\phi) + 3\beta_\xi - 4\beta_\xi^3}{1 + \beta_\xi\cos(3\phi) - 2\beta_\xi^2}}$	$\sqrt{2\beta_\xi + \cos(3\phi)}$
$\Sigma^2 = 0$	$\sqrt{\frac{m^3\cos(3\phi) + 3m^2 - 4}{m^2 + m\cos(3\phi) - 2}}$	$\sqrt{2 + m\cos(3\phi)}$
$\begin{bmatrix} m = 1 \\ \Sigma^2 = 0 \end{bmatrix}$	1	$\sqrt{2 + \cos(3\phi)}$

Table III.2 – *Average and limit phase ψ uncertainty, obtained by using three evenly spaced phase shifts, calculated from equations (III.25b) and (III.49b). Note the multiplicative constant $\left(\sqrt{N}\right)^{-1}$. The value decorated by an asterisk has different values for CRLB and UP.*

$\Delta_\psi = \frac{1}{m\sqrt{N}}\times$	$\phi = 0$	$\phi = \pi/3$	$\langle\dots\rangle_\phi$	
	CRLB = UP		CRLB	UP
–	$\sqrt{2\beta_\xi + m}$	$\sqrt{2\beta_\xi - m}$	$\beta_\xi - \sqrt{\beta_\xi^2 - m^2}$	$\frac{2}{\pi}\sqrt{2\beta_\xi - m}\,\mathcal{E}\left(\frac{2m}{m-2\beta_\xi}\right)$
$m = 1$	$\sqrt{2\beta_\xi + 1}$	$\sqrt{2\beta_\xi - 1}$	$\beta_\xi - \sqrt{\beta_\xi^2 - 1}$	$\frac{2}{\pi}\sqrt{2\beta_\xi - 1}\,\mathcal{E}\left(\frac{2}{1-2\beta_\xi}\right)$
$\Sigma^2 = 0$	$\sqrt{2+m}$	$\sqrt{2-m}$	$1 - \sqrt{1-m^2}$	$\frac{2}{\pi}\sqrt{2-m}\,\mathcal{E}\left(\frac{2m}{m-2}\right)$
$\begin{bmatrix} m=1 \\ \Sigma^2=0 \end{bmatrix}$	1 | $\sqrt{3}^\star$	1	1	$\frac{2}{\pi}\mathcal{E}(-2) \simeq 1.39$

III.5 Numerical simulations

A more *hands-on* approach compared to the previously discussed mathematical derivations is the numerical simulation of realistic images offering the flexibility of a controlled environment where all the parameters can be tuned individually. The user-set parameters typically include:

- The total number of photons N
- The modulation m and periodicity L of the illumination
- The system's point-spread function (PSF) σ_{PSF}
- The pixel size a and field of view (FOV) dimensions
- The read-out noise (typically Gaussian $\mathcal{N}(b_o, \sigma_b)$)
- The number of phase shifts K
- The amplitude of the phase shift controlled by the shift factor ξ

The main parameter of interest in this work is the phase position ϕ. We are specifically interested in knowing the accuracy and precision

of this parameter when calculated in different imaging conditions. The simulation process is then described as follows:

1. A point emitter is placed randomly on a pixel at the centre of the field of view (FOV) and assigned a random phase position ϕ_{GT}
2. Based on this initial phase and the K shifts in illumination, a series of amplitudes is calculated
3. N individual photons are generated around the emitter's position according to σ_{PSF}
4. The photons are then binned to form a series of pixelized images of size FOV. Each frame having the matching relative amplitude given by the local illumination's intensity
5. The combination of shot-noise (Poisson-randomised signal) and read-out noise (additive Gaussian, binomially rounded) is applied to the original images
6. On each image, the central part of the FOV is masked and its total intensity recorded
7. Using equation (III.19), the estimated phase position ϕ is calculated and compared to ϕ_{GT}
8. This process is repeated (typically $10^5\times$) to obtain statistically significant results

Points 1 to 5 listed above are represented in figure III.9. Note that for fair comparison between standard SMLM and SIMPLE, the read-out noise has to be accounted for only once per frame; constructing the wide-field equivalent image by summing the end-result SIMPLE images would result in multiplying the noise by the number of frames V.

Exemplary binary masks used for signal collection (point 6 above) are shown in figure III.10. The mask's dimension has to be chosen in order to maximize the amount of signal gathered while limiting the contribution of noise.

The signal gathered by the masking is then fed into equations (III.19) and (III.21) which provide estimates of the underlying ground truth (GT)

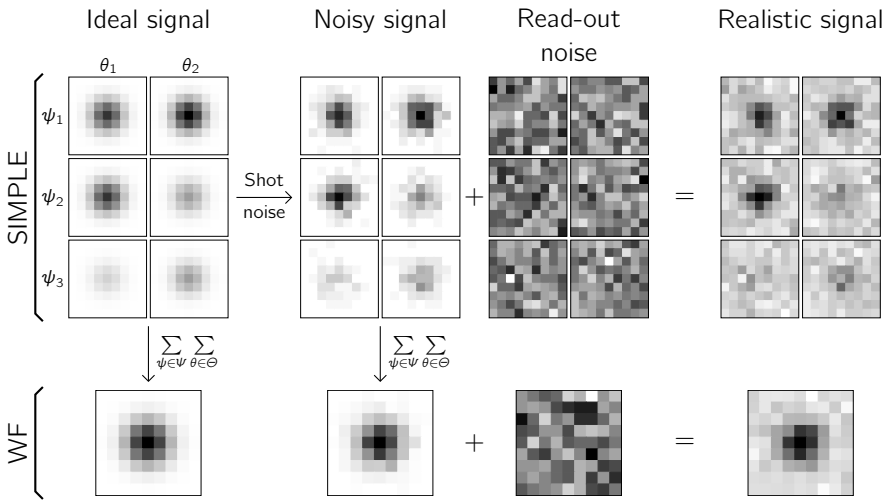

Figure III.9 – *Step-by-step description of the image simulation procedure allowing the fair comparison between SMLM and SIMPLE. Intensity modulated PSF are generated (left) on which shot-noise and read-out noise is applied (centre) in order to for a realistic image with tunable conditions (right).*

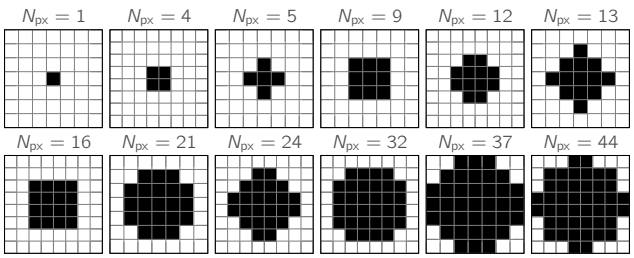

Figure III.10 – *Different mask sizes used for binning the signal. The optimal masking will depend on the imaging parameters such as σ_{PSF},a,N, and σ_b. Generally, high signals and/or low noise will see improved results with bigger masks.*

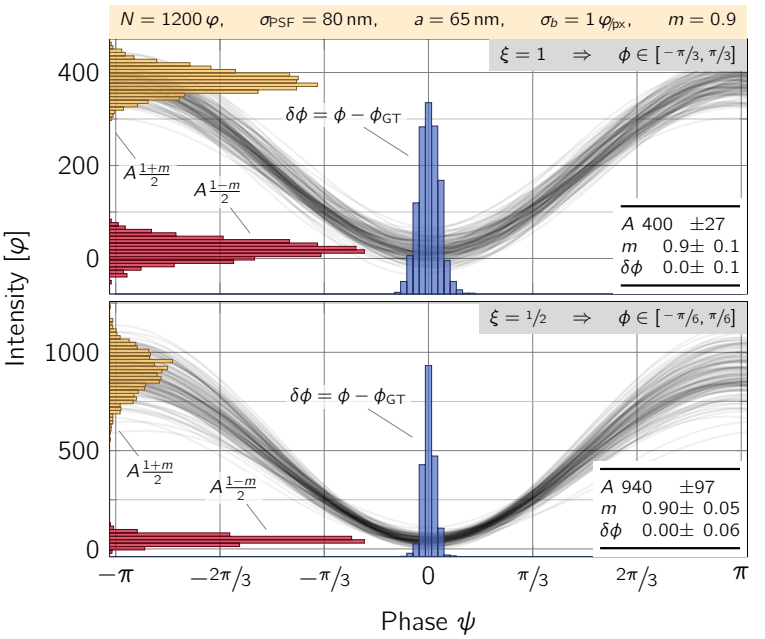

Figure III.11 – *The emitter's location is retrieved using equation* (III.19)*, applied on the recorded intensities corresponding to a series of phase-shifted pattern illuminations. The repeated deduction of fitted parameters and comparison with the ground truth (GT) allows the statistical estimation of parameters' precision.*

parameters: the fitted positions, modulations, and amplitudes are visually represented in figure III.11. The difference between the GT and estimated values of the phase position is introduced as $\delta\phi = \phi - \phi_{GT}$.

From figure III.11 the absence of bias in the estimates is clear, as the distributions are well centred on the GT values (see embedded tables). Furthermore, one sees that the the dispersion of the parameters is drastically modified by reducing the amplitude of the phase shift (*i.e.* $\xi < 1$). In particular, the dispersion –uncertainty– of $\delta\phi$ is even further reduced (approx. $2\times$) for $\xi = 1/2$ compared to the homogeneous phase shift with $\xi = 1$.

The simulation pipeline, including image generation, parameter finding, and analysis of precision is provided in listing III.2.

Code III.2 – *MATLAB code for simulating the process of SIMPLE. The lines* 1–12 *set the simulation parameters. Series or realistic images of single emitters are generated, from which the localization is retrieved through the phase. The ground truth (GT) and estimated phases are then compared and displayed in a histogram.*

```
%% Simulation paremeters
N = 1e3;                % #photons per pattern orientation
m = 1;                  % Modulation depth of the illumination
b0 = 0;                 % Background noise offset
s_b = 1;                % Background noise std (per pixel)
K = 3;                  % #phases
xi = 1;                 % Shift factor xi in (0,1]
FOV = [5,5];            % Size of the FOV in #pixels
s_psf = 80;             % PSF's standard deviation
px = 65;                % Pixel size (nm)
L = 170;                % Pattern's period (nm)
nbRep = 1e5;            % #repetition of the simulation

res = zeros(nbRep,2);   % Results matrix pre-allocation
parfor i=1:nbRep
        % Random phase
        phi = (2*pi*rand()-pi)*xi/K;
        % Random position of the emitter within a pixel
        p0 = rand(1,2)-0.5;
        % SIMPLE procedure (see function below)
        [phase,~,~] = SIMPLE(N,m,phi,p0,b0,s_b,K,xi,FOV,s_psf,px);
        % Storing results
        res(i,:) = [phi,phase];
end

% Phase: GT vs calculated. From phase (rad) to (nm)
d = L/(2*pi).*wrapToPi(diff(res')');
% Displaying results' histogram
histogram(d)
t = append("Mean=",num2str(mean(d)),"(nm), RMS=",num2str(rms(d)),"(nm)");
title(gca,t');set(gca,'YScale','log')

function [phase, im0, imSIMPLE] = SIMPLE(N,m,phi,p0,b0,s_b,K,xi,FOV,s_psf,px)
%% Definition of local functions
% Illumination pattern
illum = @(A,m,phi,psi) A/2.*(1-m.*cos(phi-psi));
% Pattern amplitude conserving N
A = @(N,m,phi,K,xi) 2*N./(K-m.*cos(phi).*csc(pi*xi/K)*sin(pi*xi));
% Phase shifts
psi = @(i,K,xi) 2*pi*xi*(i-1-(K-1)/2)/K;
% K intensities corresponding to the phase shifts
intensities = @(N,m,phi,K,xi) illum(A(N,m,phi,K,xi),m,phi,psi(1:K,K,xi));
% Read-out noise, with binomial rounding
readOut = @(ROn) floor(ROn) + binornd(1,mod(ROn,1));
% Shot + read-out noise
addNoise = @(n,s_b,b0) poissrnd(n) + readOut(normrnd(b0,s_b,size(n)));
% Gaussian spreading of the PSF, centered on p0
psf = @(p0,s_psf,n) normrnd(0,s_psf,round(n),2) + p0;
% Deletion of photons falling out of the FOV
outOfFOV = @(pos,FOV) any(pos<=0,2) | any(pos>FOV,2);
% Weighed sin/cos sum (circular statistics)
c = @(n,psi,xi) dot(n,cos(psi/xi));     s = @(n,psi,xi) dot(n,sin(psi/xi));
% Formula for retrieving the phase from the amplitudes
phiCalc = @(n,psi,xi) wrapToPi(pi+angle(complex( tan(pi/numel(n))*c(n,psi,xi), tan(pi/numel(n)*xi)*s(n,psi,xi))));

%% Image simulation
% Randomly placing N photons around p0, centered on the FOV
pos = arrayfun(@(x) ceil(psf(p0+FOV/2,s_psf/px,x)), intensities(N,m,phi,K,xi),'UniformOutput',0);
% Removing out-of-FOV photons
pos = cellfun(@(x) x(~outOfFOV(x,FOV),:),pos,'UniformOutput',0);
% Binning the photons per pixel
im0 = cellfun(@(x) accumarray(x,1,FOV),pos,'UniformOutput',0);
% Addition of the noise
imSIMPLE = addNoise(cell2mat(shiftdim(im0,-1)),s_b,b0);
% Masking of the signal
imMasked = bsxfun(@(x,y) x.*y,imSIMPLE,mask);
% Signal per image
n = sum(imMasked,1:2);
% Calculation of the phase from the modulated intensities
phase = phiCalc(n(:),psi(1:K,K,xi),xi);
end
```

III.5.1 Model/simulation comparison

The mathematical approach from sections III.3.1 and III.4 allows –under a series of assumptions– the exploration of the limits of the technique. Numerical simulations, even though computationally more demanding, constitute a powerful modular tool where those assumptions can be softened or, at times, avoided. This complementarity completes the "explorable space" of SIMPLE's parameters, allowing thorough validation of the results, and a clear definition of their limits.

This verification process –a necessary step to validate the technique before applying it to real-life samples (shown in appendix A [16] on single immobilised Alexa Fluor488 dyes) – is provided in this section where models and simulations will be compared directly. The parameters we will focus on are: the signal N, the phase position ϕ, the noise level σ_b, the modulation m, and the shift factor ξ.

Homogeneous phase-shifts with $K = 3$

The most basic illumination configuration consists of three shifted patterns (per orientation), translated each time by a third of the pattern period. The resulting illumination is homogeneous over the whole FOV which allows the straight-forward comparison with SMLM, regardless of the position of the emitter on the FOV. The modified Thompson formula [74] derived in Mortensen et al. [75] is used as the reference localization precision throughout the rest of this section.

The upper panel of figure III.12 shows the localization precision predicted by Mortensen et al. (in black) and the from UP and CRLB models (resp. in blue and purple), for a range of emitter's intensities N. The solid and dashed lines are calculated from the equations (II.17), (III.14a) and (III.61), with the parameters displayed in the yellow band above the figure.

Numerical simulations' output (green marks) are superimposed to the theoretical curves (solid lines). The synthetic data generation and

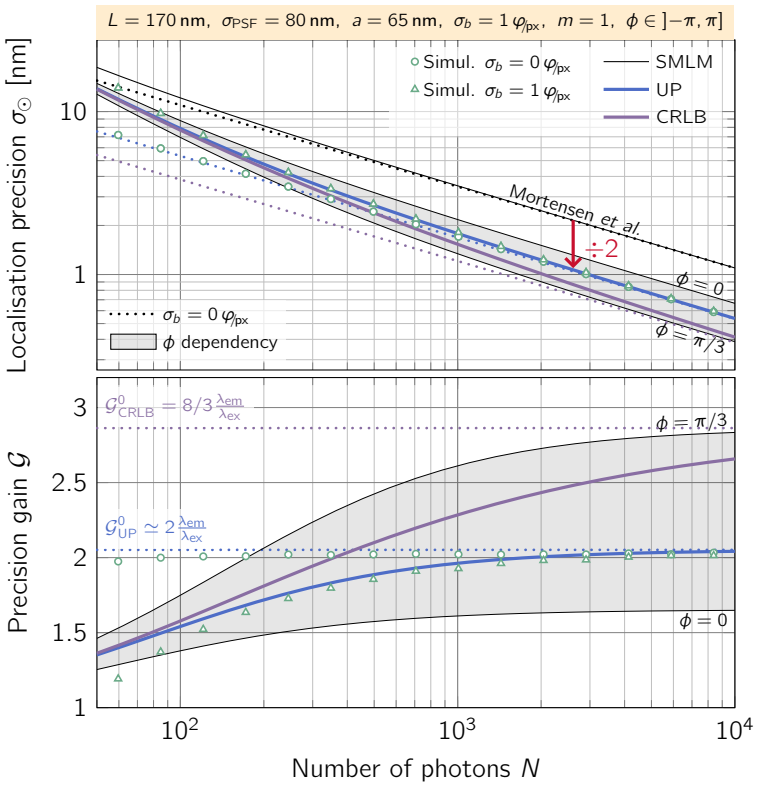

Figure III.12 – *Localisation precision (top) and gain (bottom) of SIMPLE compared to SMLM. The maximal achievable precision is estimated using uncertainty propagation (UP) in blue and Cramér-Rao lower bound (CRLB) in purple. The dependency on the phase position of the emitter ϕ is given by the grey area. Simulation results are shown with green marks (circles and triangles) at various background noise levels.*

analysis pipeline (listing III.2) accurately match UP's model, both in trend and in value. The gain (bottom panel) is calculated by dividing the localization precision by Mortensen's formula (equation (II.17)), where one sees that an average gain of around two is achieved FOV-wide. The CRLB model tends, on average, to give overly optimistic results compared to the simulations.

The discrepancy between the UP model and the simulations –more pronounced once some read-out noise is accounted for– is attributed to the image pixelation and masking whose importance is mild for higher signal-to-noise ratio (SNR) but becomes important (5–10 %) for signals below 100 φ.

Spatial dependency of the localization precision Even though the illumination is homogeneous on average, the localization precision will vary depending on the emitter's position within the illumination pattern. The range of values observed for $\sigma_{\odot}$ and $\mathcal{G}$ are represented in figure III.12 as a grey area. The detailed ϕ dependencies are shown in figures III.13 and III.16.

In accordance to the theoretical results compiled in table III.1, the influence of the emitter's phase position is different depending on the model, despite their limits being identical (with an exception in absence of noise and ideal modulation). Figure III.13 displays the precision gain for both models: UP (lower half, solid lines) and CRLB (upper half, dashed lines). We will see later on (figures III.15 and III.16) that the UP model describes better the simulation results, among others regarding the localization precision dependency on ϕ.

Effect of noise on the localization precision Real life systems unfortunately all suffer from some degree of noise that will limit the maximal precision one can expect. In figure III.14, read-out noise standard deviations σ_b of 0–2 φ_{px} are included, showing here again a very good correspondence between the theory and simulation. The same kind of discrepancy at low photon levels is observed, here again explained by the increasing importance of pixelation for such SNR.

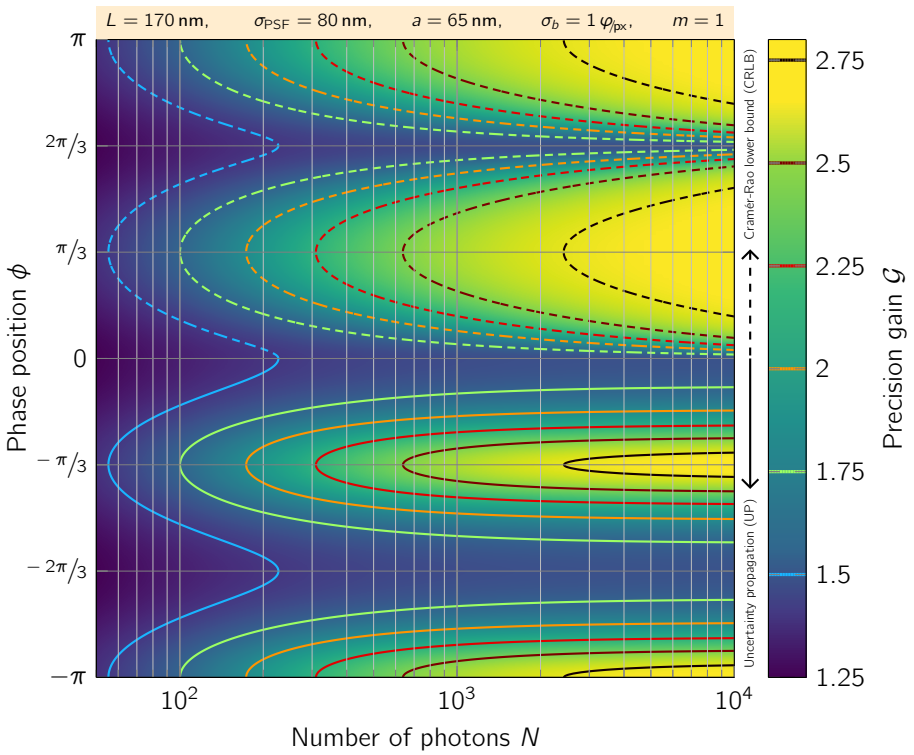

Figure III.13 – *The precision gain $\mathcal{G}$ is represented as a function of the number of photons N and the position of the emitter relatively to the phase ϕ. The upper half matches the CRLB model derived in equation* (III.61)*, whereas the lower half corresponds to the UP model from equation* (III.25a)*.*

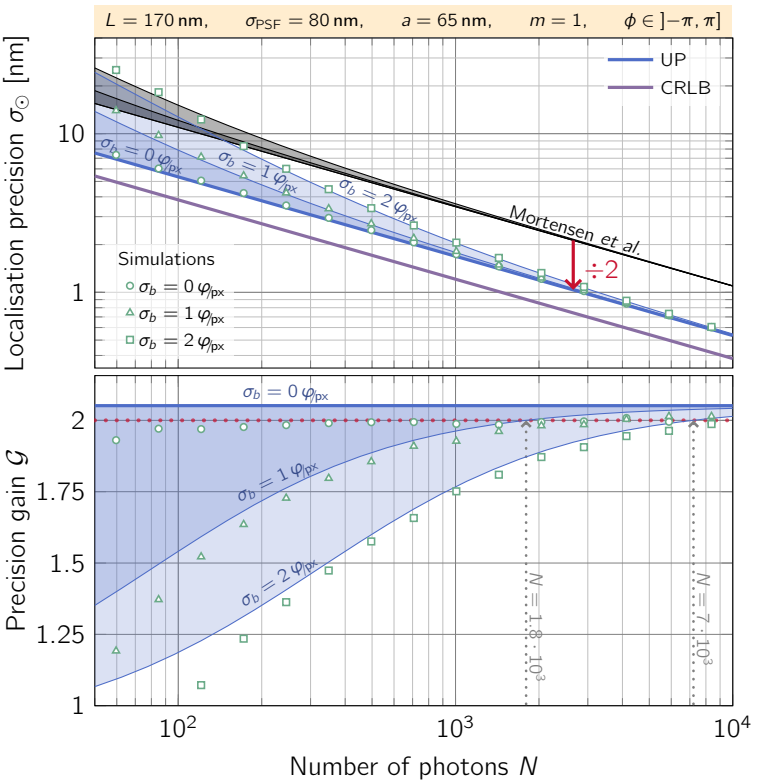

Figure III.14 – *The impact of noise levels on the localization precision (top) and gain (bottom) are illustrated as a function of the total number of photons. The theoretical results (solid lines) are compared to simulations (green marks) for noise levels up to* $2\,\varphi_{/\mathrm{px}}$.

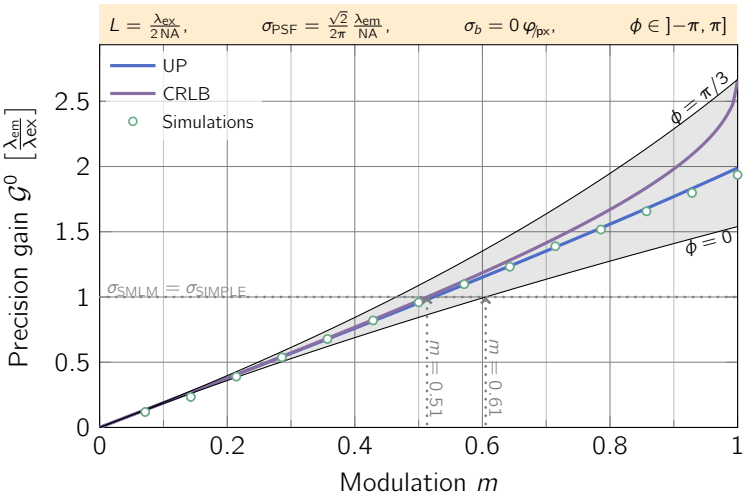

Figure III.15 – *Dependency of the localization precision's gain on the modulation. The CRLB (purple) and UP (blue) models are compared to simulated data (green marks). The range of values induced by the phase position is displayed as a grey area.*

Imperfect modulation SIMPLE, and the other meLM techniques draw their resolution power from the spatio-temporal modulation of the illumination, hence the crucial role of said modulation in the achievable localization precision and corresponding gain. In order to decouple the effect of multiple variables, we consider in figure III.15 the ideal case $\mathcal{G}^0$ from equations (III.30) and (III.31) where only the modulation is left as a parameter – in the absence of read-out noise, and using the optimal pattern period L and σ_{PSF}.

The quasi-linear behaviour of $\langle \mathcal{G}^0 \rangle_\phi$ predicted in equation (III.31) is precisely matched by the simulations (green circles). The UP model seems to be more accurate than CRLB which tends to over-estimate precision and gain.

Figure III.15, also shows that, in this ideal scenario, to achieve a minimum gain of 1 all over the FOV, a modulation above 61 % is necessary. For values of m above this threshold, the use of SIMPLE over SMLM will provide a globally enhanced localization precision.

High-gain SIMPLE: $\xi < 1$

In its implementation, MINFLUX achieves localization precision gains virtually infinite by reducing the displacement amplitude of the donut illumination. This is possible only by keeping the emitter in the region of illumination where its intensity is minimal. In this reduced portion of the FOV, emission is rarer and each detected photon carries a larger amount of information leading to the impressive results of the technique [77, 106–108].

Such high gains can also be achieved using SIMPLE, with little to no modification to the setup (see setup description in appendix A). By reducing the amplitude of the phase shifts in the illumination sequence, one obtains a very uneven average illumination over the FOV: the sum of the patterns does not compensate each other like in the previously discussed configuration. The emitters at the troughs of the pattern – around $\phi = 0 \pm n \cdot 2\pi$ – will be maintained in dim zones where the modulation of fluorescent emission carry larger amount of information per photon. Unlike MINFLUX, this technique is inherently "parallelized" as the standing-wave illumination will generate a square lattice of intensity wells separated by $L \simeq 170\,\text{nm}$; all of which simultaneously act as high-precision probes.

Figure III.16 shows both the comparison between the UP (left, solid lines) and CRLB (right, dashed lines) models and the simulation results (circles). By reducing the shift factor ξ, the precision gain peaks around $\phi = 0$, with above 10-fold gains for $\xi = 1/4$. The effect of ξ on the gain is continuous and theoretically not limited, even though in practice, the acquisition parameters and associated uncertainties will bound the maximum gain.

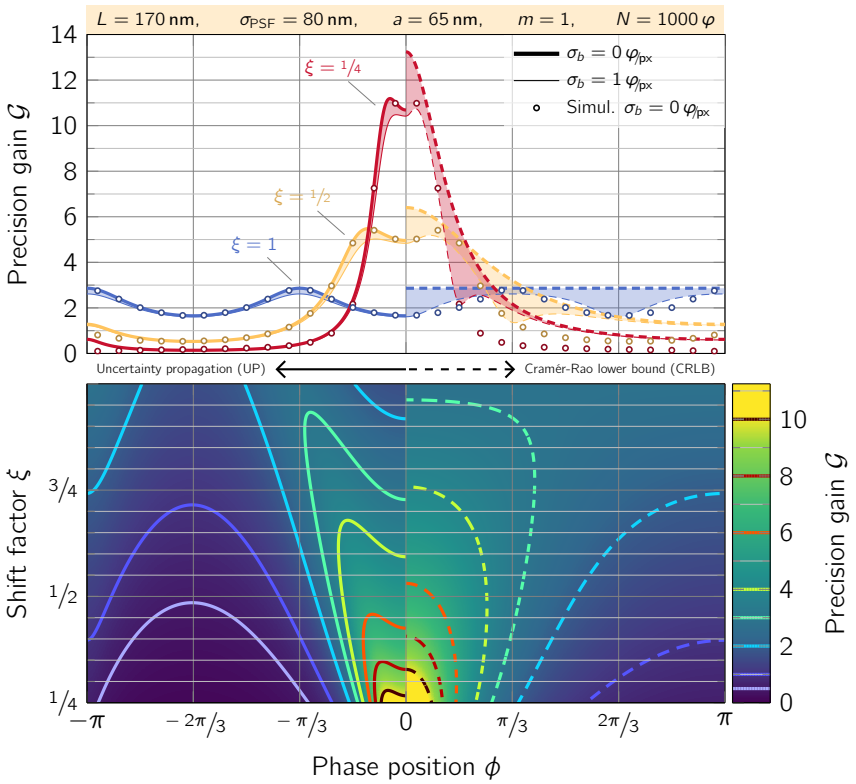

Figure III.16 – *Higher precision gains can be achieved by reducing the shift factor ξ. One sees here the role of ϕ –the relative position of the emitter on the illumination pattern– and the shift factor ξ on the attainable localization gains (equation (III.32)). On a limited region at the trough of the illumination, extreme precision can be achieved by reducing the amplitude of the illumination's shift.*

Chapter IV

Perspective: patterned illumination for nano-sizing

Now that the foundations of SIMPLE's principle have been set and its strengths/limitations identified, I would like to provide in this chapter a rather personal vision/outlook on the yet unexplored potential of modulation-enhanced microscopy. Its content aims at guiding the reader into considering a different representation for microscopy images; by describing structures (pseudo-) vectorially instead of pixel-wise.

Localization precision $\neq$ resolution Almost simultaneously after the seminal publication of MINFLUX by Balzarotti et al. in 2017, various techniques such as ROSE, SIMPLE, SIMFLUX, and ModLoc emerged, offering improved localization precision for single-molecule imaging based on the principle of MINFLUX and utilizing standing-wave illumination [16, 17, 77–79, 81].

These techniques have undoubtedly achieved remarkable advancements in localization precision. The ability to precisely determine the positions of single molecules has enabled the visualization of fixed structures with unprecedented accuracy and the tracking of particles over extended time periods with higher fidelity. However, it is important to recognize that localization precision and resolution are not synonymous, despite the initial perception that increased precision automatically leads to improved resolution [109, 110].

Resolution, in the context of microscopy, refers to the ability to distinguish two closely spaced objects as separate entities. It is a measure of the smallest resolvable feature in an image. On the other hand, localization precision pertains to the accuracy with which the position of an individual molecule can be determined within an image.

While the aforementioned techniques have achieved significant gains in localization precision, they encounter inherent limitations when it comes to resolution. The improved precision allows for more precise localization of individual molecules, but it does not necessarily enhance the ability to resolve intricate details of complex structures. This limitation becomes particularly evident in live-cell imaging, where the dynamics and complexity of the biological system can pose additional challenges.

To overcome these limitations, an extension of modulation-enhanced localization microscopy (meLM) can be proposed. This extension not only provides improved localization precision but also offers quantitative information about the structure of interest. By considering multiple molecules that are spatially related and interact with each other within the isolated structure, meLM can capture the collective behaviour and properties of the structure.

By embracing this (pseudo-) vectorial approach, the relationships and orientations of individual molecules within isolated structures can be quantitatively characterized. This extension enables the extraction of valuable quantitative information beyond what can be achieved solely through improved localization precision. It allows for a deeper understanding of the structure's properties, interactions, and dynamics, leading to enhanced resolution in a more comprehensive sense.

The following sections will demonstrate that MELM has the capability to probe the sample in a manner that directly addresses quantitative questions. This shift in focus enables a pseudo-vectorial description of nano-structures in live cells, without necessitating intricate knowledge of the photophysics of fluorophores.

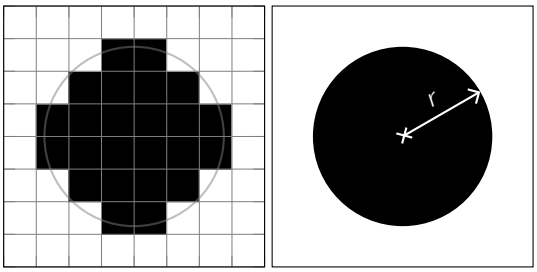

Figure IV.1 – *A disk is represented both in a pixelated (left) and vectorial way (right). The disk is ideally represented using only 3 parameters for the vectorial image, and approximately despite the 64 pixels.*

From Pixels to Vectors The prevalence of "pixelation" in our everyday life, encompassing images, screens, camera chips, and other technologies, has ingrained a bias towards thinking in pixel-based representations. However, vector graphic images offer an alternative approach where the content is parametrically represented, employing descriptive quantities instead of pixels. Consider the depiction of a disk on a binary 2D pixel grid, as shown in the left image of Figure IV.1. The disk is represented by a total of $8 \times 8 = 64$ pixels. Each pixel answers the question, "Is the disk present at this location?" Consequently, the resulting representation approximates a circle with step-like edges.

On the other hand, the right-hand side of Figure IV.1 illustrates the same circle described vectorially, employing only three parameters: the two coordinates of the centre and the radius r. With significantly fewer parameters, the shape is accurately described. The underlying questions that these parameters address are quantitative in nature: "Where is the disk?" and "What is its radius?"

By applying the principles of meLM, it becomes possible to address similar quantitative questions directly when probing nanostructures. This paradigm shift allows for a pseudo-vectorial description of nanostructures in live cells, without the requirement of complex photophysics associated with fluorophores.

IV.1 From individual emitters to sparse nanostructures

To overcome the limitations of SMLM, we aim to expand the potential applications of techniques like meLM and its variants by focusing on capturing isolated nanometric *structures*. Instead of relying solely on precise localization of individual emitters, our objective is to accurately characterize the shape, dimensions, and other properties of these sparse structures. We extend the application of meLM to sparse structures labeled with standard, non-blinking fluorophores. By leveraging patterned illumination, this approach enables the retrieval of sub-diffraction information about the dimensions of objects in various directions, using the principles of meLM and its pseudo-vectorial description.

We begin exploring this concept with a simplified case study involving a pair of emitters. Subsequently, we expand our analysis to more complex structures, demonstrating the potential of meLM in characterizing and visualizing nanometric objects with enhanced precision and accuracy.

IV.1.1 Emitter pair

When accurately representing a structure in an image formed by points, high point densities are necessary. However, achieving such densities can be challenging. Longer acquisition times can increase the number of localizations but at the expense of time efficiency. Alternatively, faster blinking or denser labelling can be employed, but this increases the risk of violating the sparsity assumption underlying SMLM, especially when two or more emitters are likely to emit simultaneously in close proximity. While co-localizations can be filtered out based on an arbitrary criterion in ideal scenarios, some may persist and be erroneously positioned, leading to increased uncertainty or even misleading interpretations. Moreover, accurately measuring the distance between two emitters becomes infeasible if they are closer than the diffraction limit (d_{Abbe}) and present simultaneously.

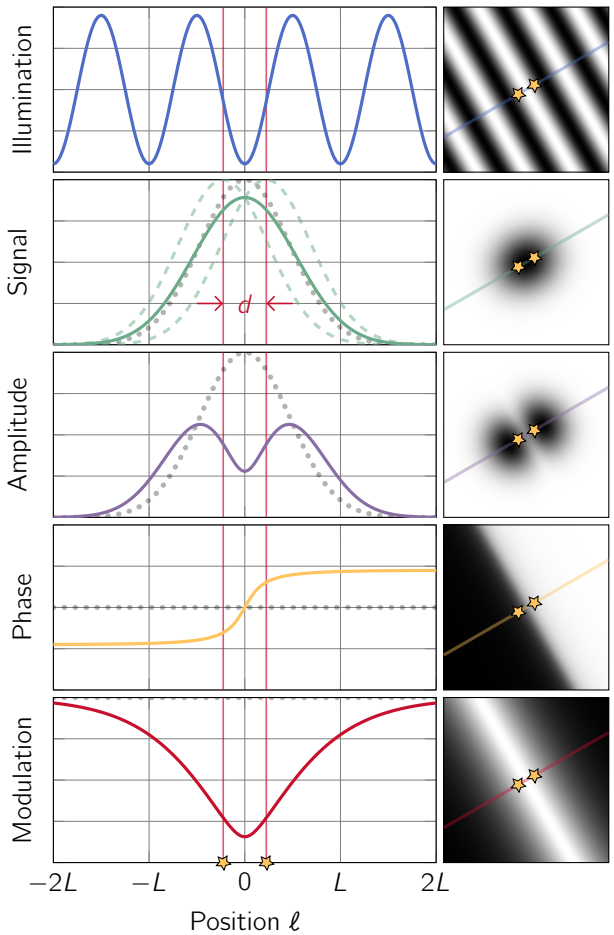

Figure IV.2 – *The space of amplitudes A, phase ϕ, and modulation m provides a complete base to describe images. From these parameters one can uniquely deduce the spacing d between two close-by emitters (stars). The grey dotted lines, provided for comparison, correspond to the single emitter case. The green dashed lines in the second panel represent the signal coming from each emitter if considered individually.*

By using the spatio-temporal modification of the signal driven by the illumination pattern, one could easily differentiate between single emitters and clusters of them. It is demonstrated in figure IV.2, where the grey dotted lines correspond to a single emitter and the coloured ones to a pair of them (shown as stars). The total signal (second panel, green), corresponding to a widefield image, is extremely similar whether one or two emitters are present: both look like a regular PSF. At this distance $d = 0.45 \cdot L \simeq \sigma_{\text{PSF}}$, the signals of the two emitters blend, making it difficult to dissociate. However, if one looks at the other quantities characterising the results of SIMPLE (A, m, ϕ), one sees a striking difference between the two cases: the spatial distribution of the amplitude A, phase ϕ, and modulation m are strongly modified by the distribution of emitters.

Figure IV.3 shows a very similar scenario involving two emitters (stars) separated by a distance $d = 2/5L \simeq 70\,\text{nm}$. As the illumination (left panel, blue) travels through the sample, the experienced illumination intensity of each of the emitters is modulated (centre left). As the two emitters are not at the exact same location, their relative signal intensities will be different and "pull" the total signal's centroid on one side or the other depending on the pattern's position (centre right, green). This "wiggling" effect is depicted on the rightmost panel, where the lighter line shows how the signal's centroid is displaced as the pattern is translated.

Taking advantage of this information-rich effect would allow for efficient filtering of parasitic co-localizations. Moreover, the collection of $\{A \times m \times \phi\}$ maps (right column in figure IV.2 and in figure IV.4) are effectively a change of representation from the raw intensity images, and fully encode the information of the fluorescent structures. This *signature*, is unique to a nano-structure, and besides carrying information about its location, it also provides clues about its size and shape.

To further demonstrate the potential of this $\{A \times m \times \phi\}$ representation, one sees in figure IV.4, that by varying the separating distance between two emitters (vertical axis), this representation is highly sensitive to sub-diffraction arrangements of emitters: enhanced contrast is visible

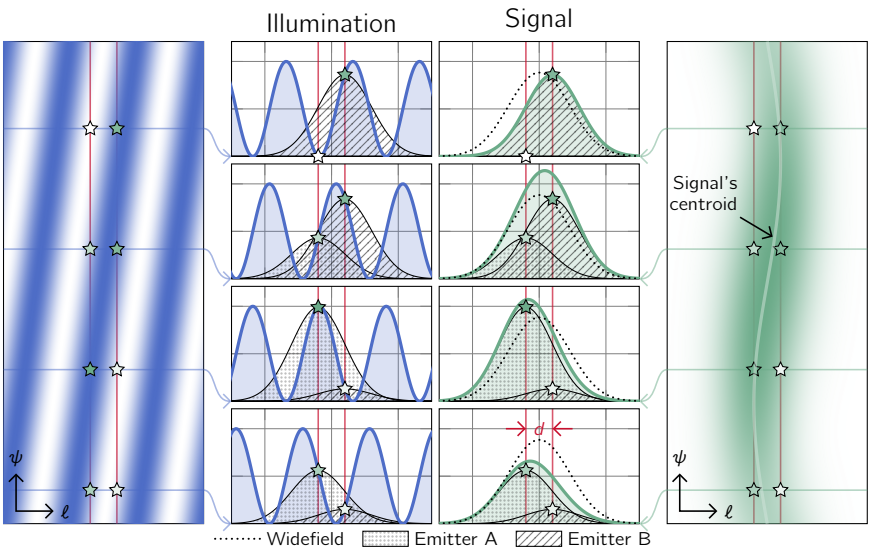

Figure IV.3 – *Two emitters (stars), separated by* $d = 2/5L \simeq 70\,\text{nm}$ *(spacing of the red vertical lines) see their emission modulated by the translation of the illumination (in blue). Their individual and combined signal is represented respectively by the black textured and green curves. The panel on the right, shows that the signal's centroid moves along the pattern's direction* ℓ *as it is translated, i.e. phase-shifted* ψ*.*

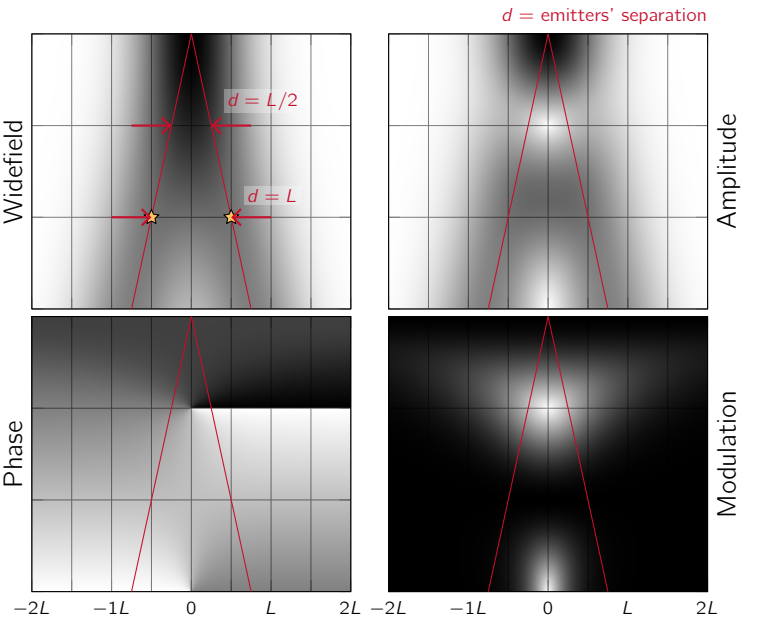

Figure IV.4 – *As the distance between two emitters is modified, the amplitude, phase, and modulation profiles are modified. The widefield image (top left) does not allow the clear distinction between the emitters below $d = L$ whereas the $\{A \times m \times \phi\}$-images provide contrast for $d \geq L/5 \simeq 35\,\text{nm}$.*

for all three $\{A \times m \times \phi\}$ panels, at separation distance below 80 nm, whereas the widefield image (top left) does not. Quantitative information about sizes can be retrieved using fitting procedures or eventually machine-learning (ML). The key principle of this analysis is presented here only conceptually as a more extensive discussion would fall outside of the scope of this thesis.

Besides improving details, representing the data as an amplitude, phase and modulation instead of intensities is physically more relevant: the information contained as photon counts in the raw images is separated based on their physical meaning.

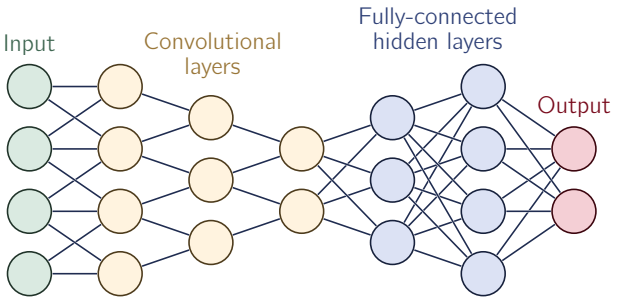

Figure IV.5 – *Graphical representation of a neural network (NN). The values of each pixels are fed into the NN, which will, through a series of layers, mix the information they contain and provide the output the network has been trained for.*

Machine-learning: In the recent years, many applications of machine-learning (ML) have flourished within the field of microscopy [65, 66, 111–115]. Trained on dedicated images databases, these applications generally aim at providing solutions to de-noising, artefact-free reconstructions, or faster treatment of data [116–118].

Figure IV.5 illustrates how, in a neural network, the input information (usually pixel intensity values), is mixed together to generate an output; each circle represents a "node" taking as input some values from the previous layer to which a basic mathematical operation is applied and propagated towards the next layer*. The type of operation a node can perform is limited: the training phase – adjusting the network to give the desired output – is an iterative back-and-forth process requiring the quasi-linearity (and/or bijectivity) of each operation. This optimization procedure is based on a "distance" measure, called merit function, between the target output (known) and the one obtained by the NN.

A concern one might have in using ML for super-resolution microscopy is the lack of physicality of the internal mechanisms of the ML process. The combination of values – initially carrying a physical meaning – is not guaranteed as the inputs are scrambled through the different network's layers. To circumvent this drawback, some models rely on phys-

*The displayed NN is a simplified version of a network's architecture: typically containing millions to billions of nodes.

ically relevant merit functions that assess the quality of a NN output, which are then called physics-informed neural network (PINN) [119, 120]. Using a physically more meaningful representation of the input data might allow improvements in the quality of a NN output as well as a drastic increase in readability/interpretability of the results. To this end, formatting the images as $\{A \times m \times \phi\}$, with the relevant physical constrains applied during the training process is surely beneficial; the intensity data is pre-processed with the known underlying physical processes at play.

IV.1.2 Complex structures

The previous discussion primarily focused on 1D structures, specifically a system of emitter pairs. However, to match the complexity encountered in real-life samples, it is essential to extend this line of reasoning to more complex structures.

In addition to its ability to improve details and resolve sub-diffraction arrangements, the $A \times m \times \phi$ representation holds great potential for analysing complex structures in biological systems. By applying the principles of this representation to intricate systems such as multi-component cellular structures or dynamic molecular assemblies, valuable insights into their spatial organization and behaviour can be extracted. This extension enables detailed sizing and characterization along different axes, facilitating a comprehensive understanding of the complexity and dynamics of biological structures.

The sizing capabilities inherent to the $A \times m \times \phi$ signature are revealed through the illumination pattern along its direction. Similar to rotating a ruler to measure different faces of an object, rotating the illumination provides insights into a structure's dimensions along various axes. Since the underlying true structure is unknown, an approximation can be made by constructing an ellipse from the various size measurements obtained during the rotation of the illumination profile.

Using an illumination sequence identical to TIRF-SIM figure IV.6 shows how, from three sizes (dotted arrows) extracted from the $\{A \times$

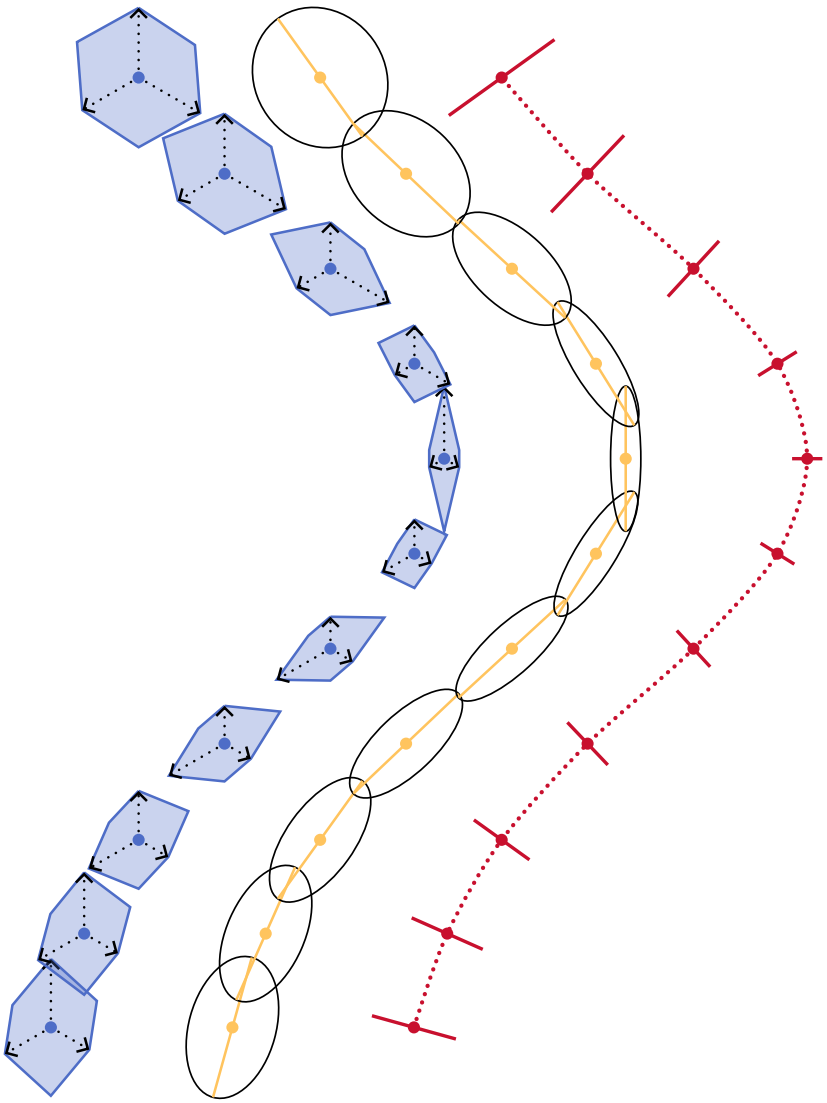

Figure IV.6 – *By measuring the dimensions along different axis at various locations of an arbitrary structure (here, a bent filament with changing width), one can weave the points together and create a smooth profile with varying thickness. The measured dimensions (blue hexagons) obtained by $\{A \times m \times \phi\}$-analysis are then extrapolated to ellipses (black) which are then linked together (red, dotted). The structure's thicknesses along its path (red, solid) correspond to the minor axis of the ellipses.*

$m \times \phi\}$'s signature (p.ex. through fitting), one could approximate the local shape of the observed structure. Centred on the signal's centroid, the smallest convex shape matching the measured dimensions is an hexagon, shown in blue in figure IV.6. From this hexagon, one can extrapolate the object's local shape by constructing its circumellipse – the smallest ellipse engulfing the hexagon that shares its centre. Repeating this process and identifying the overlapping ellipses, the discrete sampling points could be weaved together to form complex structures along which one could know the width with unprecedented precision.

In conclusion, the $A \times m \times \phi$ representation offers a powerful approach for microscopy imaging and analysis. By capturing the amplitude, phase, and modulation information of signals, this representation provides enhanced contrast and improved resolution, particularly for sub-diffraction arrangements of emitters. Its combination with machine learning techniques holds great potential for advancing super-resolution microscopy, allowing the incorporation of physical constraints and improving interpretability of results.

The applicability of the $A \times m \times \phi$ representation extends to the study of biological systems, where it offers significant advantages. For example, it enables the investigation of protein arrangements, organelle interactions, and other cellular components, providing insights into fundamental biological mechanisms such as signal transduction, molecular transport, and cell division.

Moreover, this representation enhances the study of subcellular structures and their dynamics. Accurate measurements of sizes and shapes of cellular organelles contribute to a deeper understanding of their functions and their role in cellular processes. Additionally, the quantitative information extracted from the $A \times m \times \phi$ representation allows for the analysis of dynamic changes in biological systems over time, including protein-protein interactions, membrane dynamics, and cellular responses to external stimuli.

In summary, the $A \times m \times \phi$ representation offers a versatile and powerful tool for studying biological systems, providing improved resolution, enhanced contrast, and quantitative analysis capabilities. Its

application spans various areas of biology, including cellular imaging, subcellular structure characterization, and the study of dynamic processes. By leveraging the advantages of this representation, researchers can gain deeper insights into the intricate workings of living systems and contribute to advancements in cell biology, molecular biology, and biomedical research.

Conclusion

In order to provide context and complementary information to the publications forming the *corpus* of this thesis (see appendices A to C), I have first briefly presented the history of major discoveries related to light microscopy. Then, I introduced the key concepts on which fluorescence light microscopy is based and the challenges imposed by the diffraction limit on the observation of sub-cellular structures in biology.

After explaining the basics of the state-of-the-art super-resolution modalities (TIRF, STED, SIM, and SMLM), I introduced SIMPLE, the technique we developed based on MINFLUX.

I have shown theoretically and through simulations that using a standing-wave patterned illumination in combination with SMLM provides a 2-fold improvement in localization precision across the field of view compared to standard techniques. Even higher – and virtually infinite – gains can be achieved at specific locations on the sample by modifying the illumination sequence: a dark-spot lattice offers a parallelized version of MINFLUX, probing various loci at once with extremely high photon-efficient localization precision.

These results have been obtained using uncertainty propagation (UP) method and via the Cramér-Rao lower bound (CRLB), giving easily computable limits in a wide range of imaging conditions (signal intensity, noise, modulation depth). Furthermore, we have observed that the equations derived from the UP approach are in quasi-perfect accordance to the simulated results, consolidating its validity.

Experimental results on isolated emitters ("SIMPLE: Structured Illumination Based Point Localization Estimator with Enhanced Precision" [16]) have been shown to match the theoretical predictions. The imple-

mentation of a custom-built digital micro-mirror device (DMD) based high-NA TIRF-SIM setup allowed an effective doubling of localization precision homogeneously over a 400 μm^2 FOV. In high-gain regimes, gains of 6.5$\times$ have been recorded ("Modulation-Enhanced Localization Microscopy" [17]) further validating the potential of SIMPLE.

The class of techniques applying a modulated illumination to improve localization precision to which SIMPLE pertains, has been grouped ("Modulation-Enhanced Localization Microscopy" [17]) under the name of modulation-enhanced localization microscopy (meLM), that gave its title to this thesis.

Finally, we explored possible extensions of meLM for direct size measurement of sparse nano-structures. Based on a drastic change of image representation (pseudo-vectorial description of features), such improvements would circumvent part of the limitations imposed by SMLM, and allow the study of dynamical structures with minimal experimental complexity (standard fluorophores and regular SIM setup).

In summary, the use of patterned illumination has been proven to improve localization precision in SMLM and could potentially be applied to live-cell nano-sizing.

Appendix A

SIMPLE: Structured illumination based point localization estimator with enhanced precision

L. Reymond et al., "SIMPLE: Structured illumination based point localization estimator with enhanced precision", Optics Express **27**, 24578 (2019)

Abstract We present a structured illumination microscopy based point localization estimator (SIMPLE) that achieves a 2-fold increase in single molecule localization precision compared to conventional centroid estimation methods. SIMPLE advances the recently introduced MINFLUX concept by using precisely phase-shifted sinusoidal wave patterns as nanometric rulers for simultaneous particle localization based on photon count variation over a 20 µm field of view. We validate SIMPLE in silico and experimentally on a TIRF-SIM setup using a digital micro-mirror device (DMD) as a spatial light modulator.

Research Article | Vol. 27, No. 17 | 19 Aug 2019 | OPTICS EXPRESS 24578
Optics EXPRESS

SIMPLE: Structured illumination based point localization estimator with enhanced precision

LOÏC REYMOND,[1,2,5] JOHANNES ZIEGLER,[1,5] CHRISTIAN KNAPP,[1] FUNG-CHEN WANG,[3] THOMAS HUSER,[3] VERENA RUPRECHT,[2,4] AND STEFAN WIESER[1,*]

[1]*ICFO – Institut de Ciencies Fotoniques, The Barcelona Institute of Science and Technology, 08860 Castelldefels, Spain*
[2]*Centre for Genomic Regulation (CRG), The Barcelona Institute of Science and Technology, 08003 Barcelona, Spain*
[3]*Department of Physics, University Bielefeld, 33615 Bielefeld, Germany*
[4]*Universitat Pompeu Fabra (UPF), Barcelona, Spain*
[5]*These authors contributed equally to this work.*
[*]*stefan.wieser@icfo.eu*

Abstract: We present a structured illumination microscopy based point localization estimator (SIMPLE) that achieves a 2-fold increase in single molecule localization precision compared to conventional centroid estimation methods. SIMPLE advances the recently introduced MINFLUX concept by using precisely phase-shifted sinusoidal wave patterns as nanometric rulers for simultaneous particle localization based on photon count variation over a 20 µm field of view. We validate SIMPLE *in silico* and experimentally on a TIRF-SIM setup using a digital micro-mirror device (DMD) as a spatial light modulator.

© 2019 Optical Society of America under the terms of the OSA Open Access Publishing Agreement

1. Introduction

Super-resolution (SR) imaging has become an enabling technology to access sub-diffraction information on the nanoscale structure and dynamics of molecular building blocks [1]. Different SR concepts have been introduced: Single molecule localization microscopy (SMLM) methods such as PALM [2] and STORM [3] process information in the optical detection path to estimate single particle positions of sparse emitters by centroid fitting to the diffraction-limited photon distribution on a pixelized camera. Each individual photon contributes to a measure of the actual particle position with a standard deviation s given by the point spread function (PSF) of the imaging system. The localization precision of SMLM scales with $s \propto \lambda/\mathrm{NA}$, with λ being the fluorescence emission wavelength and NA the numerical aperture of the detection objective. An increasing number of photons N results in a higher localization precision given by the standard error of the mean $\Delta x = s/\sqrt{N}$, with conventional SR localization methods reaching $\Delta x = 5 - 20\,\mathrm{nm}$ [4, 5]. In contrast, excitation-based SR concepts such as PSF-shaping [6] or structured illumination microscopy (SIM) [7–10] have been implemented. SIM enables sub-diffraction imaging by exciting samples features with periodic patterns to obtain high frequency information via the Moiré effect [10]. Typically, 3×3 phase-shifted and rotated sinusoidal interference-patterns are used and image stacks are mathematically processed to reach a 2-fold resolution improvement [11]. MINFLUX [12, 13], on the other hand, was recently introduced as a radically new concept for particle localization at minimum photon budget with up to 8-fold improvement in localization precision compared to SMLM. In MINFLUX, a single molecule emitter is probed with the central part of a doughnut-shaped illumination pattern over a restricted area of diameter $L \simeq 50\,\mathrm{nm}$. The particle position is estimated via a triangulation principle from photon count variations at different scan positions with a localization precision $\sim L/\sqrt{N}$ [12] MINFLUX is, however, limited to a restricted sub-diffraction field of observation and low

#370102 https://doi.org/10.1364/OE.27.024578
Journal © 2019 Received 14 Jun 2019; revised 29 Jul 2019; accepted 1 Aug 2019; published 14 Aug 2019

Optics EXPRESS

temporal sampling due to sequential scanning of single molecule emitter positions in addition to technical challenges of accurate doughnut generation and positioning. Here, we present a structured illumination microscopy based point localization estimator (SIMPLE), that allows for the simultaneous localization of isolated emitters via detection of photon count modulations on a camera-based system. We show that phase-shifted sinusoidal excitation patterns can be used as nanometric rulers for deriving the actual positions of multiple single molecule emitters in a micron-sized field of view (FOV), thereby overcoming current spatial and temporal sampling restrictions of MINFLUX.

2. Basic concept and principle of SIMPLE

The principle of the SIMPLE method is exemplified in Fig. 1. A sinusoidal wave pattern illuminates the sample and modulated photon numbers are collected from isolated emitters depending on their relative position within the excitation pattern. Phase shifting of the illumination pattern can be performed with nanometric precision (<1 nm) to probe the actual particle position through photon number variations n_i for different phase shifts Φ_i.

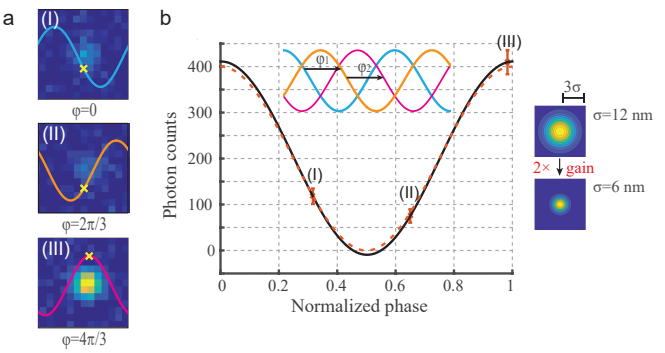

Fig. 1. The SIMPLE concept. (a) Three precisely phase-shifted sinusoidal patterns are used for illuminating a single point emitter. The sinusoidal wave serves as a nanoruler to position a single molecule emitter from which phase-dependent photon counts (n_1 = 119 (Φ_1), n_2 = 73 (Φ_2), n_3 = 410 (Φ_1)) are obtained depending on its relative position (I-III) within the sinusoidal wave. Photon counts n_i (red) are fitted with a sine function with three fit parameters (amplitude A, phase ϕ, offset b) to reveal the actual position ϕ within the wave that is mapped to the pixel image coordinate system. (b) In the case of three equally spaced phases ($\delta\Phi = 1/3$) we find a 2-fold gain in localization precision compared to SMLM (2× smaller standard deviation σ of normally distributed localization points).

The measured photon counts n_i can be fitted to the known sinusoidal illumination pattern to derive the actual particle position based on the assumption of a quasi linear response of the fluorescence emission. As $x-y$ positions can be determined independently, using two orthogonal illumination patterns is sufficient for homogeneous 2D localization of a particle emitter. This principle differs both from conventional SIM and standard SMLM approaches which rely on complex image reconstruction via Fourier methods [14] or centroid fitting of a Gaussian function to the diffraction-limited photon distribution [15], respectively. The localization precision of SIMPLE can be evaluated using error propagation analysis and estimation of the Cramer-Rao Lower Bound (CRLB) as derived previously [12, 16, 17]. In brief, a simplified estimation is based on considering photon shot noise ($\sigma_{\text{shot}} \propto \sqrt{n_i}$) that will introduce localization errors (see

Optics EXPRESS

Fig. 1(b)). Using $k = 3$ equidistant phase shifts, we can solve three equations for the detected photon counts n_i using a sine function $I = A/2\,(1 + \cos(2\pi\,(x + \phi))) + b$ with amplitude A, phase ϕ and background b:

$$A = \frac{2\sqrt{2}}{3}\sqrt{(n_1 - n_2)^2 + (n_1 - n_3)^2 + (n_2 - n_3)^2} \tag{1}$$

$$\phi = -\frac{1}{\pi}\arctan\left(\frac{-2n_1 + n_2 + n_3 + \sqrt{2}\sqrt{(n_1 - n_2)^2 + (n_1 - n_3)^2 + (n_2 - n_3)^2}}{\sqrt{3}(n_2 - n_3)}\right) \tag{2}$$

$$b = \frac{1}{3}\left(n_1 + n_2 + n_3 - \sqrt{2}\sqrt{(n_1 - n_2)^2 + (n_1 - n_3)^2 + (n_2 - n_3)^2}\right) \tag{3}$$

As the phase ϕ encodes the position, relative to the illumination, the localization precision is sensitive to the variation of the number of photons n_i.

$$\Delta\phi = \sqrt{\sum_i \left(\frac{\partial\phi}{\partial n_i}\Delta n_i\right)^2} \tag{4}$$

$$\frac{\partial\phi}{\partial n_1} = \frac{\sqrt{3}(n_2 - n_3)}{2\pi\left((n_1 - n_2)^2 + (n_1 - n_3)^2 + (n_2 - n_3)^2\right)} \tag{5}$$

$$\frac{\partial\phi}{\partial n_2} = \frac{\sqrt{3}(n_3 - n_1)}{2\pi\left((n_1 - n_2)^2 + (n_1 - n_3)^2 + (n_2 - n_3)^2\right)} \tag{6}$$

$$\frac{\partial\phi}{\partial n_3} = \frac{\sqrt{3}(n_1 - n_2)}{2\pi\left((n_1 - n_2)^2 + (n_1 - n_3)^2 + (n_2 - n_3)^2\right)} \tag{7}$$

Using the fact that the photon count follows Poisson statistics, one can write $\Delta n_i = \sqrt{n_i} + \sigma_i$, including an extra term σ_i for the background standard deviation in which the read-out noise, dark current, etc. can be embedded. A simple formula, where $N = n_1 + n_2 + n_3$ is the total number of detected photons and ℓ is the pattern period, can be derived for specific cases and for identical background fluctuations, i.e. $\sigma_i = \sigma$, $\forall i = 1, 2, 3$

$$\Delta\phi = \frac{\ell}{N}\frac{\sqrt{3}}{2\pi}\left(\sqrt{2}\sigma + \sqrt{N}\right), \quad \text{and for } \sigma = 0, \quad \Delta\phi = \frac{\ell}{\sqrt{N}}\frac{\sqrt{3}}{2\pi} \tag{8}$$

for the case that the emitter is located exactly in the valley of the illumination for one of the phase-shifts, with ℓ being the pattern period. Furthermore, we obtain

$$\Delta\phi = \frac{\ell}{N}\frac{1}{2\pi}\left(\sqrt{6}\sigma + \sqrt{N}\right), \quad \text{and for } \sigma = 0, \quad \Delta\phi = \frac{\ell}{\sqrt{N}}\frac{1}{2\pi} \tag{9}$$

if the emitter falls exactly on the peak. In the case of $\sigma = 0$ and using $s \propto \lambda/(4\mathrm{NA})$ as the standard deviation of the PSF and a pattern period of $\ell = \lambda/(2\mathrm{NA})$, the gain in localization precision of SIMPLE compared to SMLM depends on the position of the phases relative to the emitter, with $s/\Delta\phi = 1.81$ if one phase is at the minimum or $s/\Delta\phi = 3.14$ at the peak (see Fig. 3(c)). Smaller phase shifts can further enhance the localization precision at the expense of unequal localization gain in the illumination pattern.

Optics EXPRESS

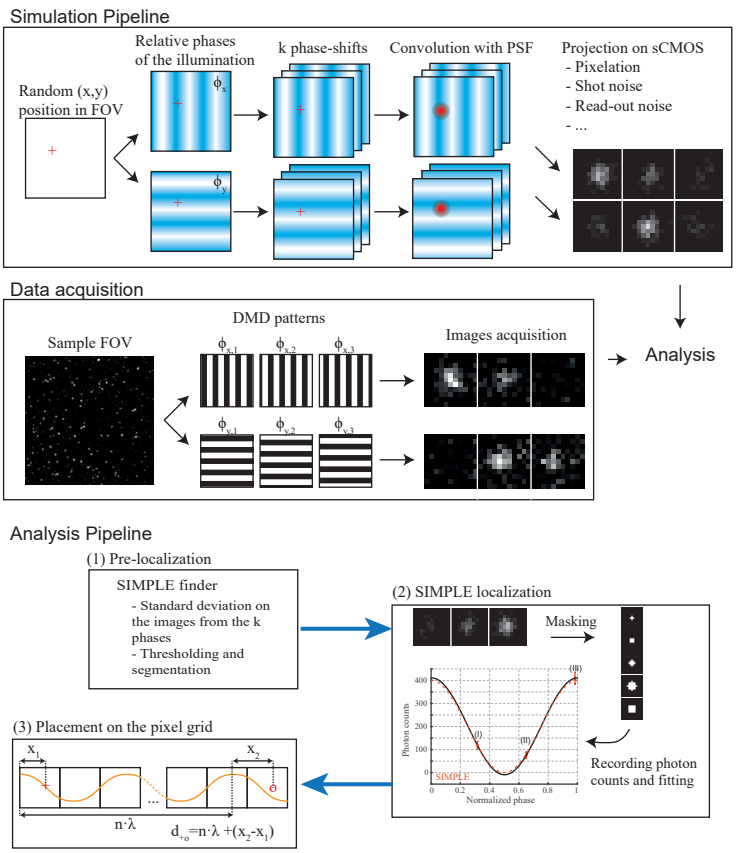

Fig. 2. Simulation and data analysis pipeline. Synthetic data are generated using random positions of single molecule emitters in $k = 3$ phase shifted illumination patterns with modulation depth m. The photon emission process is modeled as a linear response to the actual illumination intensity with Poissonian distributed photon counts. Photon positions are further normally distributed around the initial single emitter position with a standard deviation based on a defined PSF of the imaging system on a pixelized camera system. Subsequently a white noise contribution is superimposed on the image to account for read-out noise and autofluorescence in fluorescence imaging. For data acquisition, $k = 3$ phase shifted images are recorded for each direction. Data analysis first predefines pixels with high modulation contrast. In the next step, a mask (see Fig. 4) around the predefined pixel reads the number of photons. The number of photons at the three phase positions are fitted with a sine function to extract the actual position of the particle.

Optics EXPRESS

3. Methods

3.1. In silico validation of the SIMPLE concept

To validate the SIMPLE concept under realistic parameter settings, we developed an extensive simulation pipeline to generate synthetic imaging data that include relevant sources of experimental uncertainties. A fluorescent emitter is placed at a random location in the field of view. The initial phases in x and y direction, relative to the illumination pattern, are also randomized. Intensity-modulated emission counts are obtained for a series of k phases in each x and y direction, assuming a linear response of the fluorophore to the illumination. The appropriate photon spread is modeled by a Gaussian PSF on a pixelated camera chip, including photon shot noise with a Poissonian distribution. In addition, background noise is added to each pixel to mimic additional noise terms from the optical detection system or sample such as camera read-out noise, dark-current or background fluorescence. The simulations further enable to include particle characteristics such as emitter size, blinking or photo-bleaching and optical characteristics of the excitation pattern as the sinusoidal wavelength and modulation depth m. Realistic units are set by the average number of emitted photons per second and the illumination time. Synthetic data are read into our analysis pipeline to obtain the number of photons on selected pixels for an estimation of the particle position. First a pre-estimation of the emitter's location on the pixel grid is performed. This step is achieved on all associated image triplets of the FOV using a threshold for the standard deviation of photon counts during the phase shifts. Selected candidates are used for cropping the surrounding pixels with specific masks to read the number of photons for each selected emitter during phase modulation. Next, the intensity profile is fitted with a sinusoid, providing an accurate estimation of the position. Each emitter, for which the corresponding relative position on the illumination pattern has been determined through fitting, can be mapped back onto the pixelated grid of the camera. The absolute distance between the emitters is calculated as shown in Fig. 2, counting the number of wave periods and separating them accordingly. Complementarily, event detection can be obtained from summing phase shifted images to achieve a homogeneous illumination condition to reconstruct a wide-field image and using centroid-based event detection schemes as available by the ThunderSTORM plugin of Fiji [18] which is used for comparison to SIMPLE.

Figure 3 shows the comparison between SIMPLE and SMLM in the presence of a background noise of $b = 0$, 2, 4 and 6 counts/pixel. The theoretical limit of classical SMLM localization precision as described by Mortensen et al. [19] is shown in black, highlighting the localization precision improvement of SIMPLE over SMLM. Three equidistant phase shifts are sufficient to determine the emitter's position. A higher number of phase shifts Φ_i slightly lowers the localization precision due to a spread of total photons across multiple images ($\sum n_i = \text{const.}$), particularly relevant for low photon counts as obtained for dim fluorophores or fast imaging conditions. A typical camera read-out noise of 1 photon/pixel sets a lower bound to σ that will be increased by additional noise sources such as sample background, auto-fluorescence and out-of-focus fluorescence. Equidistant phase shifting yields a 1.8 to 3.1-fold improvement in localization precision depending on the emitter position relative to the wave pattern and is largely independent of the number of detected photons. A reduced modulation depth $m < 1$ of the excitation pattern will further lower the localization precision. The residual illumination generates an offset of $1 - m$ unmodulated photon counts which can be considered as an increase in the effective background noise of the sample (see Table 3.1).

The optimal pixel selection can be set in dependence on the relation PSF size/pixel size and the background noise level as shown in Fig. 4. Masks that are too small will reduce the available photon information while masks that are too big will enhance the fluctuations in the case of high background noise.

Optics EXPRESS

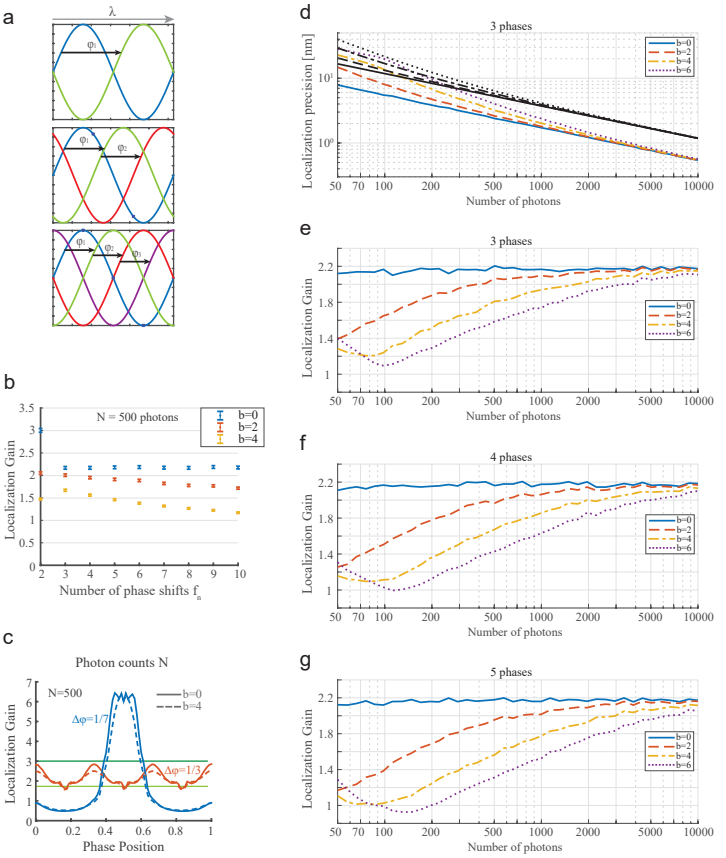

Fig. 3. Comparison of localization precision between SIMPLE and SMLM (a) Illustration of equidistant phase shifting for increasing number of phase shifts (b) Localization gain of SIMPLE versus SMLM for $N = 500$ photons for increasing number of phase shifts and various background noise $b = 0$, 2 and 4 counts/pixel. More phase shifts Φ_i result in a larger number of fitting points at the expense of fewer photons per phase shift. In all cases the sum ($\sum n_i$) over all phases is kept constant. (c) The localization gain for equally distributed phase shifts with $\delta\Phi = 1/3$ slightly depends on the actual position within the period (red) reaching localization improvements of about 1.8 to 3.1-fold. For three smaller phase shifts with $\delta\Phi = 1/7$ (blue) we find a pronounced improvement if the particle is located near the excitation minimum. Green lines indicate theoretical limits of particle localization precision in the minimum (light green) and at the peak (dark green). (d-g) Comparison between SIMPLE and SMLM in the presence of background noise $b = 0$, 2, 4 and 6 counts/pixel. The theoretical limit of classical SMLM localization precision derived by Mortensen et al. [19] is shown in black (d), highlighting the localization precision improvement of SIMPLE over SMLM.

Optics EXPRESS

Table 1. Estimation of the equivalent noise for a reduced modulation depth m.

Modulation depth	Number of photons		
	500	1000	5000
0.9	2-3	3-4	7-8
0.92	2-3	~ 3	5-6
0.94	1.2	2-3	3-4
0.96	1.2	2-3	2-3
0.98	0-1	1-2	1-2
1	0	0	0

3.2. Experimental setup

We experimentally validated the SIMPLE concept on a novel custom-built TIRF-SIM setup (Fig. 5). The optical design is based on the use of a spatial light modulator (SLM) that allows for ultra-fast pattern generation with high modulation depth and ultra-precise phase shifting of orthogonal patterns. In general, the concept of SIMPLE relies on the exact knowledge of the patterns' phase shifts, which we accomplish by using a digital micro-mirror device (DMD) as SLM. The DMD (DLP V-9501 VIS, VIALUX, pixel pitch 10.8 µm) can operate at ~17 kHz switching rate, allowing for fast imaging in the millisecond range. The de-magnification of the DMD plane to the sample plane amounts to a factor of 300, resulting in a sinusoidal interference pattern on the sample with a period of 170 nm (see Fig. 5(b-g)). This corresponds to an excitation numerical aperture (NA) of 1.44 of the first orders. The DMD also serves as master clock for the trigger protocol.

The detailed optical path of the setup comprises the excitation laser with 500 mW power at 473 nm wavelength (gem473, LaserQuantum), followed by a 10× telescope (AC080-010-A-ML and AC254-100-A-ML, Thorlabs) to expand and collimate the laser beam. The diffracted light from the DMD is collected by a lens (AC508-500-A-ML, Thorlabs) and passes through a quarter wave plate (AQWP05M-600, Thorlabs), generating circular polarization. Two neutral density filters (NDC-50C-2, Thorlabs) provide fine control over the intensities of the individual diffracted beams. A custom aluminum mask is placed in the Fourier plane of the DMD and serves as spatial filter to block unwanted diffraction orders originating from the binary stripe pattern. Only the required first orders pass through and create the sinusoidal intensity pattern on the sample. A segmented polarizer (colorPOL VIS087 BC3 CW01, CODIXX) then generates azimuthal polarization, which is necessary to achieve maximum modulation depth of the sinusoidal pattern at the sample. The combination of the fast-switching DMD with the segmented polarizer implies only mechanically fixed and stable components with no moving parts. This circumvents the low time resolution in classical SIM configurations and furthermore guarantees an accurate determination of the phase shift by solely changing the displayed pattern on the DMD. The beams are relayed by two lenses (#49-367, Edmund Optics, AC254-300-A-ML, Thorlabs) and then reflected by two identical, but rotated dichroic beam splitters (ZT405/473/561rpc, AHF) to eliminate detrimental polarization effects for *s*- and *p*-polarized reflected light. The diffraction spots are projected close to the edge of the back focal plane of the objective (UAPON 100XOTIRF, Olympus), which is mounted onto a z-piezo stage (N-725.2A PIFOC, Physik Instrumente). The beams interfere at the focal plane at an effective NA of 1.44 and generate the

Optics EXPRESS

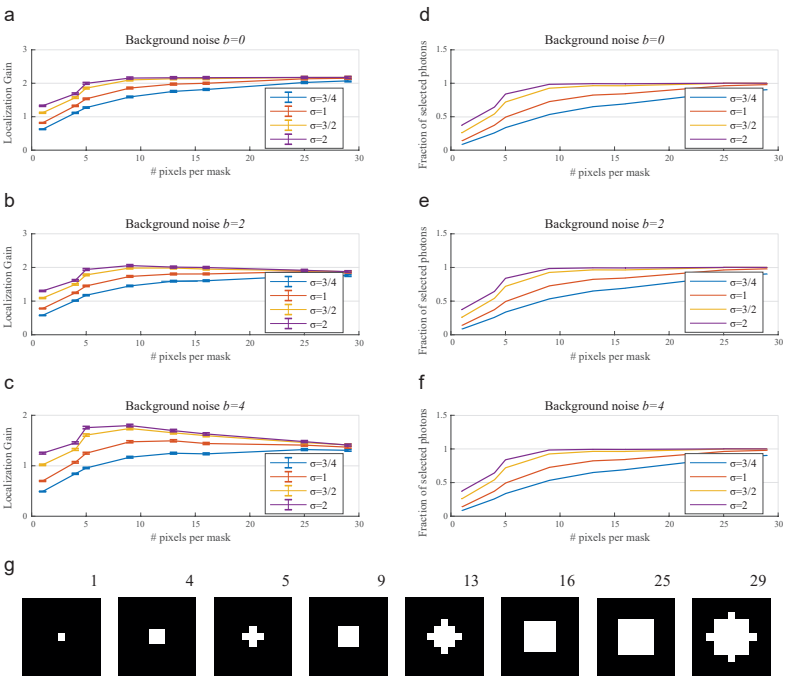

Fig. 4. Pixel selection and relation to PSF size for various background levels. (a-c) Change in the localization gain for various mask types, PSF to pixel size ratios (σ) and background noises. The mask size is increased from 4 to 29 pixels (g). By changing the mask size, a larger fraction of the emitters' signal will be accounted for (d-f), but more read-out noise is accumulated. (g) Corresponding series of figures chosen as the appropriate mask given the experimental parameters (noise, pixel size and PSF).

desired sinusoidal illumination pattern on the sample. Sample positioning can be performed by a piezo stage (P-545.3C8H, Physik Instrumente). The emitted fluorescence is collected by the same objective lens, passing through the dichroic mirror, the tube lens and a combination of emission filters (ZET405/473/561NF, AHF; FF01-503/LP-25, Semrock; HQ515/30m, Chroma) to reject unwanted excitation light and achieve lower residual background. A sCMOS camera (Zyla-4.2P-CL10, Andor) detects the fluorescence signals in the mode "rolling shutter global clear external triggering (non-overlap mode)". The size of the FOV on the sample is defined by a circular mask in the displayed DMD pattern and amounts to approximately 27 µm.

3.3. Pattern period calibration

For pattern period calibration a dense distribution of single Alexa Fluor488 molecules was repeatedly illuminated with phase shifted sinusoidal patterns. Data were analysed automatically by an adapted code of fairSIM [20] written in Java, extracting the shift vector length of the parameter estimation that corresponds to the pattern period of the excitation pattern. As shown in Fig. 5(b) we revealed a sinusoidal illumination pattern period of $\ell = (169.0 \pm 0.3)$ nm.

Optics EXPRESS

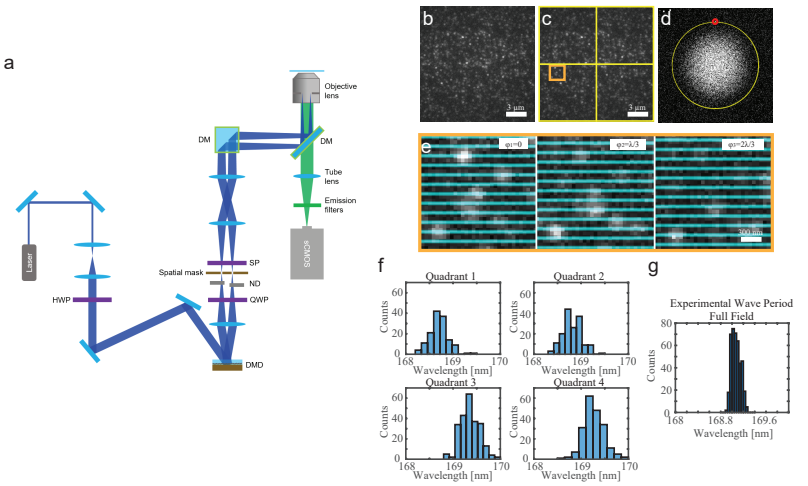

Fig. 5. Schematic of the SIMPLE setup and calibration. (a) Excitation laser 473 nm, 500 mW; 10× telescope for beam expansion; half wave plate (HWP); digital micro-mirror device (DMD) as spatial light modulator; quarter wave plate (QWP); neutral density (ND) filter; spatial mask for selection of diffraction orders; segmented "pizza" polarizer (SP) for polarization control; relay lenses; identical dichroic mirrors (DM) for azimuthal polarization conservation; NA 1.49 objective lens; sample on $x - y$ piezo stage; sCMOS camera with emission filters in the detection path. (b) Representative image sets of three phases used for period estimation, showing single Alexa Fluor488 molecules bound to functionalized glass. (c) Same image as in (b) with highlighted quadrants and enlarged region of interest (ROI). (d) Power-spectrum visualization of the cross-correlation in the Fourier domain returned by fairSIM. Red circle marks the maximum of correlation. FairSIM performs a fit with sub-pixel resolution and estimates the pattern period. (e) Illustration of the illumination pattern overlaid on an enlarged ROI (c) of recorded signals after each phase-shift representing the camera-based coordinate system and the sinusoidal wave-based coordinate system. (f, g) Period histograms for each quadrant and the full field of view. The precision of the spatial period ℓ in the whole FOV can be estimated to (169.1 ± 0.1) nm, and in the individual quadrants (Quadrant1: (168.7 ± 0.2) nm; Quadrant2: (168.8 ± 0.2) nm; Quadrant3: (169.4 ± 0.2) nm; Quadrant4: (169.3 ± 0.2) nm).

Optics EXPRESS

4. Results and discussion

As a proof of concept, we applied SIMPLE to the localization of single immobilized Alexa Fluor488 dyes. We recorded image sequences with $k = 3$ equidistant phases of the sinusoidal illumination pattern and subsequent localizations of the same molecule were used to obtain the localization precision Δx. Figure 6 shows a representative image series of one single Alexa488 dye.

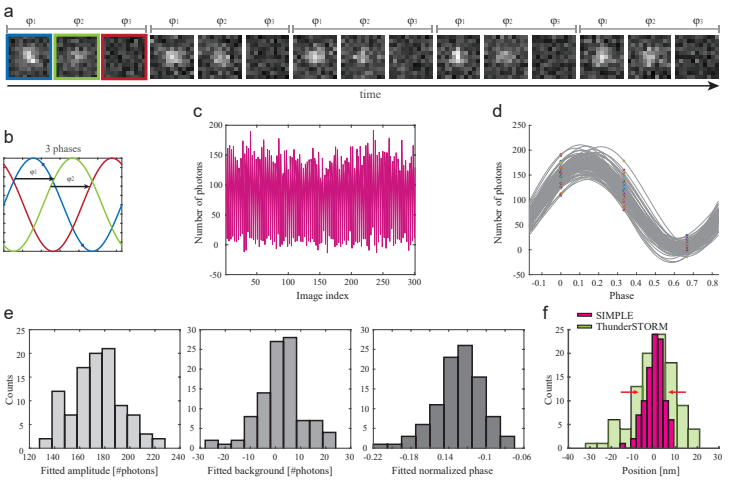

Fig. 6. Exemplary data and processing routine for SIMPLE. (a) Time series of a single Alexa Fluor488 molecule emitting upon repeated excitation (exposure time 50 ms) with three equidistant phases of a sinusoidal pattern. (b) Sketch of the phase steps $\Phi_i = 0, 1/3, 2/3$. (c) Intensity time trace of the emitter in (a) reflecting phase-dependent intensity modulation at 300 time points using a centered 3×3 mask for photon count calculation. (d) Extraction of the position for each intensity triple via a least-squares fitting routine reflecting the variability due to single emitter shot noise and background noise. We did not notice any sample drift during the acquisition time. (e) Statistics of the fitted positions in (d) for the amplitude (left), background (middle) and normalized phase (right). (f) Comparison of the localization precision for the same particle via multiple positioning using Thunderstorm [18] (green) and SIMPLE (pink) with a localization gain of 2.0-fold.

To validate the parallel detection of multiple single molecule emitters in a large field of view we placed single Alexa488 dyes on a glass slide and derived their positions via the SIMPLE method and standard SLML point localization. Sparse single molecule emitters were modulated with three phase shifted sinusoidal illumination patterns multiple times to reveal consecutive positions of all molecules in the FOV. This allows us to generate proper statistics for comparing localization precision enhancement of SIMPLE compared to SMLM in a parallel detection scheme. Figure 7 shows a reconstruction of a summed stack for three phases. The corresponding emission intensities to the three phases over the time series for two indicated emitters and the SIMPLE fitting routine are depicted in Fig. 7(b).

The obtained localization precision of SIMPLE in Fig. 7 outperforms conventional centroid fitting using ThunderSTORM [17] applied to the sum of three phase images being equivalent to homogeneous illumination. The achieved localization precision for a single molecule is $\Delta x = 4.3$ nm ($\Delta y = 4.5$ nm) for SIMPLE in contrast to $\Delta x = 8.8$ nm ($\Delta y = 10.9$ nm) for SMLM,

Optics EXPRESS

and $\langle x_{\text{all}} \rangle$ = 4.7 nm (SIMPLE) versus 9.4 nm (SMLM) for 40 particles averaged across the FOV (Fig. 7(c)). We further demonstrate the performance of our localization approach by precisely repositioning single emitters in (20.0 ± 0.4) nm steps on a piezo driven stage, for mapping particle localizations on the principle of a nanometric ruler (Fig. 8).

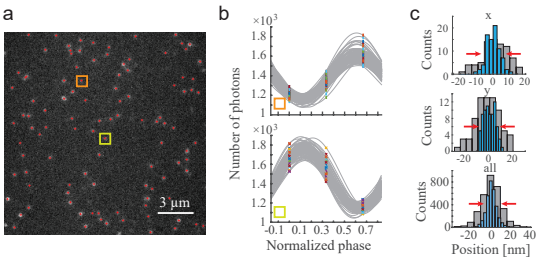

Fig. 7. Experimental validation of the SIMPLE method on a 15 µm FOV. (a) FOV showing the sample with sparse single Alexa Fluor488 dyes. (b) Exemplary fitting procedure on ~ 200 triple images for two isolated emitters in (b) (orange and yellow squares). (c) Histogram of x (upper panel) and y (middle panel) localizations of a single emitter are compared to SMLM centroid fitting using Thunderstorm with a localization gain of SIMPLE versus SMLM of 2.0-fold (x-direction) and 2.4-fold (y-direction). Histogram of x localizations of 40 single molecules in the FOV with an average gain of 2.1-fold (lower panel).

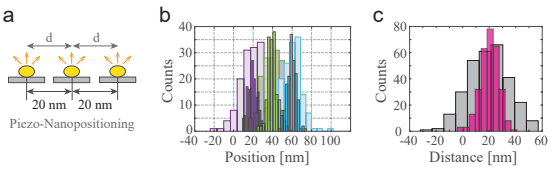

Fig. 8. Experimental validation of the SIMPLE method using piezo-stage driven 20 nm lateral movements (ground truth) of isolated Alexa Fluor488 emitters. (a) Sketch of piezo-nanopositioning of single molecule emitters. (b) Localization histogram of single emitters at three different positions for d = 20 nm distance and (c) Distance histogram of single emitters using SIMPLE (red) and Thunderstorm (grey) highlighting the power of the method.

In conclusion we have shown that sinusoidal wave patterns can be used as nanometric rulers for localizing the position of single molecule emitters with improved precision by a factor of 2 compared to standard SMLM methods. Similar to MINFLUX, particle localization is extracted from the photon count variation in an inhomogeneous illumination field. This enables to enhance localization precision with a minimal photon budget by the contribution of positional information in low illumination regions. Using a periodic wave function as an illumination pattern, we further demonstrate here that the concept of MINFLUX can massively parallelized from diffraction limited areas to a micron-sized field of view of >10 µm. Using a DMD as spatial light modulator we show that fast and exact nanometric phase shifting of sinusoidal illumination patterns can be employed to achieve a gain in localization precision of a factor of 2 compared to classical centroid fitting methods used in STORM/PALM and single particle tracking (SPT). A similar approach was recently presented in an article by Cnossen et al. [21] using piezo-mounted gratings to reveal enhanced localization precision, which was termed SIMFLUX. SIMPLE, MINFLUX and SIMFLUX are based on measuring photon number variations n_i in a shifted

Optics EXPRESS

periodic excitation pattern, thereby setting limits to single molecule movements during sample illumination and the excitation shifting period. Effects of motion blur and emitter movement during illumination are also well known in SPT experiments and affect the determination of diffusion modes or structural confinement sizes [22–24]. However, a reduction of photon numbers in SIMPLE, MINFLUX and SIMFLUX allows for improved temporal resolution and higher dynamic sampling rates at comparable localization precision to standard SMLM methods [13]. In the case of fixed samples, methods such as PALM/STORM [2, 3] and DNA-Paint [25] achieve nanometric structural resolution based on adjusting optimal sample labeling density, number of active emitters and obtaining a sufficient set of emitter localizations in consecutive images. For this purpose, specific labeling strategies and buffer systems were developed to set fluorophore switching rates and molecular binding kinetics for obtaining maximal structural resolution [26]. In SMLM imaging, frame rates are adjusted to gather the maximum photon signal during the ON-state of fluorophore blinking/binding that determines localization precision. In comparison, SIMPLE requires multiple image acquisitions (three images for each direction) for localizing a single emitter. This demands, for optimal imaging speed, to capture photon counts of the emitter during the ON-state before bleaching or blinking occurs. DMDs providing very high temporal control of illumination patterns, the limitation in image acquisition times is mainly due to the camera read-out speed, ensuring a high total detection rate of fluorescence spots (also referred to as "miss/hit probability" in the sample). Furthermore, SMLM requires four times the number of photons compared to SIMPLE to achieve a similar localization precision, therefore reducing the acquisition time of SIMPLE four-fold. Note that the emitter's density is a key factor that determines the false positive/negative rates of emitter localizations in SMLM methods [26] and accordingly provides an inherent quality criteria for SIMPLE to detect emitters within a diffraction-limited distance by changes in the modulated intensity response that can be extracted to avoid mis-localizations.

Altogether, SIMPLE improves localization precision at reduced photon numbers compared to standard SMLM approaches [27], the method will thus enable to minimize detrimental phototoxicity and photobleaching for live cell applications and single particle tracking that will be validated in future studies.

Funding

"la Caixa" Foundation (ID 100010434, LCF/BQ/IN18/11660032); Marie Skłodowska-Curie Horizon 2020 (713673, 754558, 642157); Spanish Ministry Centro de Excelencia Severo Ochoa (SEV-2015-0522); MINECO's Plan Nacional (BFU2017-86296-P); Generalitat de Catalunya (CERCA); Fundació Privada Cellex.

Acknowledgments

L.R. built the theoretical framework, developed simulation and data analysis tools, and contributed to the setup design and implementation; J.Z. implemented the setup, performed experiments and contributed to the initial study design; C.K. prepared samples and contributed to supplementary data analysis; F-C.W. provided data; T. H. advised on the manuscript and provided data; V.R and S.W. designed the study, performed simulations and data analysis, supervised the work and wrote the manuscript with the contribution of all authors.

References

1. L. Schermelleh, A. Ferrand, T. Huser, C. Eggeling, M. Sauer, O. Biehlmaier, and G. P. Drummen, "Super-resolution microscopy demystified," Nat. Cell Biol. **21**, 72–84 (2019).
2. M. J. Rust, M. Bates, and X. Zhuang, "Sub-diffraction-limit imaging by stochastic optical reconstruction microscopy (STORM)," Nat. Methods **3**, 793–795 (2006).

Optics EXPRESS

3. E. Betzig, G. H. Patterson, R. Sougrat, O. W. Lindwasser, S. Olenych, J. S. Bonifacino, M. W. Davidson, J. Lippincott-Schwartz, and H. F. Hess, "Imaging intracellular fluorescent proteins at nanometer resolution," Science **313**, 1642–1645 (2006).
4. R. E. Thompson, D. R. Larson, and W. W. Webb, "Precise nanometer localization analysis for individual fluorescent probes," Biophys. J. **82**, 2775–2783 (2002).
5. C. S. Smith, N. Joseph, B. Rieger, and K. A. Lidke, "Fast, single-molecule localization that achieves theoretically minimum uncertainty," Nat. Methods **7**, 373–375 (2010).
6. I. Izeddin, M. El Beheiry, J. Andilla, D. Ciepielewski, X. Darzacq, and M. Dahan, "PSF shaping using adaptive optics for three-dimensional single-molecule super-resolution imaging and tracking," Opt. Express **20**, 4957 (2012).
7. R. Fiolka, L. Shao, E. H. Rego, M. W. Davidson, and M. G. L. Gustafsson, "Time-lapse two-color 3D imaging of live cells with doubled resolution using structured illumination." Proc. Natl. Acad. Sci. United States Am. **109**, 5311–5 (2012).
8. D. Li, L. Shao, B.-C. Chen, X. Zhang, M. Zhang, B. Moses, D. E. Milkie, J. R. Beach, J. A. Hammer, M. Pasham, T. Kirchhausen, M. A. Baird, M. W. Davidson, P. Xu, and E. Betzig, "Extended-resolution structured illumination imaging of endocytic and cytoskeletal dynamics," Science **349**, aab3500–aab3500 (2015).
9. N. Chakrova, R. Heintzmann, B. Rieger, and S. Stallinga, "Studying different illumination patterns for resolution improvement in fluorescence microscopy," Opt. Express **23**, 31367 (2015).
10. R. Heintzmann and T. Huser, "Super-Resolution Structured Illumination Microscopy," Chem. Rev. **117**, 13890–13908 (2017).
11. M. G. Gustafsson, D. A. Agard, and J. W. Sedat, "I5M: 3D widefield light microscopy with better than 100 nm axial resolution," J. Microsc. **195**, 10–16 (1999).
12. F. Balzarotti, Y. Eilers, K. C. Gwosch, A. H. Gynnå, V. Westphal, F. D. Stefani, J. Elf, and S. W. Hell, "Nanometer resolution imaging and tracking of fluorescent molecules with minimal photon fluxes," Science **355**, 606–612 (2017).
13. Y. Eilers, H. Ta, K. C. Gwosch, F. Balzarotti, and S. W. Hell, "MINFLUX monitors rapid molecular jumps with superior spatiotemporal resolution," Proc. Natl. Acad. Sci. **115**, 6117–6122 (2018).
14. L.-H. Yeh, L. Tian, and L. Waller, "Structured illumination microscopy with unknown patterns and a statistical prior," Biomed. Opt. Express **8**, 695 (2017).
15. S. Wieser and G. J. Schütz, "Tracking single molecules in the live cell plasma membrane-Do's and Don't's," Methods **46**, 131–140 (2008).
16. R. J. Ober, S. Ram, and E. S. Ward, "Localization Accuracy in Single-Molecule Microscopy," Biophys. J. **86**, 1185–1200 (2004).
17. S. Ram, E. S. Ward, and R. J. Ober, "Beyond Rayleigh's criterion: A resolution measure with application to single-molecule microscopy," Proc. Natl. Acad. Sci. **103**, 4457–4462 (2006).
18. M. Ovesný, P. Křížek, J. Borkovec, Z. Švindrych, and G. M. Hagen, "ThunderSTORM: A comprehensive ImageJ plug-in for PALM and STORM data analysis and super-resolution imaging," Bioinformatics **30**, 2389–2390 (2014).
19. K. I. Mortensen, L. S. Churchman, J. A. Spudich, and H. Flyvbjerg, "Optimized localization analysis for single-molecule tracking and super-resolution microscopy," Nat. Methods **7**, 377–381 (2010).
20. M. Müller, V. Mönkemöller, S. Hennig, W. Hübner, and T. Huser, "Open-source image reconstruction of super-resolution structured illumination microscopy data in ImageJ," Nat. Commun. **7**, 10980 (2016).
21. J. Cnossen, T. Hinsdale, R. Thorsen, F. Schueder, R. Jungmann, C. S. Smith, B. Rieger, and S. Stallinga, "Localization microscopy at doubled precision with patterned illumination," bioRxiv p. 554337 (2019).
22. K. Ritchie, X. Y. Shan, J. Kondo, K. Iwasawa, T. Fujiwara, and A. Kusumi, "Detection of non-Brownian diffusion in the cell membrane in single molecule tracking," Biophys. J. **88**, 2266–2277 (2005).
23. S. Wieser, M. Moertelmaier, E. Fuertbauer, H. Stockinger, and G. J. Schütz, "(Un)confined diffusion of CD59 in the plasma membrane determined by high-resolution single molecule microscopy," Biophys. J. **92**, 3719–3728 (2007).
24. S. Wieser, M. Axmann, and G. J. Schütz, "Versatile analysis of single-molecule tracking data by comprehensive testing against Monte Carlo simulations," Biophys. J. **95**, 5988–6001 (2008).
25. R. Jungmann, M. S. Avendaño, J. B. Woehrstein, M. Dai, W. M. Shih, and P. Yin, "Multiplexed 3D cellular super-resolution imaging with DNA-PAINT and Exchange-PAINT," Nat. Methods **11**, 313–318 (2014).
26. S. Wolter, U. Endesfelder, S. van de Linde, M. Heilemann, and M. Sauer, "Measuring localization performance of super-resolution algorithms on very active samples," Opt. Express **19**, 7020 (2011).
27. D. Sage, T. A. Pham, H. Babcock, T. Lukes, T. Pengo, J. Chao, R. Velmurugan, A. Herbert, A. Agrawal, S. Colabrese, A. Wheeler, A. Archetti, B. Rieger, R. Ober, G. M. Hagen, J. B. Sibarita, J. Ries, R. Henriques, M. Unser, and S. Holden, "Super-resolution fight club: assessment of 2D and 3D single-molecule localization microscopy software," Nat. Methods **16**, 387–395 (2019).

185.225.208.100 {ts '2019-08-18 13:05:12'}

Appendix B

Modulation-enhanced localization microscopy

L. Reymond et al., "Modulation-enhanced localization microscopy", Journal of Physics: Photonics **2**, 041001 (2020)

Abstract Super-resolution fluorescence microscopy has become a powerful tool in cell biology to observe sub-cellular organization and molecular details below the diffraction limit of light. Super-resolution methods are generally classified into three main concepts: stimulated emission depletion (STED), single molecule localization microscopy (SMLM) and structured illumination microscopy (SIM). Here, we highlight the novel concept of modulation-enhanced localization microscopy (meLM) which we designate as the 4th super-resolution method. Recently, a series of modulation-enhanced localization microscopy methods have emerged, namely MINFLUX, SIMPLE, SIMFLUX, ModLoc and ROSE. Although meLM combines key ideas from STED, SIM and SMLM, the main concept of meLM relies on a different idea: isolated emitters are localized by measuring their modulated fluorescence intensities in a precisely shifted structured illumination pattern. To position meLM alongside state-of-the-art super-resolution methods we first highlight the basic principles of existing techniques and show which parts of these principles are utilized by the meLM method. We then present the overall novel super-resolution principle of meLM that can theoretically reach unlimited localization precision whenever illumination patterns are translated by an arbitrarily small distance.

Journal of Physics: Photonics

OPEN ACCESS

RECEIVED
4 May 2020

REVISED
6 June 2020

ACCEPTED FOR PUBLICATION
19 June 2020

PUBLISHED
23 July 2020

Original content from this work may be used under the terms of the Creative Commons Attribution 4.0 licence.

Any further distribution of this work must maintain attribution to the author(s) and the title of the work, journal citation and DOI.

PERSPECTIVE

Modulation-enhanced localization microscopy

Loïc Reymond[1,2], Thomas Huser[3], Verena Ruprecht[2,4] and Stefan Wieser[1]

[1] ICFO – Institut de Ciencies Fotoniques, The Barcelona Institute of Science and Technology, 08860 Castelldefels, Spain
[2] Centre for Genomic Regulation (CRG), The Barcelona Institute of Science and Technology, 08003 Barcelona, Spain
[3] Department of Physics, University of Bielefeld, 33615 Bielefeld, Germany
[4] Universitat Pompeu Fabra (UPF), Barcelona, Spain

E-mail: Stefan.wieser@icfo.eu

Keywords: super-resolution microscopy, modulation enhanced localization microscopy, minimal photon flux, localization precision, structured illumination localization microscopy

Abstract

Super-resolution fluorescence microscopy has become a powerful tool in cell biology to observe sub-cellular organization and molecular details below the diffraction limit of light. Super-resolution methods are generally classified into three main concepts: stimulated emission depletion (STED), single molecule localization microscopy (SMLM) and structured illumination microscopy (SIM). Here, we highlight the novel concept of modulation-enhanced localization microscopy (meLM) which we designate as the 4th super-resolution method. Recently, a series of modulation-enhanced localization microscopy methods have emerged, namely MINFLUX, SIMPLE, SIMFLUX, ModLoc and ROSE. Although meLM combines key ideas from STED, SIM and SMLM, the main concept of meLM relies on a different idea: isolated emitters are localized by measuring their modulated fluorescence intensities in a precisely shifted structured illumination pattern. To position meLM alongside state-of-the-art super-resolution methods we first highlight the basic principles of existing techniques and show which parts of these principles are utilized by the meLM method. We then present the overall novel super-resolution principle of meLM that can theoretically reach unlimited localization precision whenever illumination patterns are translated by an arbitrarily small distance.

1. Introduction

Cell biology and microscopy are closely intertwined since the invention of light microscopy in the late 1600s, attributed to Antonie van Leeuwenhoek who was the first to observe bacteria and protozoa. Fluorescence microscopy—pioneered in the early 1900s—is based on substances which absorb light that is reemitted as fluorescence at a longer wavelength determined by the Stokes shift [1, 2]. Nowadays, fluorescence microscopists in state-of-the-art biolabs can specifically tag and image molecular components of cells and tissues (such as proteins, lipids, DNA, RNA) in various biological systems with minimal invasiveness [2–4]. One of the key developments has been the advent of genetically encoded fluorescent proteins, which enabled to study protein localization, dynamics and function in cells [5, 6]. Over the last two decades, this approach generated fundamental knowledge about cellular processes and profoundly advanced life science research.

Despite the advantages of optical microscopy, both brightfield microscopes (using visible light passing through the sample) and fluorescence-based microscopes are fundamentally limited in spatial resolution by the wave nature of light. Specifically, the optical resolution is set by the diffraction limit of light to around $\lambda/2$, where λ is the wavelength of the collected light [7]. For example, considering the emission of a green fluorescent protein (GFP, $\lambda \sim 500$ nm), no structure below 250 nm would be resolvable.

Pioneering steps in the direction of super-resolution fluorescence microscopy were set in the late 1980's, with the recording of tracks of single light-scattering objects and fluorescent particles [8–10]. First described by Heisenberg around 1930, this approach used the fact that sparse point emitters can be detected with high precision: each recorded photon carries information about the true location of its—well separated—emitter [11, 12]. The precision of localization is then given by the spreading, called point spread function (PSF), of

© 2020 The Author(s). Published by IOP Publishing Ltd

the photons around the emitter position in the image plane. The PSF of the imaging system is characterized by a standard deviation s set by the numerical aperture (NA) and λ, the fluorescence emission wavelength, by $s \cong \lambda/\mathrm{NA}$. Collecting N photons is equivalent to repeating N independent measurement of the emitter's position, leading to an uncertainty given by the standard error of the mean [13] $dx = s/\sqrt{N}$. A precision of about 1 nm in the localization of a particle would therefore be achievable with around 10^4 photons detected, assuming a very low background noise.

In 1995, Eric Betzig published a first rough idea for how super-resolution optical microscopy based on the localization of single fluorescent molecules could be realized [12]. It did, however, take yet another 10 years, before he and colleagues were able to truly demonstrate this concept in 2006 by consecutively photo-activating and localizing single photo-activatable fluorescent proteins and by superimposing all detected single molecule locations to create one pointillistic image [14]. This was the starting point for single molecule localization microcopy (SMLM) methods such as (F)PALM, (d)STORM and μPAINT [15–18].

In a different attempt to overcome the diffraction limit of light, in the late 1990's Stefan Hell proposed stimulated emission depletion (STED) of fluorophores [19, 20]. In 2000, Klar *et al* showed a 5 to 6-fold increase in the axial resolution of a modified confocal microscope using depletion spots above and below the focused excitation spot. This depletion pattern was generated by placing a phased plate in the beam path of the depletion laser (called STED beam), resulting in a non-linear inhibition of active fluorescence to narrow the effective PSF of the microscope. Even though both the excitation and depletion laser spots are diffraction-limited, their combination results in a non-linear depletion of the fluorophore's emission, which reduces the effective PSF of the excitation volume. After its initial realization, the concept was immediately extended to multiple colors, 2D/3D versions, cell applications and was generalized to reversibly photo-switchable fluorescent labels (RESOLFT) [21–24].

Around the year 2000, another super-resolution microscopy (SRM) concept was introduced by Gustafsson and Heintzmann based on the use of interference patterns in structured illumination microscopy (SIM) [25, 26]. In contrast to PALM, where typically more than 10^4 raw-images are used to create a super-resolved image, SIM relies on 9 or 15 raw-images to create one super-resolved image. The physical principle of SIM is based on illuminating a sample with a striped pattern that will shift high-frequency image information below the diffraction limit into the lower frequency domain that can be captured by the objective lens [27, 28]. This is highlighted by the so-called Moiré patterns, which carry information about previously inaccessible details of the sample. The advantage of SIM is that super-resolved images are created without the need of special fluorophores since super-resolution linear SIM is not dependent on specific photo-physical dye characteristics, required in methods such as PALM, STORM or STED. The disadvantage of linear SIM is that it is limited to a resolution gain by a factor of two, down to approximately 100 nm. SIM has also been extended to non-linear SIM using photo-switchable dyes, which allows improving the image resolution, achieving about 50 nm lateral resolution [29–31].

In 2017, Balzarotti *et al* introduced MINFLUX—minimal photon fluxes—in which a radically new concept of SRM was presented with the potential to virtually reach unlimited resolution with minimal photo-damage to the fluorophore [32]. MINFLUX reached 2 nm localization precision by using less than $N = 500$ photons. Although the technical setup uses a doughnut-shaped laser beam, the method is drastically different from STED microscopy. In MINFLUX, single fluorescent emitters are kept close to the center of a doughnut-shaped illumination profile. The idea is to use the well-known doughnut shaped illumination profile as a ruler for probing the emitter's position. The position of the emitter is retrieved by a triangulation localization approach as outlined further below. MINFLUX can achieve better localization than the theoretical limit of SMLM methods and was extended to isotropic 3D localization precision [33, 34].

In 2019, the parallelization of the MINFLUX method was first described by Reymond *et al* using the acronym SIMPLE [35] and followed by similar approaches [36–38] named ROSE, SIMFLUX and ModLoc. In a recent paper [33], Hell *et al* also extended the field of view (FOV) of MINFLUX from initially around 100×100 nm^2 to a size of about 10×10 μm^2. In this perspective, we will describe the novel concept of these modulation-enhanced localization microscopies (meLM), its relation to STED, SMLM and SIM, and outline current technical realizations, limitations, and future perspectives of the approach.

2. Current concepts of super-resolution microscopy

In order to demonstrate how meLM is positioned within the field of super-resolution microscopy, we will split the current super-resolution (SR) methods into three main principles: stimulated emission depletion microscopy (STED), single molecule localization microscopy (SMLM) and structured illumination microscopy (SIM) [39–41]. To get an overview over the current SR methods and the novelty and relation of meLM to these three methods (STED, SMLM and SIM), we classify and structure all four approaches as shown in figure 1. Despite some shared features between meLM and the existing SR techniques (such as

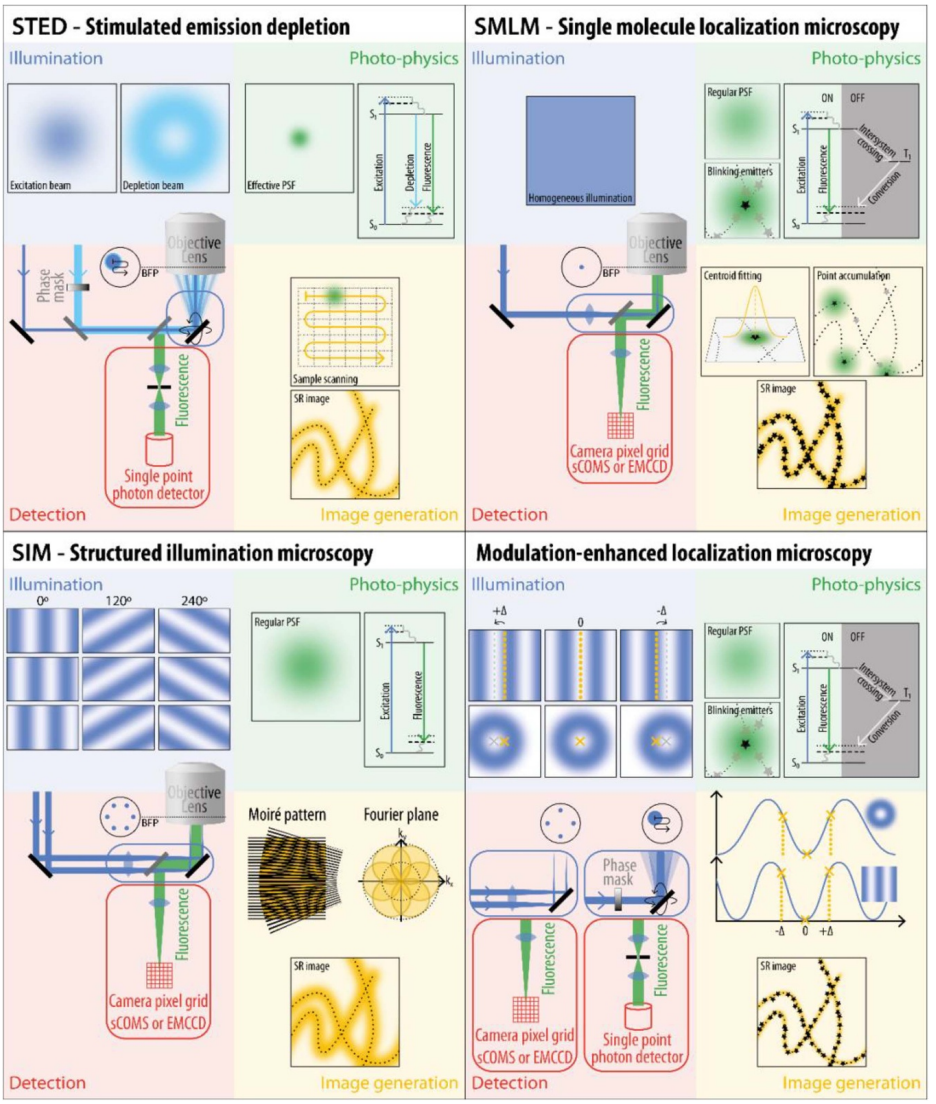

Figure 1. Overview of super-resolution microscopy concepts: STED—Stimulated emission depletion microscopy uses two illumination laser beams (STED-blue), one to excite fluorophores and one to deplete fluorescence in a doughnut shaped ring around the center of the excitation laser spot. The generated effective point spread function (STED-green) is scanned across the sample to create super-resolved images (STED-yellow). SMLM—Single Molecule Localization Microscopy is based on localizing single molecules with high precision (SMLM-yellow) by creating sparse active emitters in individual images. To generate sparsity, a very small subset of emitters is fluorescently activated (ON) at one single time point, whereas all the other fluorescent dyes are kept in an OFF state (SMLM-green). Point accumulation of thousands of isolated emitters into one image leads to a super-resolved image. SIM—Structured Illumination Microscopy is based on illuminating the sample with patterned light (SIM-blue, sinusoidal wave pattern) to generate the Moiré effect. Moiré patterns contain higher frequency information (SIM-yellow), which is algebraically decoded to allow for super-resolution microscopy. meLM—modulation-enhanced Localization Microscopy uses the illumination features of SIM or the doughnut spot in STED in the illumination path (meLM-blue). Instead of imaging the entire fluorescently labeled sample as done in SIM, meLM uses the idea of imaging single emitters as performed in SMLM by putting most of the fluorophores into an inactive state (meLM-green). By shifting the illumination pattern (meLM-blue) to modulate the fluorescence response (meLM-red), the single molecule position can be inferred from recorded photon counts with highest precision resulting in SR images at lowest photon budget (meLM-yellow).

structured illumination profile or on/off switching of the fluorophores to ensure sample's sparsity), meLM relies on a fundamentally different principle as described below, therefore justifying it to be named a fourth SR microscopy technique. In figure 1, all four SR methods are further split into four quadrants highlighting their specific requirements: (1) Illumination (blue), (2) photo-physics of the fluorophore (green), (3) setup and detection method (red) and (4) image generation, necessary to create the super-resolved image (yellow).

Control of illumination and photo-physical properties in each method enable spatial excitation and fluorescence emission control prior to signal detection by the objective lens (blue and green). Detection type and signal analysis in each method describes the handling of emitted photons after passing the objective lens (red and yellow). Note that machine-learning approaches can be combined with existing techniques such as SMLM [42, 43] and SIM [44, 45] for better and faster reconstructions, and we believe meLM will benefit from it too.

2.1. STED

To bypass the classical resolution-limit, STED uses a specific photo-physical concept, which is based on combining the excitation beam with a doughnut-shaped fluorescence depletion beam in the illumination path (see figure 1(a)). The non-linear dependence of the fluorescence depletion process on the power used for depleting fluorescence, together with the specific illumination configuration generate an effective point spread function (PSF) smaller than the diffraction-limited PSF, the size of which can be tuned with the power of the depletion beam. This sub-PSF-sized excitation volume is then scanned across the sample—identical to a confocal setup—and the corresponding fluorescence is collected with single point photodetectors, e.g. an avalanche photodiode. Scanning the sample with a sub-diffraction size PSF will result in super-resolved images [21].

2.2. SMLM

In contrast to STED, a homogenous illumination of the sample is used in SMLM (see figure 1(b)). To achieve a super-resolved image, technical efforts have been put in the development of excitation schemes that ensure sparsity of the fluorophores at each time point such as photo-activation or fluorescent dye switching. The detection is typically achieved with sensitive, high-speed cameras (sCMOS, EMCCD) to capture individual single molecules, frame by frame, with minimal read-out noise. Localization microscopy techniques such as PALM/STORM extract the molecular position of a single molecule by calculating the centroid position of the diffraction-limited signal spread across the pixelated frame of the camera. The reconstruction of structures of interest is then possible by superimposing the molecules' centroid coordinates obtained from a large number of processed images, each of them featuring localizations of a sparse sub-set of the tagged fluorescent molecule of interest. Even though the localization precision of each emitter is high (2–20 nm), the effective resolution of the SR image is typically around 20–50 nm not only depending on the single molecule localization precision but further on the density of collected single molecule positions, structural sample parameters and true positive localizations [46–49]. Altogether, SMLM achieves super-resolution by controlling the sparsity of fluorophores and using image post-processing algorithms for centroid fitting and pointillistic image reconstruction [50].

2.3. SIM

Structured illumination microscopy (SIM) creates high resolution via patterned illumination (see figure 1(c)). SIM can be used with standard fluorophores and does not require specific photo-physical operations, making it broadly accessible to a large range of genetically encoded and commercially available fluorescent tags. In a typical SIM setup, a sinusoidal patterned illumination is rotated 3 times and shifted 3 (5) times resulting in 9 (15) raw—diffraction limited—images for 2D (3D) SIM [51]. Each of the raw images contains high frequency information (higher than given by the optical diffraction limit of the microscope), visible as low frequency features of Moiré patterns. These raw images then have to be mathematically decoded resulting in a reconstructed super-resolved image [28, 52].

2.4. meLM

Modulation-enhanced localization microscopy (meLM see figure 1(d)) takes advantage of both the structured illumination (sine-wave pattern from SIM or doughnut-shaped pattern from STED) and the sparsity of emitters used in SMLM to improve localization precision. The well-defined illumination pattern and, more importantly, its precise displacement, lead to a predictable modulated response of the fluorescence intensity from which extra information can be harvested. Even though any high-contrast structured illumination would theoretically work, until now only sinusoidal patterns and doughnut profiles have been used. Note that in this application the doughnut-shaped illumination inherited from STED is used solely as an excitation source and not as a depletion beam.

3. Principle of modulation-enhanced localization microscopy (meLM)

The fundamental requirements of modulation-enhanced localization microscopy are the following:

a. *A well-characterized structured illumination pattern (e.g. sinusoidal wave or doughnut-shaped beam)*
b. *The possibility to shift this pattern with high accuracy (sub-nanometric precision achievable with spatial light modulators (SLMs) or electro-optical deflectors (EODs))*
c. *A sparse sampling of fluorescently labelled molecules*
d. *Single photon counting with high precision and sensitivity*

Even though not strictly necessary, one assumes, for simplicity, a linear response of the fluorophore to the excitation; this assumption is reasonable for most of the fluorophores and for laser powers below the saturation intensity for most standard fluorophores. In the case of a sinusoidal illumination pattern, a series of three measurements are performed along the direction of the pattern, each of them corresponding to a different translational position of the pattern [35]. The collected fluorescence intensity, response of the emitter to the excitation, directly depending on its relative position with respect to the illumination pattern, will therefore be modulated as the illumination is shifted. From this series of three images, one can extract three different numbers of emitted photons N_i, which follow the shape of the illumination profile (in the case of a non-linear response, one simply has to combine the response with the excitation pattern). It is important to assume a stable photo-physical behavior during the measurement time. From these modulated emission intensities N_i, one retrieves the position of the emitter through fitting of the illumination's shape; a sinusoidal function in this case. As *x*-*y* positions can be determined independently, using two orthogonal illumination patterns is sufficient for 2D localization of a single particle. The procedure is therefore repeated after a 90° rotation of the illumination pattern. MINFLUX works in a similar way, using a doughnut-shaped illumination and consecutive measurements at four positions to retrieve a *x*-*y* localization. This approach is radically different from SIM and SMLM as it relies neither on image reconstruction of Moiré patterns in Fourier space, nor on centroid fitting of diffraction-limited photon distributions.

The localization precision of meLM can be evaluated using error propagation and the Cramer–Rao Lower Bound (CRLB) as derived for sinusoidal, Gaussian and quadratic functions [32]. In the next section, we will describe the resulting localization precision by using either large or small pattern shifts, where we achieve a homogeneous ∼2-fold localization improvement or higher localization gains, respectively.

Altogether, the concept relies on phase-shifting of the otherwise stable illumination pattern which can be performed with nanometer precision (<1 nm) to probe the actual particle position through photon number variations for different phase shifts. The measured photon counts can be fitted to the known illumination pattern to derive the actual particle location leading to higher localization precisions compared to centroid fitting in classical SMLM.

The power of the newly developed meLM technique comes from the extra information one can extract from the structured nature of the previously well-characterized illumination pattern. In other words, by putting into the system more knowledge—in this case the illumination's spatial shape and spatial shifts—one can achieve higher localization precision. The requirement is that there is a technology to control illumination patterns and shifts at precisions significantly smaller than the wavelength of the emitted light. This, however, can be achieved easily e.g. by displacing the sample underneath a stationary pattern using high-precision piezo-position stages, or by displacing the pattern. MINFLUX, which opened the path for this class of techniques, directly exemplifies an extreme case, where the emitters are localized in the minimum of the doughnut-shaped illumination profile using sub-nanometer shifts. However, this is only possible at the expense of the size of the field of view, as only the particles resting at the center of the doughnut will be localized with higher precision (see below). In comparison, other techniques such as SIMPLE, ROSE, SIMFLUX and iterative MINFLUX have the advantage of providing a localization precision improvement over large fields of view and have been shown to yield an improvement factor of around two.

The key difference between meLM and other SR techniques is that information about the actual emitter's position can be extracted even in the complete absence of any detected photons in an image. Indeed, by considering a region of the FOV, where nothing but noise is visible on a camera frame, only two plausible conclusions can be drawn:

(1) There is no emitter at this location.
(2) The emitter is located in a trough with a zero value of the illumination intensity.

The latter hypothesis is then answered to with the next acquired image where the illumination is shifted: a brightness increase will be observed if there is an emitter present. This *Gedankenexperiment* shows that

after a full measurement cycle, i.e. successive phase shifts of the illumination, both the 'absence of' and the actual collected photons contributed to defining the position of the emitter. This contrasts with standard SMLM that would only employ the directly captured photon information.

In the following subsections, we will describe how this homogeneous two-fold increase in localization precision is achieved, as well as the more specific regimes where the gain becomes virtually infinite using small pattern shifts.

3.1. Homogeneous two-fold localization precision gain

Whenever (1) the average illumination intensity is equal, and (2) the 'modulation efficiency' (defined further below) is constant over the FOV, a homogeneous resolution gain over the whole FOV will be reached:

(1) Assuming a sinusoidal illumination described by:

$$I(x) = \frac{A}{2}\left(1 + m\cos\left(\frac{2\pi}{\lambda}(x - \phi_0)\right)\right)$$

with A the amplitude, ϕ_0 the phase and m the modulation depth. Taking $k \geq 2$ equally spaced sampling points on the illumination, i.e. $x_i = \frac{1}{k}\left(i - \frac{k+1}{2}\right), i = 1, \ldots, k$, one obtains an expression for the average total number of photons:R

$$N = \sum_{i=1}^{k} n_i = \sum_{i=1}^{k} R\left(I(x_i)\right).$$

R represents the response function of the fluorophore to a given excitation, generalizing the approach to any illumination pattern and linear/non-linear response of the fluorophore. In the following, this response is assumed to be linear, without loss of generality $R = 1$, leading to:

$$N = \sum_{i=1}^{k} \frac{A}{2}\left(1 + m\cos\left(\frac{2\pi}{\lambda}(x_i - \phi_0)\right)\right) = \frac{2A}{k}.$$

Please note that the resulting expression does *not* depend on ϕ_0, and is therefore constant over the FOV whenever$k \geq 2$.

(2) Next, we introduce a 'modulation efficiency'ε_m, defined as the normalized standard deviation of n_i the recorded number of photons:

$$\varepsilon_m = \frac{\mathrm{std}\left(\{n_i\}\right)}{N} = \begin{cases} \frac{m}{\sqrt{2}}\left|\sin\left(\frac{2\pi}{\lambda}\phi_0\right)\right|, & \text{if } k = 2 \\ \frac{m}{\sqrt{2k(k-1)}}, & \text{if } k > 2. \end{cases}$$

If the number of sampling points is below three, the modulation efficiency will exhibit a spatial dependence. For three or more frames per pattern orientation, a homogeneous modulation can be achieved, necessary for a homogeneous precision gain. Even though demonstrated for the specific case of a sinusoidal illumination pattern, this reasoning will hold for any arbitrary illumination pattern.

A two-fold localization precision gain over the field of view has been verified both *in silico* and experimentally by different groups [35–38]. The localization gain is defined by comparing the localization precision of meLM to SMLM for a given number of photons. Figure 2 shows one measurement to determine the position of a single emitter using the SIMPLE method. First, three intensities are recorded at three illumination pattern positions and second, a fit to the illumination pattern retrieves the actual single molecule position. Figure 3 shows the repetition of this process to get information about the statistical behavior of the three fit parameters: the amplitude, phase and offset. The photon spreading, shot-noise and read-out noise are included in these simulations showing a Poissonian-like distributed variability of photon counts [53] matching $\sqrt{N}$. We assume that the phase shift of the pattern is infinitely accurate, there is no movement or drift of the emitter and the laser has no intensity variation during the time scale of the measurement. The crucial parameter is the phase ϕ, as it corresponds to the position of the emitter on the sinusoidal wave pattern, i.e. its location. The spreading of the recovered phase σ_ϕ directly gives the localization precision. Figure 3(b) shows the comparison of the theoretical limit of SMLM as derived by Mortensen *et al* 2010 (revised formula from Thompson *et al* 2002) [13, 54]. The SIM based localization techniques, such as SIMPLE, provide a two-fold improvement in localization precision, homogeneously over the FOV and regardless of the number of recorded photons.

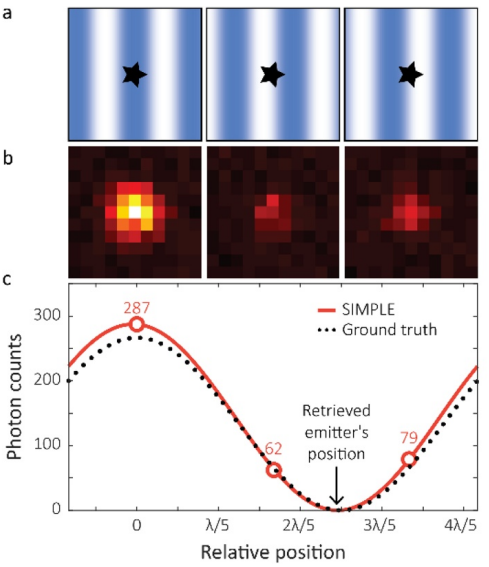

Figure 2. Principle of meLM. (a) A single emitter is illuminated with the same sinusoidal pattern sequentially shifted along the horizontal direction by a third of the wavelength (equidistant lateral displacements). (b) The modulated intensity response is then recorded on a camera. (c) The number of detected photons for each position of the illumination pattern is fitted with a function identical to the illumination profile, i.e. a sinusoidal wave function. The retrieved phase of the sine corresponds to the relative position of the emitter in the illumination pattern.

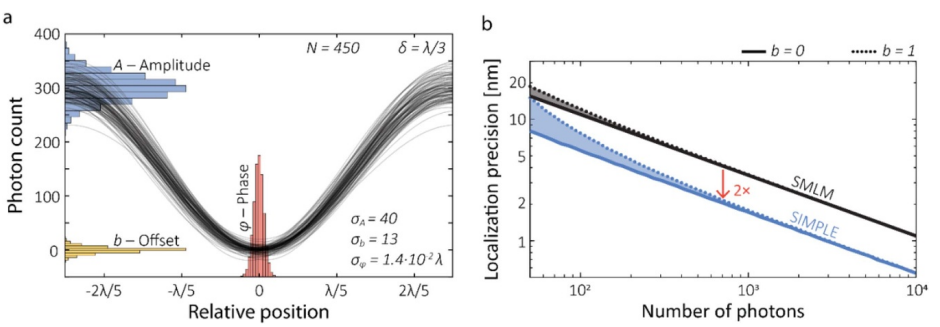

Figure 3. Localization precision of meLM compared to SMLM (a) Triplets of modulated intensities are repeatedly fitted with a sinusoidal function in order to retrieve the emitter's position. The histogram, normalized to the maximum, represents the dispersion of each parameter of the fit: the amplitude, the background offset and the phase. (b) Comparison between the theoretical limit of SMLM derived by Mortensen *et al* [54] and SIMPLE at various detected numbers of photons. SIMPLE reaches a 2-fold improvement of the localization precision, regardless of the number of detected photons. The parameter *b* is the standard deviation of the noise in photons/pixel.

3.2. Extreme localization precision gain: minimal photon flux

In the previous section, we described a shift of the excitation pattern by a third of the illumination pattern's wavelength, resulting in a high modulation of the emitter's fluorescence response following the full excitation amplitude. As previously mentioned, by reducing the displacement of the illumination pattern, one can reach even greater gain in localization precision: the fluorescent emitters present in the valley of the excitation will be precisely localized even in near-absence of photon emission. In such a case, the precision arises from the fact that an emitter can be kept in the zero-intensity region of the illumination pattern by shifting and registering its displacements with sub-nanometric precision.

Where SMLM uses the fluorescence signal to statistically retrieve the position of the centroid, for each photon collected, meLM extracts the information about the likelihood of an emitter to be present at a certain distance from the excitation's valley. In short, the paradigm changes from 'Where is the emitter in the FOV?'

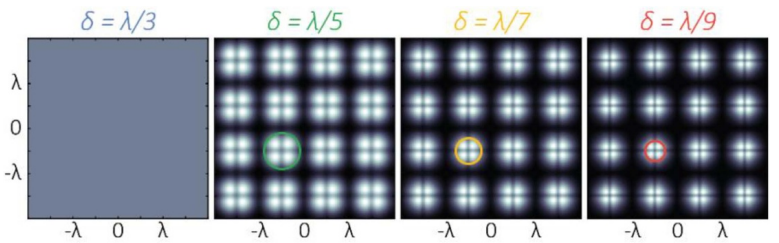

Figure 4. Spatial map of the 'modulation efficiency' ε_m for various step sizes of the illumination pattern's shift. For a pattern shift of a third of the illumination wavelength, ε_m is homogeneous whereas for smaller shifts, the modulation becomes dependent on the relative position of the emitter with respect to the illumination. The regions with high modulation efficiency, located at each trough of the pattern (highlighted by colored circles) scale with the size of the illumination shift.

to 'Is it located in the valley?'. By narrowing down the scope of the question, each individual answer (photon counted) gives rise to a more accurate information. This enhanced precision comes at the expanse of the covered surface, as this gain exists only within the dark regions of the illumination.

By adding a certain background noise level on top of the emitted fluorescence, the principle can still be applied, and a high localization precision can be envisioned. In addition, reduced modulation contrast due to limitations in real setup configurations can be accounted for with an increased background noise as described in Reymond *et al* [35].

Therefore, for smaller translations $x_i = \delta\ \left(i - \frac{k+1}{2}\right), i = 1, \ldots, k$, of the pattern with a shift amplitude δ, one can obtain the number of collected photons as a function of the relative position with respect to the illumination ϕ_0:

$$N = \frac{A}{2}\left(k + m\,\cos\left(\frac{2\pi}{\lambda}\,\phi_0\right)\,\csc\left(\frac{\pi}{\lambda}\delta\right)\,\sin\left(\frac{k\pi}{\lambda}\delta\right)\right).$$

For $k = 3$, the modulation efficiency can be analytically expressed as:

$$\varepsilon_m = \left|\sin\left(\frac{\pi}{\lambda}\delta\right)\right| m\sqrt{\frac{2}{3}}\,\frac{\sqrt{2+\cos\left(\frac{2\pi}{\lambda}\delta\right) - \left(1+2\cos\left(\frac{2\pi}{\lambda}\delta\right)\right)\cos\left(\frac{4\pi}{\lambda}\phi_0\right)}}{3+m\left(1+2\cos\left(\frac{2\pi}{\lambda}\delta\right)\right)\cos\left(\frac{2\pi}{\lambda}\phi_0\right)}.$$

As previously stated, a spatial dependence arises for $\delta \neq \frac{\lambda}{k}$. The effect of varying the pattern shift's size onto the modulation efficiency is shown in figure 4. If the modulation efficiency is negligible—the illumination intensity does not change between frames—meLM cannot provide extra information compared to SMLM.

Following the same principle as described in figure 3, the triplet of emitter intensities, recorded close to the illumination minimum, is fitted with the illumination profile to obtain the particle location. Comparing figure 3(a) with figure 5(a) highlights the resulting higher localization precision at the same number of photons ($N = 450$) set in this simulation (see specifically the standard deviation of the fitted phase σ_ϕ). Reducing the pattern shift will increase the localization precision gain regardless of the number of photons (see figure 5(b)).

When we consider emitters residing outside of the illumination minimum, the effect of having a gain in localization precision compared to SMLM will be lost. The farther the particle climbs up towards the peak of the illumination pattern, the less of an advantage is created by the smaller phase shift mode, eventually removing all information encoded in the phase. The observed localization precision gain with respect to the position of the emitter relative to the illumination pattern is shown in figure 6(a). Balzarotti *et al* showed that the localization precision scales with $L/\sqrt{N}$ when a single molecule emitter is scanned with pattern shifts of size L. However, as illustrated in figure 6(b), this comparison for a fixed number of detected photons implies a strong increase of the fluorescence whenever the fluorophore is located outside of the illumination minimum. Specifically, to keep the same number of photons, an increasing laser power is necessary, thereby creating a larger amplitude of the illumination pattern (see figure 6(b)). If on the other hand the emitter resides close to the peak of the illumination pattern, the localization precision will be low, and the high laser power will eventually bleach the fluorophore. To quantify this increased intensity required, we represent the achievable localization gain alongside the square root of the relative illumination amplitude (figure 6(c)).

3.3. Experimental results

In order to demonstrate experimentally the results obtained through computer simulations, a variety of samples have been tested by different research groups. We show in figure 7 a comparison of localization

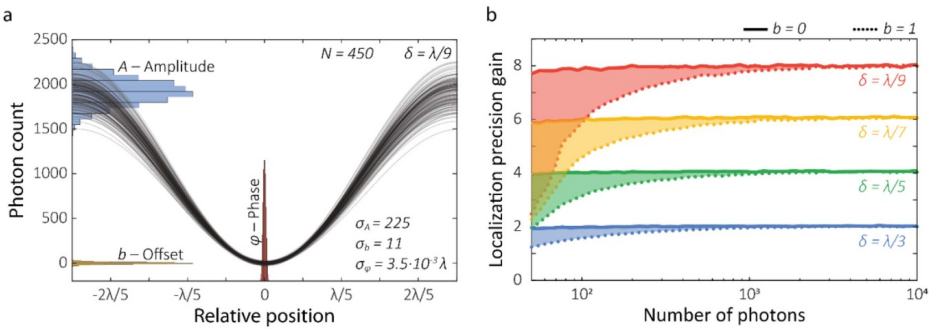

Figure 5. Smaller phase shifts increase the localization precision for molecules located in the valley of the illumination pattern: (a) Triplets of intensities collected in the illumination's valley are repeatedly fit, providing a high precision localization of the emitter. The illumination pattern is shifted by a ninth of its wavelength between each point centered on zero. The distribution of the fitted phase, at equivalent numbers of detected photons, is much narrower than for the case described in figure 3(a). (b) Localization gain compared to the theoretical limit of SMLM (Mortensen *et al*) obtained for different magnitude of pattern-shifts. The obtained gain at low background noise is nearly independent of the number of photons collected.

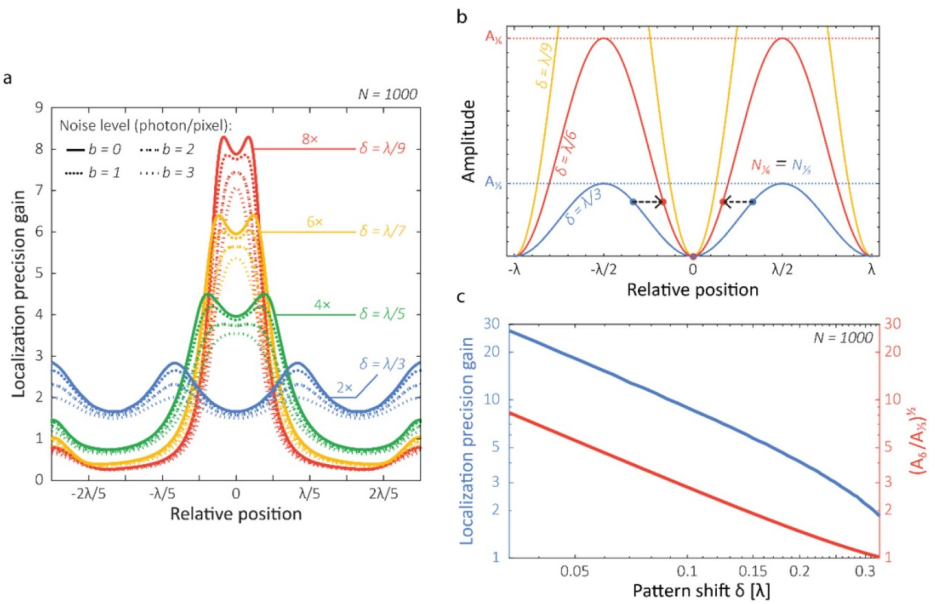

Figure 6. High-gain meLM. Extreme localization precision gains are created using small phase shifts of the illumination pattern (a) Localization precision gain as a function of the relative position of the emitter in the illumination pattern. The high gain of the 'valley mode' (red/yellow/green) only works close to the minimum of the illumination pattern. Phase shifts of a third of the wavelength (λ/3) result in approximately 2 to 3-fold improvement regardless of the position of the emitter (blue). (b) Illustration of the increase in amplitude necessary to keep the photon number constant while decreasing the size of phase shifts (λ/3, blue, λ/6, red and λ/9 yellow). The three blue points on the blue curve represent an overall number of $N_{1/3}$ photons used to determine the emitter's position. If we keep the number of photons constant ($N_{1/3} = N_{1/6}$) while creating a smaller phase shift (λ/6 instead of λ/3) we must follow a horizontal line indicated by the black arrow. This now has two important consequences: (1) the amplitude has to be increased and (2) the red points on the red curve are positioned deeper in the valley of the red curve. The two red points allow for a better estimation of the relative single molecule position compared to the blue ones. (c) Localization precision gain as a function of the pattern shift (blue), scaling linearly for small shifts. The increase in amplitude (emitter's response or illumination intensity) to preserve the number of photons while changing the size of the shift (red).

precision between classical SMLM techniques (ThunderSTORM [55]) and SIMPLE. This comparison is carried out on single Alexa488 dyes on glass, both in regular and high-gain regimes, validating a 2 and 6.5-fold improvement in localization precision (figures 7(b)–(d)). The illumination pattern and the fitting procedure effectively provide a doubling in localization precision over the whole field of view, whereas smaller pattern translation give rise to higher gain in regions restricted to the trough of the illumination,

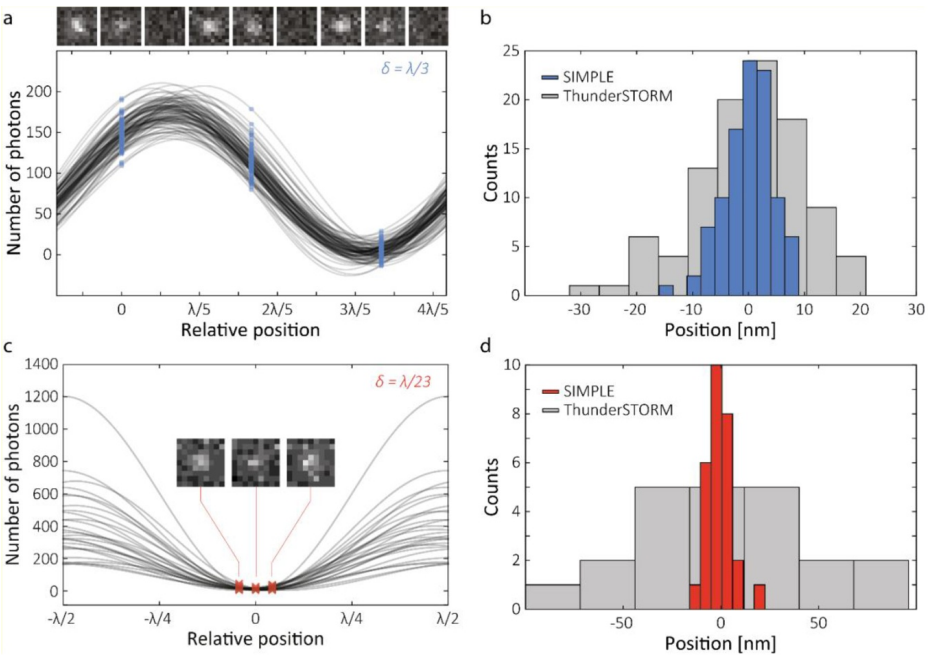

Figure 7. Illustration of the fitting procedure and obtained localization precision gain with respect to ThunderSTORM. (a) Exemplary data from a single Alexa488 dye with repeated fitting of recorded intensities. (b) Comparison of the localization position's distribution obtained using SIMPLE (blue) and ThunderSTORM (gray), featuring a 2-fold improvement in localization precision. (c) Example of high-gain regime, where reduced illumination shift results in higher localization precision. (d) Comparison of the localization precision obtained using SIMPLE (red) and ThunderSTORM (gray), with a 6.5-fold improvement. Note the difference of localization's counts, resulting from some discarded failed ThunderSTORM detections.

Table 1. Implementation's comparison of the existing meLM techniques.

	Pattern					
	Generation	Shifting	Shape	Lateral/axial	Detection path	Detector
MINFLUX	Vortex phase plate	EOD & galvos	Doughnut	x,y,z	'STED' Scan	APD
SIMPLE	Diffraction on DMD	DMD	Sine	x,y	Direct	sCMOS
ROSE	Beam splitters	EOM	Sine	x,y	Galvo (split)	sCMOS
SIMFLUX	Diffraction grating	Transl. grating	Sine	x,y	Direct	sCMOS
ModLoc	Beam splitters	EOM	Sine	z	Pockel cells	sCMOS

similarly to MINFLUX. The datasets are acquired on a modified custom-built TIRF-SIM setup with a high NA objective (NA 1.49).

4. Setup configurations

All the meLM techniques require the precise measurement of the induced intensity changes in the fluorescence as well as the generation and translation of a well-defined illumination pattern. A range of recently introduced meLM techniques each feature slightly different implementations achieving those goals, and are summarized thereafter.

4.1. Illumination

SIM-based meLM requires the interference of two pairs of identical laser beams, responsible for creating the sinusoidal illumination patterns, which can be achieved using standard diffraction gratings, spatial light modulators (SLMs), beam-splitters, Pockel-cells or digital micro-mirror devices (DMDs), see table 1.

The maximum achievable localization precision of the technique is limited by the modulation depth and the precision of the pattern shifts. Therefore, it is crucial to calibrate and to control the system precisely. In the case of MINFLUX, this is achieved with galvo-mirrors and electro-optic deflectors (EODs), respectively, for large scale and precise positioning of the doughnut beam profile.

The first MINFLUX approach was developed for a limited area of about 100 × 100 nm^2 but meanwhile it has been extended to FOVs of about 10 × 10 μm^2 using an iterative fluorophore targeting feedback loop. In brief, the iterative MINFLUX setup consists of a beam scanning confocal fluorescence microscope where the excitation beam is co-aligned with a UV beam to activate single emitters in a region of about 400 × 400 nm^2. Whenever a single fluorophore appears in the activated area, the doughnut-shaped illumination pattern shift is subsequently reduced from 150 nm to 40 nm while keeping the actual calculated position in the respective minimum. On this basis Gwosch *et al* [33] could show that they were able to detect ∼100 single emitters in about 1 min leading to an overall recording time for the FOV of >60 min. As a consequence of using iterative steps for locating the fluorophore of interest, more photons are needed, leading to a reduced localization precision compared to using a single minimum target search.

ModLoc, ROSE, and SIMFLUX use electro-optic modulators (EOMs) and the translation of a diffraction grating to modify the phase of one of the two interfering beams. In SIMPLE, the DMD is used both to switch between the perpendicular orientations of the pattern and to modify the relative phase between the interfering beams. The discrete nature of the array of mirrors constituting the DMD allows a theoretically error-free repeatability of the illumination pattern shift.

4.2. Detection

SIMPLE, ROSE, SIMFLUX, and ModLoc cover the entire *x-y* region of interest using a sCMOS camera. Complementarily, based on a STED-like excitation and detection scheme, MINFLUX uses an avalanche photodiode (APD) to detect the emission gathered from a scanned volume on the sample. APDs have the advantage to have very low noise-levels and to be extremely fast, enabling the extreme localization precision gains demonstrated with MINFLUX. Despite the limiting read-out time, the camera-based techniques benefit from the parallelization of the approach, which removes the need to scan the sample. SIMPLE and SIMFLUX both record the signal directly on a sCMOS camera, whereas ROSE takes advantage of the use of a resonant mirror, splitting the emitted fluorescence into six sub-regions spread over two cameras: this allows multiple repetitions of each measurements within a single read-out time. ModLoc is based on using a series of Pockel cells and splits the fluorescence into four quadrants in the emission path to allow for 'phase unwrapping' and high precision axial localization.

5. Discussion and conclusions

Currently, the original MINFLUX implementation of meLM still achieves the highest spatial resolution with minimal photobleaching. This implementation based on a doughnut-shaped excitation pattern readily enables a variety of modalities, such as nanoscale imaging and tracking of single fluorophores. The parallelization of the meLM scheme has the advantage of increasing the achievable spatial resolution relative to SMLM, which is the current 'gold standard' for super-resolution microscopy, based on its simplicity and low cost of components to realize it. With the 'simple' addition of a well-characterized illumination pattern and by acquiring a few more images relative to SMLM, the wide-field implementations of meLM—SIMPLE, ROSE, SIMFLUX, and ModLoc—provide enhanced precision over large FOVs, making these approaches very powerful. However, to enable the high-gain capabilities across the entire field of view, allowing virtually unlimited resolution, the use of photo-switchable probes is required.

For practical purposes, a combination of both an initial localization of molecules, by peak finding or SMLM, followed by a meLM procedure, will likely be necessary in order to utilize the full potential of this new class of techniques. By combining meLM with machine learning to allow high-throughput data analysis [42–45] one can anticipate further improvements in quality and applicability of meLM for future life-science research. This should then enable true wide-field imaging of a large number of structures with extensions of less than 10 nm, which will open up new perspectives in the characterization of local macromolecular interactions within single cells. This could be particularly powerful in our on-going quest of unraveling the nanoscale structure of interphase chromatin. Based on these exciting prospects, we believe that it is well deserved to call meLM, in its various implementations, the fourth super-resolution method.

Acknowledgments

L R acknowledges support of a fellowship from 'la Caixa' Foundation (ID 100010434, LCF/BQ/IN18/11660032) and funding from the European Union´s Horizon 2020 research and innovation programme under the Marie Skłodowska-Curie grant agreement No 713673. V R acknowledges support from the Spanish Ministry of Economy and Competitiveness through the Program 'Centro de Excelencia Severo Ochoa 2013-2017', the CERCA Programme/Generalitat de Catalunya, MINECO's Plan Nacional (BFU2017-86296-P) and support from the CRG Advanced Light Microscopy Facility. S W acknowledges

support from the Spanish Ministry of Economy and Competitiveness through the 'Severo Ochoa' program for Centres of Excellence in R&D (SEV-2015-0522), from Fundació Privada Cellex, and from Generalitat de Catalunya through the CERCA program.

ORCID iDs

Loïc Reymond https://orcid.org/0000-0002-9775-3353
Verena Ruprecht https://orcid.org/0000-0003-4088-8633
Stefan Wieser https://orcid.org/0000-0002-2670-2217

References

[1] Renz M 2013 Fluorescence microscopy-a historical and technical perspective *Cytometry Part A* **83** 767–79
[2] Lichtman J W and Conchello J A 2005 Fluorescence microscopy *Nat. Methods* **2** 910–9
[3] O'Hare H M, Johnsson K and Gautier A 2007 Chemical probes shed light on protein function *Curr. Opin. Struct. Biol.* **17** 488–94
[4] Lin M Z and Wang L 2008 Selective labeling of proteins with chemical probes in living cells *Physiology* **23** 131–41
[5] Tsien R Y 1998 The green fluorescent protein *Annu. Rev. Biochem.* **67** 509–44
[6] Shaner N C, Steinbach P A and Tsien R Y 2005 A guide to choosing fluorescent proteins *Nat. Methods* **2** 905–9
[7] Abbe E 1873 Beiträge zur Theorie des Mikroskops und der mikroskopischen Wahrnehmung *Arch. für Mikroskopische Anat.* **9** 413–8
[8] Hirschfeld T 1976 Optical microscopic observation of single small molecules *Appl. Opt.* **15** 2965
[9] Gross D and Webb W W 1986 Molecular counting of low-density lipoprotein particles as individuals and small clusters on cell surfaces *Biophys. J.* **49** 901–11
[10] Geerts H, De Brabander M, Nuydens R, Geuens S, Moeremans M, De Mey J and Hollenbeck P 1987 Nanovid tracking: a new automatic method for the study of mobility in living cells based on colloidal gold and video microscopy *Biophys. J.* **52** 775–82
[11] Bobroff N 1986 Position measurement with a resolution and noise-limited instrument *Rev. Sci. Instrum.* **57** 1152–7
[12] Betzig E 1995 Proposed method for molecular optical imaging *Opt. Lett.* **20** 237
[13] Thompson R E, Larson D R and Webb W W 2002 Precise nanometer localization analysis for individual fluorescent probes *Biophys. J.* **82** 2775–83
[14] Betzig E, Patterson G H, Sougrat R, Lindwasser O W, Olenych S, Bonifacino J S, Davidson M W, Lippincott-Schwartz J and Hess H F 2006 Imaging intracellular fluorescent proteins at nanometer resolution *Science* **313** 1642–5
[15] Van De Linde S, Kasper R, Heilemann M and Sauer M 2008 Photoswitching microscopy with standard fluorophores *Appl. Phys. B* **93** 725–31
[16] Hess S T, Girirajan T P K and Mason M D 2006 Ultra-high resolution imaging by fluorescence photoactivation localization microscopy *Biophys. J.* **91** 4258–72
[17] Rust M J, Bates M and Zhuang X 2006 Sub-diffraction-limit imaging by stochastic optical reconstruction microscopy (STORM) *Nat. Methods* **3** 793–5
[18] Sharonov A and Hochstrasser R M 2006 Wide-field subdiffraction imaging by accumulated binding of diffusing probes *Proc. Natl Acad. Sci. USA* **103** 18911–6
[19] Klar T A, Jakobs S, Dyba M, Egner A and Hell S W 2000 Fluorescence microscopy with diffraction resolution barrier broken by stimulated emission *Proc. Natl Acad. Sci.* **97** 8206–10
[20] Klar T A, Dyba M and Hell S W 2001 Stimulated emission depletion microscopy with an offset depleting beam *Appl. Phys. Lett.* **78** 393–5
[21] Sahl S J and Hell S W 2019 High-resolution 3D light microscopy with STED and RESOLFT *High Resolution Imaging in Microscopy and Ophthalmology* (Berlin: Springer) pp 3–32
[22] Willig K I, Kellner R R, Medda R, Hein B, Jakobs S and Hell S W 2006 Nanoscale resolution in GFP-based microscopy *Nat. Methods* **3** 721–3
[23] Donnert G *et al* 2007 Two-color far-field fluorescence nanoscopy *Biophys. J.* **92** L67–9
[24] Hell S W 2007 Far-field optical nanoscopy *Science* **316** 1153–8
[25] Heintzmann R and Cremer C G 1999 Laterally modulated excitation microscopy: improvement of resolution by using a diffraction grating *Optical Biopsies and Microscopic Techniques III* vol 3568 ed I J Bigio, H Schneckenburger, J Slavik, K Svanberg and P M Viallet (SPIE) pp 185–96
[26] Gustafsson M G L 2000 Surpassing the lateral resolution limit by a factor of two using structured illumination microscopy *J. Microsc.* **198** 82–87
[27] Jost A and Heintzmann R 2013 Superresolution multidimensional imaging with structured illumination microscopy *Annu. Rev. Mater. Res.* **43** 261–82
[28] Heintzmann R and Huser T 2017 Super-resolution structured illumination microscopy *Chem. Rev.* **117** 13890–908
[29] Gustafsson M G L 2005 Nonlinear structured-illumination microscopy: wide-field fluorescence imaging with theoretically unlimited resolution *Proc. Natl Acad. Sci. USA* **102** 13081–6
[30] Rego E H, Shao L, Macklin J J, Winoto L, Johansson G A, Kamps-Hughes N, Davidson M W and Gustafsson M G L 2012 Nonlinear structured-illumination microscopy with a photoswitchable protein reveals cellular structures at 50-nm resolution *Proc. Natl Acad. Sci.* **109** E135–E143
[31] Guo M *et al* 2018 Single-shot super-resolution total internal reflection fluorescence microscopy *Nat. Methods* **15** 425–8
[32] Balzarotti F, Eilers Y, Gwosch K C, Gynnå A H, Westphal V, Stefani F D, Elf J and Hell S W 2017 Nanometer resolution imaging and tracking of fluorescent molecules with minimal photon fluxes *Science* **355** 606–12
[33] Gwosch K C *et al* 2020 MINFLUX nanoscopy delivers 3D multicolor nanometer resolution in cells *Nat. Methods* **17** 217–24
[34] Eilers Y, Ta H, Gwosch K C, Balzarotti F and Hell S W 2018 MINFLUX monitors rapid molecular jumps with superior spatiotemporal resolution *Proc. Natl Acad. Sci. USA* **115** 201801672
[35] Reymond L, Ziegler J, Knapp C, Wang F-C, Huser T, Ruprecht V and Wieser S 2019 SIMPLE: structured illumination based point localization estimator with enhanced precision *Opt. Express* **27** 24578
[36] Gu L *et al* 2019 Molecular resolution imaging by repetitive optical selective exposure *Nat. Methods* **16** 1114–8

[37] Cnossen J, Hinsdale T, Thorsen R Ø, Siemons M, Schueder F, Jungmann R, Smith C S, Rieger B and Stallinga S 2020 Localization microscopy at doubled precision with patterned illumination *Nat. Methods* **17** 59–63
[38] Jouchet P *et al* 2019 Nanometric axial localization of single fluorescent molecules with modulated excitation *bioRxiv* **2019** 865865
[39] Requejo-Isidro J 2013 Fluorescence nanoscopy. Methods and applications *J. Chem. Biol.* **6** 97–120
[40] Godin A G, Lounis B and Cognet L 2014 Super-resolution microscopy approaches for live cell imaging *Biophys. J.* **107** 1777–84
[41] Cox S 2015 Super-resolution imaging in live cells *Dev. Biol.* **401** 175–81
[42] Nehme E, Weiss L E, Michaeli T and Shechtman Y 2018 Deep-STORM: super-resolution single-molecule microscopy by deep learning *Optica* **5** 458
[43] Ouyang W, Aristov A, Lelek M, Hao X and Zimmer C 2018 Deep learning massively accelerates super-resolution localization microscopy *Nat. Biotechnol.* **36** 460–8
[44] Laine R F, Goodfellow G, Young L J, Travers J, Carroll D, Dibben O, Bright H and Kaminski C F 2018 Structured illumination microscopy combined with machine learning enables the high throughput analysis and classification of virus structure *Elife* **2018** 7
[45] Christensen C N, Ward E N, Lio P and Kaminski C F 2020 ML-SIM: a deep neural network for reconstruction of structured illumination microscopy images
[46] Deschout H, Zanacchi F C, Mlodzianoski M, Diaspro A, Bewersdorf J, Hess S T and Braeckmans K 2014 Precisely and accurately localizing single emitters in fluorescence microscopy *Nat. Methods* **11** 253–66
[47] Wolter S, Endesfelder U, van de Linde S, Heilemann M and Sauer M 2011 Measuring localization performance of super-resolution algorithms on very active samples *Opt. Express* **19** 7020
[48] Nieuwenhuizen R P J, Lidke K A, Bates M, Puig D L, Grünwald D, Stallinga S and Rieger B 2013 Measuring image resolution in optical nanoscopy *Nat. Methods* **10** 557–62
[49] Descloux A, Grußmayer K S and Radenovic A 2019 Parameter-free image resolution estimation based on decorrelation analysis *Nat. Methods* **16** 918–24
[50] Schermelleh L, Ferrand A, Huser T, Eggeling C, Sauer M, Biehlmaier O and Drummen G P C 2019 Super-resolution microscopy demystified *Nat. Cell Biol.* **21** 72–84
[51] Ströhl F and Kaminski C F 2017 Speed limits of structured illumination microscopy *Opt. Lett.* **42** 2511
[52] Gregor I, Spiecker M, Petrovsky R, Großhans J, Ros R and Enderlein J 2017 Rapid nonlinear image scanning microscopy *Nat. Methods* **14** 1087–9
[53] Waters J C 2009 Accuracy and precision in quantitative fluorescence microscopy *J. Cell Biol.* **185** 1135–48
[54] Mortensen K I, Churchman L S, Spudich J A and Flyvbjerg H 2010 Optimized localization analysis for single-molecule tracking and super-resolution microscopy *Nat. Methods* **7** 377–81
[55] Ovesný M, Křížek P, Borkovec J, Švindrych Z and Hagen G M 2014 ThunderSTORM: a comprehensive ImageJ plug-in for PALM and STORM data analysis and super-resolution imaging *Bioinformatics* **30** 2389–90

Appendix C

Structured illumination microscopy

L. Reymond et al., *Structured illumination microscopy*, Vol. 1 (IOP Publishing, May 2021), p. I.3

Abstract Super-resolution imaging has emerged as a key future fluorescence imaging technology in life science research allowing one to resolve cellular details below 200 nm. Optical super-resolution (SR) microscopy such as STED and STORM typically uses high laser power, which compromises cell viability and long-term imaging and thus restricts these SR methods to fixed samples. On the other side, structured illumination microscopy (SIM) can be used for live cell super-resolution microscopy. STED is based on scanning the sample with an effective sub-diffraction laser spot while localisation microscopy (STORM, PALM) sequentially detects a subset of single emitters for generating a high-resolution image. In comparison, SIM uses stripe patterns for sample illumination to create large-scale Moiré effects, which are used to create super-resolved images. In a typical structured illumination microscope, the stripe-patterned illumination is rotated and shifted, resulting in a series of raw diffraction-limited images. Each of the raw images encodes high frequency information (higher than the optical limit of the microscope) which is visible as low frequency features of Moiré patterns. Algebraic decoding and reconstruction of the images results in a two-fold increase in lateral (2D SIM) and axial (3D SIM) resolution. Using high numerical aperture (NA) objective lenses, a lateral resolution of 80–100 nm can be achieved with 10^2–10^6 fold lower laser powers compared to STED and STORM imaging. Altogether, 2D/3D SIM allows for super-resolution imaging of fixed samples and on living cells at low illumination intensities using conventional fluorophores.

IOP Publishing

Imaging Modalities for Biological and Preclinical Research: A Compendium, Volume 1

Part I: *Ex vivo* biological imaging

Andreas Walter, Julia G Mannheim and Carmel J Caruana

Chapter I.3.b

Structured illumination microscopy

Loïc Reymond, Marcel Müller, Verena Ruprecht and Stefan Wieser

Super-resolution imaging has emerged as a key future fluorescence imaging technology in life science research allowing one to resolve cellular details below 200 nm. Optical super-resolution (SR) microscopy such as STED and STORM typically uses high laser power, which compromises cell viability and long-term imaging and thus restricts these SR methods to fixed samples. On the other side, structured illumination microscopy (SIM) can be used for live cell super-resolution microscopy. STED is based on scanning the sample with an effective sub-diffraction laser spot while localisation microscopy (STORM, PALM) sequentially detects a subset of single emitters for generating a high-resolution image. In comparison, SIM uses stripe patterns for sample illumination to create large-scale Moiré effects, which are used to create super-resolved images. In a typical structured illumination microscope, the stripe-patterned illumination is rotated and shifted, resulting in a series of raw diffraction-limited images. Each of the raw images encodes high frequency information (higher than the optical limit of the microscope) which is visible as low frequency features of Moiré patterns. Algebraic decoding and reconstruction of the images results in a two-fold increase in lateral (2D SIM) and axial (3D SIM) resolution. Using high numerical aperture (NA) objective lenses, a lateral resolution of 80–100 nm can be achieved with 10^2–10^6 fold lower laser powers compared to STED and STORM imaging. Altogether, 2D/3D SIM allows for super-resolution imaging of fixed samples and on living cells at low illumination intensities using conventional fluorophores.

1 Introduction

Optical super-resolution (SR) microscopy can be split into three main principles: Stimulated emission depletion microscopy (STED), localisation microscopy (LM) and structured illumination microscopy (SIM) [1]. Each of the three SR microscopy

doi:10.1088/978-0-7503-3059-6ch17

© IOP Publishing Ltd 2021

technologies has its own advantages and drawbacks. Although the lateral resolution of LM techniques such as STORM and PALM can come close to only a few nanometres (typically around 20 nm) in fixed biological samples—capturing single protein dimensions—the poor time resolution and phototoxic illumination conditions are the main limitations to observing molecular dynamics in living cells [2], especially when these dynamics are fast. In contrast to LM, where $>10^4$ raw-images are required to create a super-resolved image, SIM relies on typically 9 (2D) or 15 (3D) raw-images to create one super-resolved image. Current state-of-the-art high-speed, sensitive cameras (sCMOS, EMCCD) can continuously image at around 10 ms per frame, which allows for SIM imaging at ~1 frame/100 ms. Commercially available SIM systems indeed reach temporal resolutions of ~100 ms at around 100 nm spatial resolution, whereas custom-made SIM systems can reach temporal resolutions of ~10 ms with a spatial resolution of 80–100 nm [2]. In order to reveal features smaller than 50 nm, localisation microscopy techniques such as STORM and PALM would be the preferred SR, with the drawback of sample fixation and the need for specific fluorescent dyes.

Here we focus on classical structured illumination (SIM) as introduced by Gustafsson and Heintzmann [3–5] based on using sinusoidal illumination patterns. Besides classical SIM, a range of related microscopy methods, such as MSIM and iSIM, carry the 'SIM' abbreviation in their name. While they also use a form of structured light for illumination, they do not aim to achieve sinusoidal intensity distributions, and thus their resolution power and reconstruction approaches are different.

2 Principles and setups

2.1 Physical principles

SIM relies on creating sinusoidal wave patterns for illuminating the sample. Typically, 2 (3) beams of coherent laser light are focused onto the back focal plane of the objective lens for 2D (3D) SIM [5]. The interference at the front focal plane (the sample plane) of these 2 (3) beams results in a sinusoidal standing wave for 2D (3D) structured illumination with a wavelength below the diffraction limit. The physical principle of SIM imaging is based on the fact that illuminating a sample with a stripe pattern will shift high frequency information to lower frequencies, highlighted by the so-called Moiré patterns (see figure 1(b)), which carry information about previously inaccessible details of the sample [5]. In general, a lens or objective lens has an inherently limited frequency range that can pass through it. This leads to a loss of fine features—encoded in high frequency information—present in the sample. However, using sinusoidal patterns for illumination in order to make inaccessible frequency information available can theoretically improve the resolution by a factor of two (see figure 1(c)). To practically reach a two-fold gain in lateral and axial resolution, at least three rotations for each 3 (5) phase shifts of the sinusoidal illumination patterns are necessary for 2D (3D) SIM. The three rotations are needed to obtain an homogeneous lateral resolution gain, whereas the 3 (5)

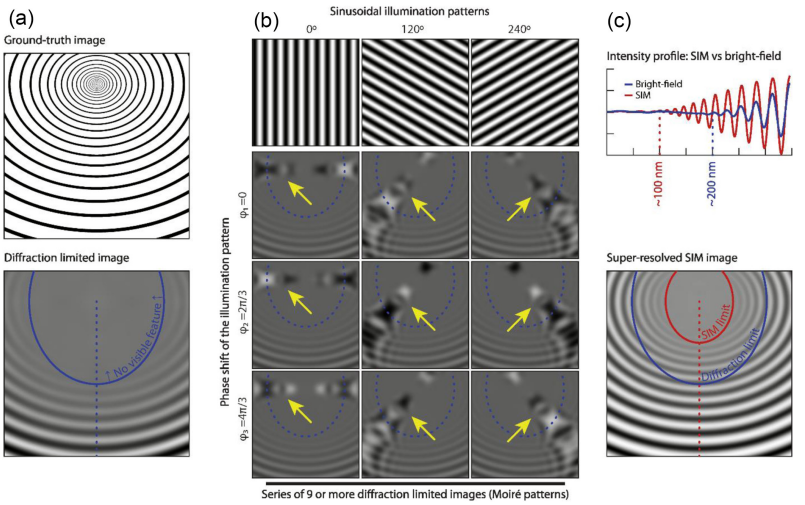

Figure 1. Physical principle of SIM. (a) Fine structures in an image are lost due to the diffraction limit of light. (b) Structured illumination of the sample (three rotations and three phase shifts) leads to Moiré effects (yellow arrows) which encode information about high frequency structures. (c) Algebraic decoding of the nine images from (b) are used to reconstruct one super-resolved image highlighted in the intensity line profile.

phase shifts are required to extract the super-resolution information from the Moiré patterns, also ensuring an even illumination on average.

2.2 Typical setups and state-of-the-art

Structured illumination microscopes are comprised of a wide-field detection path, often utilising a high-end research microscope, and a specialised illumination path that allows one to create, rotate and phase-shift the SIM interference pattern.

Commercial turn-key solutions are currently available by three manufacturers (Zeiss, Nikon, GE Healthcare), and are integrated into their respective microscope platforms. Due to their complexity, these systems are often maintained in core imaging facilities. Their specific feature sets such as excitation wavelength, filter sets, number of cameras, simultaneous channels and speed vary from setup to setup. However, most systems will offer the common 405 (DAPI), 488 nm (eGPF), 561/568 (mScarlet) and sometimes 633/642 nm (Cy5, Alexa 647) channels. All commercially available systems currently implement three-beam 3D SIM illumination, with some additionally offering a two-beam mode for TIRF-SIM imaging.

SIM instruments have also been developed by various research groups, which are well documented in scientific publications, and their blue-prints, parts lists as well as control and data reconstruction software are freely available. Typically, these systems are constructed with a specific imaging task at hand. For example, the popular fastSIM [6] concept uses a very fast spatial light modulator device to create the interference pattern, and complex camera synchronisation to achieve video-rate imaging speeds (exceeding 20 ms of reconstructed super-resolution data). Other

approaches perform SIM at cryogenic temperatures (cryoSIM) or combine it with adaptive optics to image challenging samples (deepSIM).

Figure 2 showcases both a typical commercial SIM installation and a custom-made SIM imaging system.

3 Biomedical relevance

3.1 Application range and relevance

SR fluorescence imaging methods fill the gap between confocal imaging and electron microscopy (EM) in terms of spatial resolution. In comparison, SIM provides specificity in molecular labelling and also offers a route towards live cell super-resolution microscopy, allowing one to observe dynamics and avoiding potential cellular structural changes introduced by fixation. SIM does not rely on specific fluorophores and it operates at very low illumination intensities, hence circumventing phototoxic effects and photobleaching of the sample. SIM imaging has been applied to resolve details of structural elements in cells [2], such as actin, microtubules, intermediate filaments (lamins) and the spectrin network in neurons. Recently, live cell SIM allowed for unravelling dynamic details of the endoplasmatic reticulum (ER), Golgi, the actomyosin cortex, nuclear territories and replication sites [2, 7–11].

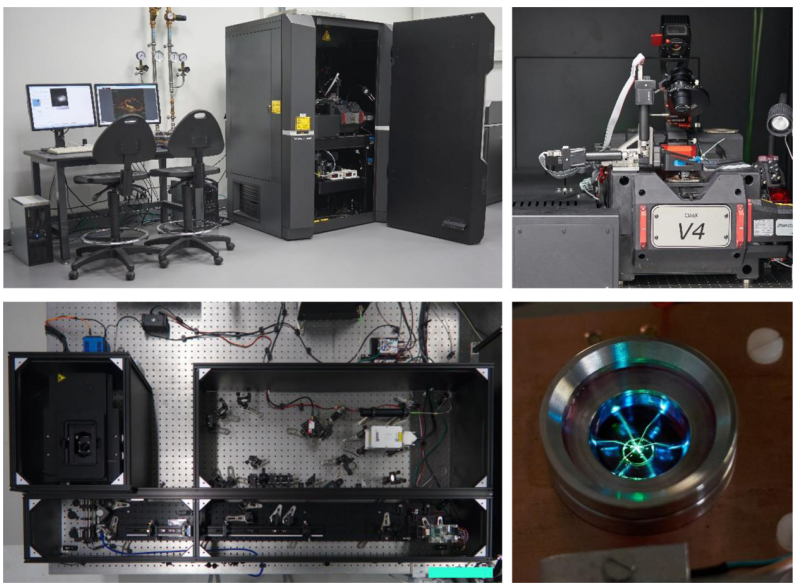

Figure 2. Typical setups for structured illumination microcscopy. A commercial DeltaVision OMX V4 3D-SIM in its enclosure (top left) and the microscope unit itself (top right), installed at University Bielefeld (photos courtesy W Hübner, University Bielefeld). A SIM microscope following the 'fastSIM' approach (bottom left), optimised for fast imaging speeds and rapid sample scanning (constructed at KU Leven by Robin Van den Eynde, scale bar: 25 cm). Laser beams interference creating a SIM illumination pattern in a fluorescent sample (bottom right).

3.2 Sample preparation

A key advantage of SIM is that it does not require specific labelling procedures or sensitive buffer conditions compared to STED and STORM/PALM. SIM can be applied to all genetically fused fluorescent proteins, Halo-tags or SNAP-tags and their membrane permeable dyes, fluorescently labelled antibodies, quantum dots or nanodiamonds. For both fixed and living cells, successful labelling strategies for wide-field or confocal microscopy often carry over to SIM with no or minimal changes. SIM has also been extended to non-linear SIM using photo-switchable dyes such as Dronpa, mEos or Kohinoor which allows improving the resolution reaching about 50 nm lateral resolution [2].

4 Parameters of image quality

Various parameters can be tuned to achieve high-quality SIM images [4]. Some are inherent to the microscope in use, and optimisations have to be performed by the instrument maintainer or manufacturer. Others are inherent to the sample and its imaging procedure, and thus are under the control of the user. A comprehensive protocol focusing on the optimisation of SIM imaging is available [4], featuring many real-world examples. A software package [7] is freely available to assist in assessing the quality of both raw and reconstructed SIM images, and to pinpoint problems that might arise both from malfunctioning instruments and, more commonly, challenging samples.

Three main aspects control the quality achievable in SIM data reconstruction: (1) The signal-to-noise ratio, i.e. the amount of desirable signal compared to both noise and background signal acquired. Here, very dim samples or samples featuring a high amount of out-of-focus fluorescence are problematic. (2) The modulation contrast of the SIM pattern, as a high contrast is needed to extract super-resolution information. Both misaligned instruments as well as scattering samples can heavily reduce pattern modulation contrast. (3) The quality of the SIM pattern, i.e. the ability of the instrument to create a homogenous sinusoidal intensity distribution over the field of view (FOV) and to reliably image it. Here, aberrations caused by refractive index changes in the sample, typically occurring when imaging through thicker materials like tissue, can easily both degrade pattern contrast and disturb the SIM pattern shape itself.

Figure 3 shows how the first two effects, signal-to-noise ratio and modulation contrast, will degrade a SIM image to the point where the desired resolution improvement is lost.

5 Data processing

SIM relies on a post-processing step, where the raw data, acquired with the set of rotated and phase-shifted structured illumination patterns, are reconstructed to extract additional information. Figure 4 provides an overview of how the raw images are transformed into frequency space (Fourier transform), separated, shifted, merged, filtered and finally transformed back into a super-resolved image [5].

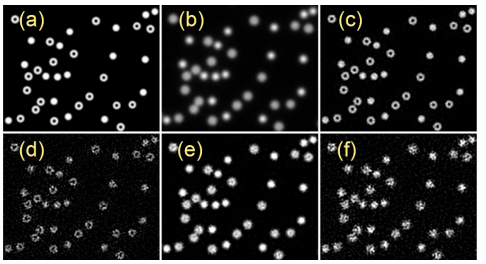

Figure 3. Degradation of SIM quality due to SNR and pattern contrast. (a) A layer of fluorescent spheres, which are either solid or hollow, is simulated. (b) The wide-field image cannot distinguish between hollow and solid spheres. (c) SIM imaging at reasonable modulation depth of ~80% and photon count of ~7000 per sphere clearly shows the resolution improvement. (d) Reduction in photon count by 10× to ~700 per sphere introduce typical SIM noise artefacts and uncertainty about the sphere shape. (e) A reduction in SIM pattern contrast to ~20% does not cause noise, but the super-resolution information is lost. (f) A combination of both effects heavily degrades signal quality.

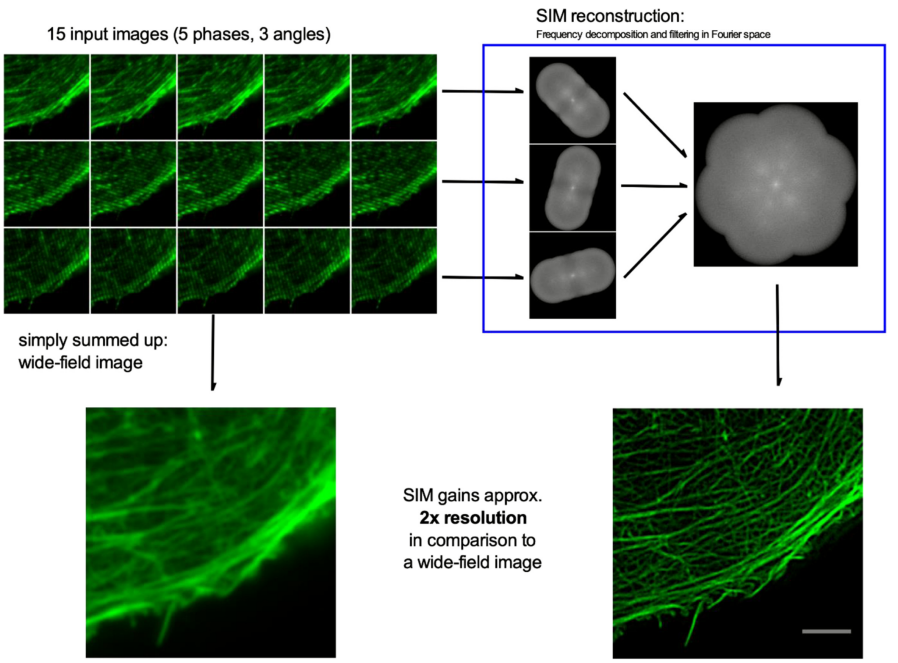

Figure 4. SIM image reconstruction process from a user perspective. The instrument collects a set of images, typically three rotations with 3 (5) phase-shifts for 2D (3D) SIM, which are transferred into Fourier space, separated, filtered and merged to form a super-resolved image. Different implementations of the reconstruction algorithm (blue box) exists, typically as commercial or open-source solutions provided by the scientific community.

The algorithm itself is also split into two parts, where first the SIM parameters (pattern spacing, rotation angles, phase shifts, modulation depths achieved) are extracted, and then are applied in the reconstruction step. This is necessary, as both

drifts in instrument alignment and sample-to-sample variations typically do not allow reconstruction of SIM data with only a fixed set of machine-dependent parameters. Additionally, the algorithm depends on machine-alignment data (optical transfer functions), that must be kept up-to-date by instrument maintainers, and offer filter-parameters to adjust for different sample behaviour (noise, background, etc). The latter can and often must be adjusted by the user. Unfortunately, different implementations of the reconstruction algorithm allow for different levels of control and follow different naming conventions.

Manufacturers of commercial SIM setups provide implementations of the reconstruction algorithm, available on the instrument's control computer or on a separate data processing workstation and are typically adapted to the instrument in use. Additionally, independent implementations, compatible with a wide range of SIM microscopes, are available. For example, the fairSIM project [10] aims to make SIM reconstruction algorithms available in the popular ImageJ/Fiji image processing software.

When reporting and publishing SIM data, it is important to document both the machine in use to acquire the data, the software (and version) used for reconstruction, as well as filter settings to ensure data integrity. Additionally, the raw data acquired by the instrument should be stored, and ideally made accessible as supplementary material. This both allows one to better assess data quality, and also to reprocess these data sets when new, improved algorithms become available. A comprehensive guide on publishing SIM data can be found in [4].

6 Conclusions

6.1 Strength and limitations

SIM allows surpassing the diffraction limit of light by providing a lateral resolution of around 100 nm. Importantly, LM reveals single molecule positions with accuracies of <20 nm, but the effective resolution due to the pointillistic image reconstruction is typically in the range of 50–70 nm [2]. In general, all SR methods are prone to imaging artefacts which in the case of SIM are mostly coming from deviations in the reconstruction parameters (i.e. sinusoidal wave length or rotation angles) compared to the correct parameters. Although SIM, in principle, easily allows the combination of high spatial and temporal resolution, most publications using SIM are still done on fixed samples. Altogether SIM has the potential to open super-resolution microscopy for live cell applications [2, 7–10].

6.2 Future developments

Recently, a series of similar new super-resolution methods have emerged, based on structured illumination of single fluorescent emitters, named MINFLUX [8], SIMPLE [9], SIMFLUX, ModLoc and ROSE. LM techniques such as STORM/PALM is primarily built on centroid fitting methods to derive particle localisations from the diffraction-limited photon distribution on a camera-based system. The lower limit of localisation precision for LM is given by $\Delta x = \sigma/\sqrt{N}$, with σ the standard deviation of the photon spreading defined by the system's point spread

function [1]. Radically new SR concepts, such as MINFLUX or SIMPLE, take advantage of using precisely controlled structured illumination patterns to measure the modulated fluorescence intensity of individual emitters in a shifted pattern of displacement L. Through the recording of the intensity-dependent fluorescence emission it was shown that single molecule localisation precision scales as $L/\sqrt{N}$. Figure 5 highlights the working principle using three equally spaced positions of the sinusoidal wave pattern, similar to a classical SIM pattern, leading to a two- to

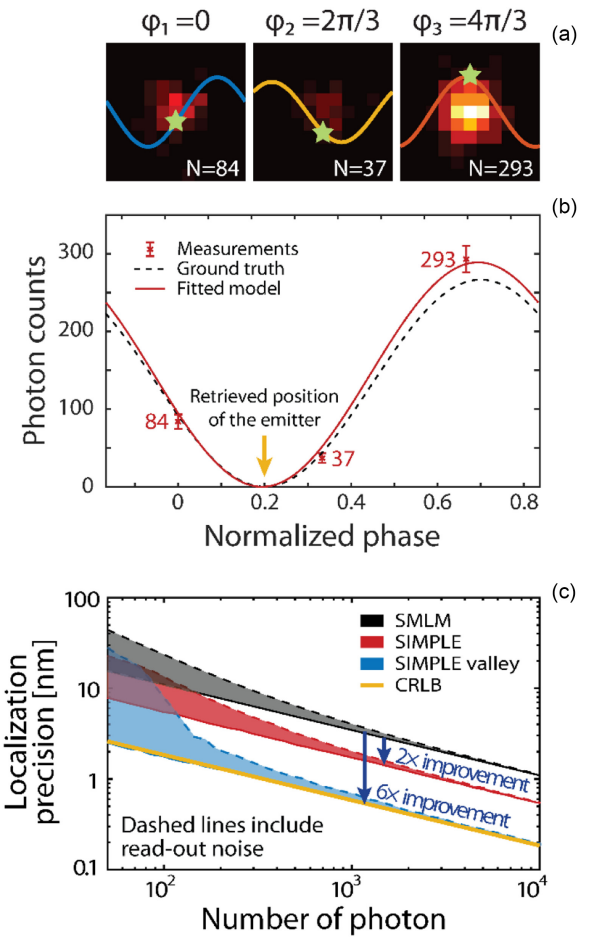

Figure 5. Principle of SIMPLE [9]. (a) The single emitters are illuminated with three phase-shifted sinusoidal patterns with equal phase shifts (lateral displacements). The modulated intensity response is then recorded on a camera. (b) The number of detected photons corresponding to each illumination is then fitted with a profile identical to the illumination, i.e. a sinusoid. The retrieved phase of the sine corresponds to the relative position of the emitter on the illumination pattern. (c) The comparison with existing SMLM techniques reveals a two-fold improvement for three equally spaced phase shifts. By reducing the phase shift, and for realistic experimental conditions, one can obtain a six-fold gain in accordance with the theoretical limits given by the Cramer–Rao lower bound (CRLB).

three-fold improvement of localisation precision compared to LM [9]. Since L can be set arbitrarily small, the localisation precision is theoretically unlimited, highlighting the potential of these novel SR methods.

References and further reading

[1] Schermelleh L *et al* 2019 *Nat. Cell Biol.* **21** 72–84
[2] Li D *et al* 2015 *Science* **349** 524–8
[3] Gustafsson M G L *et al* 2008 *Biophys. J.* **94** 4957–70
[4] Demmerle J *et al* 2017 *Nat. Protoc.* **12** 988–1010
[5] Heintzmann R and Huser T 2017 *Chem. Rev.* **117** 13890–908
[6] Lu-Walther H W, Kielhorn M, Förster R, Jost A, Wicker K and Heintzmann R 2015 *Methods Appl. Fluoresc.* **3** 014001
[7] Ball G, Demmerle J, Kaufmann R, Davis I, Dobbie I M and Schermelleh L 2015 *Sci. Rep.* **5** 15915
[8] Balzarotti F *et al* 2017 *Science* **355** 606–12
[9] Reymond L *et al* 2019 *Opt. Express* **27** 24578
[10] Müller M, Mönkemöller V, Hennig S, Hübner W and Huser T 2016 *Nat. Commun.* **7** 10980
[11] Guo Y *et al* 2018 *Cell* **175** 1430–1442.e17

Bibliography

Main publications

[16] L. Reymond, J. Ziegler, C. Knapp, F.-C. Wang, T. Huser, V. Ruprecht, and S. Wieser, "SIMPLE: Structured illumination based point localization estimator with enhanced precision", Optics Express **27**, 24578 (2019).

[17] L. Reymond, T. Huser, V. Ruprecht, and S. Wieser, "Modulation-enhanced localization microscopy", Journal of Physics: Photonics **2**, 041001 (2020).

[18] L. Reymond, M. Müller, V. Ruprecht, and S. Wieser, *Structured illumination microscopy*, Vol. 1 (IOP Publishing, May 2021), p. I.3.

Books

[1] H. Harris, *The birth of the cell* (Yale University Press, New Haven London, 2000).

[3] Müller, Johannes, *Archiv für Anatomie, Physiologie und Wissenschaftliche Medicin*, Vol. 1838 (Berlin, 1838).

[4] T. Schwann, *Mikroskopische Üntersuchungen über die Übereinstimmung in der Struktur und dem Wachstume der Tiere und Pflanzen* (Verlag der Sander'schen Buchhandlung (GE Reimer), 1839).

[8] J. B. Pawley, *Handbook Of Biological Confocal Microscopy* (Springer US, Boston, MA, 2006).

[19] B. R. Masters, *Superresolution Optical Microscopy: The Quest for Enhanced Resolution and Contrast*, Vol. 227, Springer Series in Optical Sciences (Springer International Publishing, Cham, 2020).

[22] E. Hecht, *Optics*, 5th edition (Pearson Education, Inc., Boston, 2017).

[26] G. R. Fowles, *Introduction to modern optics*, 2nd ed., Dover ed (Dover Publications, New York, 1989).

[46] I. Amidror, *The Theory of the Moiré Phenomenon: Volume I: Periodic Layers*, Vol. 38 (Springer London, London, 2009).

[83] P. J. Nahin, *The science of radio: with MATLAB and Electronics Workbench demonstrations*, 2nd ed (AIP Press, New York, 2001).

[84] N. I. Fisher, *Statistical Analysis of Circular Data*, First (Cambridge University Press, Oct. 1993).

[85] K. V. Mardia and P. E. Jupp, *Directional Statistics* (J. Wiley, Chichester, 2000).

[88] S. V. Gupta, *Measurement uncertainties: Physical parameters and calibration of instruments* (Springer Berlin Heidelberg, Berlin, Heidelberg, 2012).

[89] S. G. Rabinovich, *Measurement errors and uncertainties: Theory and practice* (Springer New York, New York, NY, 2005).

[90] M. Drosg, *Dealing with Uncertainties: A Guide to Error Analysis* (Springer Berlin Heidelberg, Berlin, Heidelberg, 2009).

[91] P. N. Kaloyerou, *Basic Concepts of Data and Error Analysis* (Springer International Publishing, 2018).

[93] H. Cramér, *Mathematical Methods of Statistics* (Princeton University Press, Dec. 1946).

[94] C. R. Rao, ed., *Linear Statistical Inference and its Applications*, Wiley Series in Probability and Statistics (John Wiley & Sons, Inc., Hoboken, NJ, USA, Apr. 1973).

[95] E. L. Lehmann and G. Casella, *Theory of point estimation*, 2nd ed, Springer Texts in Statistics (Springer, New York, 1998).

[96] M. Dekking, C. Kraaikamp, H. P. Lopuhaä, and L. E. Meester, *A modern introduction to probability and statistics: understandig why and how*, Springer Texts in Statistics (Springer-Verlag London Limited, London, 2010).

[98] Y. Pawitan, *In all likelihood: statistical modelling and inference using likelihood* (Oxford University Press, Oxford, 2013).

[100] J. Pfanzagl, *Mathematical Statistics* (Springer Berlin Heidelberg, Berlin, Heidelberg, 2017).

[121] U. J. Birk, *Super-resolution microscopy : a practical guide* (Wiley-VCH Verlag GmbH & Co. KGaA, Weinheim, Germany, Oct. 2017).

[126] A. Diaspro, ed., *Optical Fluorescence Microscopy* (Springer Berlin Heidelberg, Berlin, Heidelberg, 2011).

[129] J. Goodman, *Introduction to Fourier Optics*, Second (McGraw-Hill, Inc., 1968).

[131] H. Gross, *Handbook of optical systems, Vol. 1: Fundamentals of technical optics*, Vol. 1 (Wiley-VCH Verlag GmbH & Co. KGaA, Weinheim, Germany, Jan. 2005).

[132] P. W. Hawkes and J. C. H. Spence, eds., *Springer Handbook of Microscopy*, Springer Handbooks (Springer International Publishing, Cham, 2019).

[143] L. Novotny and B. Hecht, *Principles of nano-optics*, 2nd ed (Cambridge University Press, Cambridge, 2012).

[148] F. Träger, ed., *Springer Handbook of Lasers and Optics* (Springer Berlin Heidelberg, Berlin, Heidelberg, 2012).

[150] A. Walter, J. G. Mannheim, and C. J. Caruana, eds., *Imaging Modalities for Biological and Preclinical Research: A Compendium, Volume 1: Part I: Ex vivo biological imaging* (IOP Publishing, May 2021).

[151] William A. Shurcliff, *Polarized light* (Harvard Univ Press, Cambridge, 2013).

Articles

[2] P. Mazzarello, "A unifying concept: the history of cell theory", Nature Cell Biology **1**, E13–E15 (1999).

[5] E. Abbe, "Beiträge zur Theorie des Mikroskops und der mikroskopischen Wahrnehmung", Archiv für Mikroskopische Anatomie **9**, 413–468 (1873).

[6] M. Minsky, "Memoir on inventing the confocal scanning microscope: Memoir on Inventing the confocal scanning microscope", Scanning **10**, 128–138 (1988).

[7] M. Zimmer, "GFP: from jellyfish to the Nobel prize and beyond", Chemical Society Reviews **38**, 2823 (2009).

[9] D. Axelrod, "Cell-substrate contacts illuminated by total internal reflection fluorescence.", Journal of Cell Biology **89**, 141–145 (1981).

[10] S. W. Hell and J. Wichmann, "Breaking the diffraction resolution limit by stimulated emission: stimulated-emission-depletion fluorescence microscopy", Optics Letters **19**, 780 (1994).

[11] E. Betzig, "Proposed method for molecular optical imaging", Optics Letters **20**, 237 (1995).

[12] W. E. Moerner and M. Orrit, "Illuminating Single Molecules in Condensed Matter", Science **283**, 1670–1676 (1999).

[13] E. Betzig, G. H. Patterson, R. Sougrat, O. W. Lindwasser, S. Olenych, J. S. Bonifacino, M. W. Davidson, J. Lippincott-Schwartz, and H. F. Hess, "Imaging Intracellular Fluorescent Proteins at Nanometer Resolution", Science **313**, 1642–1645 (2006).

[14] R. M. Dickson, A. B. Cubitt, R. Y. Tsien, and W. E. Moerner, "On/off blinking and switching behaviour of single molecules of green fluorescent protein", Nature **388**, 355–358 (1997).

[15] M. G. L. Gustafsson, "Surpassing the lateral resolution limit by a factor of two using structured illumination microscopy", Journal of Microscopy **198**, 82–87 (2000).

[20] Rayleigh, "XV. *On the theory of optical images, with special reference to the microscope*", The London, Edinburgh, and Dublin Philosophical Magazine and Journal of Science **42**, 167–195 (1896).

[21] C. M. Sparrow, "On Spectroscopic Resolving Power", The Astrophysical Journal **44**, 76 (1916).

[23] A. Ghosh, N. Karedla, J. C. Thiele, I. Gregor, and J. Enderlein, "Fluorescence lifetime correlation spectroscopy: Basics and applications", Methods **140–141**, 32–39 (2018).

[24] L. Schermelleh, R. Heintzmann, and H. Leonhardt, "A guide to super-resolution fluorescence microscopy", Journal of Cell Biology **190**, 165–175 (2010).

[25] B. Mandracchia, X. Hua, C. Guo, J. Son, T. Urner, and S. Jia, "Fast and accurate sCMOS noise correction for fluorescence microscopy", Nature Communications **11**, 94 (2020).

[27] D. Axelrod, "Total Internal Reflection Fluorescence Microscopy in Cell Biology: Total Internal Reflection Fluorescence", Traffic **2**, 764–774 (2001).

[28] A. L. Mattheyses, S. M. Simon, and J. Z. Rappoport, "Imaging with total internal reflection fluorescence microscopy for the cell biologist", Journal of Cell Science **123**, 3621–3628 (2010).

[29] M. Martin-Fernandez, C. Tynan, and S. Webb, "A 'pocket guide' to total internal reflection fluorescence", Journal of Microscopy **252**, 16–22 (2013).

[30] R. Fiolka, Y. Belyaev, H. Ewers, and A. Stemmer, "Even illumination in total internal reflection fluorescence microscopy using laser light", Microscopy Research and Technique **71**, 45–50 (2008).

[31] R. Fiolka, "Clearer view for TIRF and oblique illumination microscopy", Optics Express **24**, 29556 (2016).

[32]W. Zong, X. Huang, C. Zhang, T. Yuan, L.-l. Zhu, M. Fan, and L. Chen, "Shadowless-illuminated variable-angle TIRF (siva-TIRF) microscopy for the observation of spatial-temporal dynamics in live cells", Biomedical Optics Express **5**, 1530 (2014).

[33]J. Boulanger, C. Gueudry, D. Münch, B. Cinquin, P. Paul-Gilloteaux, S. Bardin, C. Guérin, F. Senger, L. Blanchoin, and J. Salamero, "Fast high-resolution 3D total internal reflection fluorescence microscopy by incidence angle scanning and azimuthal averaging", Proceedings of the National Academy of Sciences **111**, 17164–17169 (2014).

[34]T. A. Klar and S. W. Hell, "Subdiffraction resolution in far-field fluorescence microscopy", Optics Letters **24**, 954–956 (1999).

[35]K. I. Willig, B. Harke, R. Medda, and S. W. Hell, "STED microscopy with continuous wave beams", Nature Methods **4**, 915–918 (2007).

[36]B. Hein, K. I. Willig, and S. W. Hell, "Stimulated emission depletion (STED) nanoscopy of a fluorescent protein-labeled organelle inside a living cell", Proceedings of the National Academy of Sciences **105**, 14271–14276 (2008).

[37]E. Rittweger, K. Y. Han, S. E. Irvine, C. Eggeling, and S. W. Hell, "STED microscopy reveals crystal colour centres with nanometric resolution", Nature Photonics **3**, 144–147 (2009).

[38]T. Müller, C. Schumann, and A. Kraegeloh, "STED Microscopy and its Applications: New Insights into Cellular Processes on the Nanoscale", ChemPhysChem **13**, 1986–2000 (2012).

[39]C. Eggeling, K. I. Willig, and F. J. Barrantes, "STED microscopy of living cells - new frontiers in membrane and neurobiology", Journal of Neurochemistry **126**, 203–212 (2013).

[40]H. Blom and H. Brismar, "STED microscopy: increased resolution for medical research?", Journal of Internal Medicine **276**, 560–578 (2014).

[41]S. W. Hell, "Toward fluorescence nanoscopy", Nature Biotechnology **21**, 1347–1355 (2003).

[42] D. M. Owen and K. Gaus, "Imaging lipid domains in cell membranes: the advent of super-resolution fluorescence microscopy", Frontiers in Plant Science **4**, 10.3389/fpls.2013.00503 (2013).

[43] E. Wegel, A. Göhler, B. C. Lagerholm, A. Wainman, S. Uphoff, R. Kaufmann, and I. M. Dobbie, "Imaging cellular structures in super-resolution with SIM, STED and Localisation Microscopy: A practical comparison", Scientific Reports **6**, 27290 (2016).

[44] L. Schermelleh, A. Ferrand, T. Huser, C. Eggeling, M. Sauer, O. Biehlmaier, and G. P. Drummen, "Super-resolution microscopy demystified", Nature Cell Biology **21**, 72–84 (2019).

[45] B. Huang, M. Bates, and X. Zhuang, "Super-Resolution Fluorescence Microscopy", Annual Review of Biochemistry **78**, 993–1016 (2009).

[47] R. Heintzmann and C. G. Cremer, "Laterally modulated excitation microscopy: improvement of resolution by using a diffraction grating", in BiOS Europe '98, edited by I. J. Bigio, H. Schneckenburger, J. Slavik, K. Svanberg, and P. M. Viallet (Jan. 1999), pp. 185–196.

[48] L. J. Young, F. Ströhl, and C. F. Kaminski, "A Guide to Structured Illumination TIRF Microscopy at High Speed with Multiple Colors", Journal of Visualized Experiments, e53988–e53988 (2016).

[49] M. Guo, P. Chandris, J. P. Giannini, A. J. Trexler, R. Fischer, J. Chen, H. D. Vishwasrao, I. Rey-Suarez, Y. Wu, X. Wu, C. M. Waterman, G. H. Patterson, A. Upadhyaya, J. W. Taraska, and H. Shroff, "Single-shot super-resolution total internal reflection fluorescence microscopy", Nature Methods **15**, 425–428 (2018).

[50] J. Roth, J. Mehl, and A. Rohrbach, "Fast TIRF-SIM imaging of dynamic, low-fluorescent biological samples", Biomedical Optics Express **11**, 4008 (2020).

[51] M. Lachetta, G. Wiebusch, W. Hübner, J. Schulte Am Esch, T. Huser, and M. Müller, "Dual color DMD-SIM by temperature-controlled laser wavelength matching", Optics Express **29**, 39696 (2021).

[52] M. G. Gustafsson, "Nonlinear structured-illumination microscopy: Wide-field fluorescence imaging with theoretically unlimited resolution", Proceedings of the National Academy of Sciences of the United States of America **102**, 13081–13086 (2005).

[53] M. G. L. Gustafsson, L. Shao, P. M. Carlton, C. J. R. Wang, I. N. Golubovskaya, W. Z. Cande, D. A. Agard, and J. W. Sedat, "Three-dimensional resolution doubling in wide-field fluorescence microscopy by structured illumination", Biophysical Journal **94**, 4957–4970 (2008).

[54] A. Jost and R. Heintzmann, "Superresolution Multidimensional Imaging with Structured Illumination Microscopy", Annual Review of Materials Research **43**, 261–282 (2013).

[55] J. Demmerle, C. Innocent, A. J. North, G. Ball, M. Müller, E. Miron, A. Matsuda, I. M. Dobbie, Y. Markaki, and L. Schermelleh, "Strategic and practical guidelines for successful structured illumination microscopy", Nature Protocols **12**, 988–1010 (2017).

[56] R. Heintzmann and T. Huser, "Super-Resolution Structured Illumination Microscopy", Chemical Reviews **117**, 13890–13908 (2017).

[57] R. Fiolka, L. Shao, E. H. Rego, M. W. Davidson, and M. G. L. Gustafsson, "Time-lapse two-color 3D imaging of live cells with doubled resolution using structured illumination", Proceedings of the National Academy of Sciences **109**, 5311–5315 (2012).

[58] D. Li, L. Shao, B.-C. Chen, X. Zhang, M. Zhang, B. Moses, D. E. Milkie, J. R. Beach, J. A. Hammer, M. Pasham, T. Kirchhausen, M. A. Baird, M. W. Davidson, P. Xu, and E. Betzig, "Extended-resolution structured illumination imaging of endocytic and cytoskeletal dynamics", Science **349**, aab3500 (2015).

[59] L. He, R. Kooistra, R. Das, E. Oudejans, E. Van Leen, J. Ziegler, S. Portegies, B. De Haan, A. Van Regteren Altena, R. Stucchi, A. M. Altelaar, S. Wieser, M. Krieg, C. C. Hoogenraad, and M. Harterink, "Cortical anchoring of the microtubule cytoskeleton is essential for neuron polarity", eLife **9**, e55111 (2020).

[60] E. Ingerman, R. London, R. Heintzmann, and M. Gustafsson, "Signal, noise and resolution in linear and nonlinear structured-illumination microscopy", Journal of Microscopy **273**, 3–25 (2019).

[61] G. Ball, J. Demmerle, R. Kaufmann, I. Davis, I. M. Dobbie, and L. Schermelleh, "SIMcheck: A toolbox for successful super-resolution structured illumination microscopy", Scientific Reports **5**, 15915 (2015).

[62] H. W. Lu-Walther, M. Kielhorn, R. Förster, A. Jost, K. Wicker, and R. Heintzmann, "FastSIM: A practical implementation of fast structured illumination microscopy", Methods and Applications in Fluorescence **3**, 014001 (2015).

[63] M. Müller, V. Mönkemöller, S. Hennig, W. Hübner, and T. Huser, "Open-source image reconstruction of super-resolution structured illumination microscopy data in ImageJ", Nature Communications **7**, 10980 (2016).

[64] A. Lal, C. Shan, and P. Xi, "Structured illumination microscopy image reconstruction algorithm", IEEE Journal of Selected Topics in Quantum Electronics **22**, 50–63 (2016).

[65] L. Jin, B. Liu, F. Zhao, S. Hahn, B. Dong, R. Song, T. C. Elston, Y. Xu, and K. M. Hahn, "Deep learning enables structured illumination microscopy with low light levels and enhanced speed", Nature Communications **11**, 1934 (2020).

[66] E. N. Ward, L. Hecker, C. N. Christensen, J. R. Lamb, M. Lu, L. Mascheroni, C. W. Chung, A. Wang, C. J. Rowlands, G. S. K. Schierle, and C. F. Kaminski, "Machine learning assisted interferometric structured illumination microscopy for dynamic biological imaging", Nature Communications **13**, 7836 (2022).

[67] L. Reymond, R. Griss, A. Schena, B. Mollwitz, K. Bojkowska, A. Masharina, M. A. Brun, D. Maurel, K. Umezawa, G. Lukinavičius, and K. Johnsson, "Visualizing Biochemical Activities in Living Cells through Chemistry", CHIMIA **65**, 868 (2011).

[68] M. J. Rust, M. Bates, and X. Zhuang, "Sub-diffraction-limit imaging by stochastic optical reconstruction microscopy (STORM)", Nature Methods **3**, 793–795 (2006).

[69] F. Aguet, "Super-resolution fluorescence microscopy based on physical models", PhD thesis (EPFL, Lausanne, Apr. 2009).

[70] D. Sage, T.-A. Pham, H. Babcock, T. Lukes, T. Pengo, J. Chao, R. Velmurugan, A. Herbert, A. Agrawal, S. Colabrese, A. Wheeler, A. Archetti, B. Rieger, R. Ober, G. M. Hagen, J.-B. Sibarita, J. Ries, R. Henriques, M. Unser, and S. Holden, "Super-resolution fight club: assessment of 2D and 3D single-molecule localization microscopy software", Nature Methods **16**, 387–395 (2019).

[71] I. M. Khater, I. R. Nabi, and G. Hamarneh, "A Review of Super-Resolution Single-Molecule Localization Microscopy Cluster Analysis and Quantification Methods", Patterns **1**, 100038 (2020).

[72] M. Ovesný, P. Křížek, J. Borkovec, Z. Švindrych, and G. M. Hagen, "ThunderSTORM: A comprehensive ImageJ plug-in for PALM and STORM data analysis and super-resolution imaging", Bioinformatics **30**, 2389–2390 (2014).

[73] D. Sage, H. Kirshner, T. Pengo, N. Stuurman, J. Min, S. Manley, and M. Unser, "Quantitative evaluation of software packages for single-molecule localization microscopy", Nature Methods **12**, 717–724 (2015).

[74] R. E. Thompson, D. R. Larson, and W. W. Webb, "Precise nanometer localization analysis for individual fluorescent probes", Biophysical Journal **82**, 2775–2783 (2002).

[75] K. I. Mortensen, L. S. Churchman, J. A. Spudich, and H. Flyvbjerg, "Optimized localization analysis for single-molecule tracking and super-resolution microscopy", Nature Methods **7**, 377–381 (2010).

[76] R. J. Ober, S. Ram, and E. S. Ward, "Localization Accuracy in Single-Molecule Microscopy", Biophysical Journal **86**, 1185–1200 (2004).

[77] F. Balzarotti, Y. Eilers, K. C. Gwosch, A. H. Gynnå, V. Westphal, F. D. Stefani, J. Elf, and S. W. Hell, "Nanometer resolution imaging and tracking of fluorescent molecules with minimal photon fluxes", Science **355**, 606–612 (2017).

[78] P. Jouchet, C. Cabriel, N. Bourg, M. Bardou, C. Poüs, E. Fort, and S. Lévêque-Fort, "Nanometric axial localization of single fluorescent molecules with modulated excitation", Nature Photonics **15**, 297–304 (2021).

[79] J. Cnossen, T. Hinsdale, R. Thorsen, M. Siemons, F. Schueder, R. Jungmann, C. S. Smith, B. Rieger, and S. Stallinga, "Localization microscopy at doubled precision with patterned illumination", Nature Methods **17**, 59–63 (2020).

[80] M. Schmidt, A. C. Hundahl, H. Flyvbjerg, R. Marie, and K. I. Mortensen, "Camera-based localization microscopy optimized with calibrated structured illumination", Communications Physics **4**, 1–9 (2021).

[81] L. Gu, Y. Li, S. Zhang, Y. Xue, W. Li, D. Li, T. Xu, and W. Ji, "Molecular resolution imaging by repetitive optical selective exposure", Nature Methods, 1–5 (2019).

[82] E. W. Weisstein, *Harmonic Addition Theorem*.

[86] D. Kalisvaart, J. Cnossen, S.-T. Hung, S. Stallinga, M. Verhaegen, and C. S. Smith, "Precision in iterative modulation enhanced single-molecule localization microscopy", Biophysical Journal **121**, 2279–2289 (2022).

[87] Y. Sun, L. Yin, M. Cai, H. Wu, X. Hao, C. Kuang, and X. Liu, "Modulated illumination localization microscopy-enabled sub-10 nm resolution", Journal of Innovative Optical Health Sciences **15**, 2230004 (2022).

[92] C. R. Rao, "Information and accuracy attainable in the estimation of statistical parameters", Bulletin of the Calcutta Mathematical Society **37**, 81–91 (1945).

[97] M. Jansen and G. Claeskens, "Cramér–Rao Inequality", in *International Encyclopedia of Statistical Science*, edited by M. Lovric (Springer Berlin Heidelberg, Berlin, Heidelberg, 2011), pp. 322–323.

[99] J. Chao, E. Sally Ward, and R. J. Ober, "Fisher information theory for parameter estimation in single molecule microscopy: tutorial", Journal of the Optical Society of America A **33**, B36 (2016).

[101] Y. Hiraoka, J. Sedat, and D. Agard, "Determination of three-dimensional imaging properties of a light microscope system. Partial confocal behavior in epifluorescence microscopy", Biophysical Journal **57**, 325–333 (1990).

[102] S. F. Gibson and F. Lanni, "Experimental test of an analytical model of aberration in an oil-immersion objective lens used in three-dimensional light microscopy", Journal of the Optical Society of America A **8**, 1601 (1991).

[103] R. Arimoto and J. M. Murray, "A common aberration with water-immersion objective lenses", Journal of Microscopy **216**, 49–51 (2004).

[104] R. W. Cole, T. Jinadasa, and C. M. Brown, "Measuring and interpreting point spread functions to determine confocal microscope resolution and ensure quality control", Nature Protocols **6**, 1929–1941 (2011).

[105] H. Kirshner, F. Aguet, D. Sage, and M. Unser, "3-D PSF Fitting for Fluorescence Microscopy: Implementation and Localization Application", Journal of Microscopy **249**, 13–25 (2013).

[106] Y. Eilers, H. Ta, K. C. Gwosch, F. Balzarotti, and S. W. Hell, "MINFLUX monitors rapid molecular jumps with superior spatiotemporal resolution.", Proceedings of the National Academy of Sciences of the United States of America **115**, 201801672 (2018).

[107] K. C. Gwosch, J. K. Pape, F. Balzarotti, P. Hoess, J. Ellenberg, J. Ries, and S. W. Hell, "MINFLUX nanoscopy delivers 3D multicolor nanometer resolution in cells", Nature Methods **17**, 217–224 (2020).

[108] L. A. Masullo, F. Steiner, J. Zähringer, L. F. Lopez, J. Bohlen, L. Richter, F. Cole, P. Tinnefeld, and F. D. Stefani, "Pulsed Interleaved MINFLUX", Nano Letters **21**, 840–846 (2021).

[109] M. Reuss, F. Fördős, H. Blom, O. Öktem, B. Högberg, and H. Brismar, "Measuring true localization accuracy in super resolution microscopy with DNA-origami nanostructures", New Journal of Physics **19**, 025013 (2017).

[110] M. Lelek, M. T. Gyparaki, G. Beliu, F. Schueder, J. Griffié, S. Manley, R. Jungmann, M. Sauer, M. Lakadamyali, and C. Zimmer, "Single-molecule localization microscopy", Nature Reviews Methods Primers **1**, 39 (2021).

[111] E. Nehme, L. E. Weiss, T. Michaeli, and Y. Shechtman, "Deep-STORM: super-resolution single-molecule microscopy by deep learning", 10.48550/ARXIV.1801.09631 (2018).

[112] R. F. Laine, G. Goodfellow, L. J. Young, J. Travers, D. Carroll, O. Dibben, H. Bright, and C. F. Kaminski, "Structured illumination microscopy combined with machine learning enables the high throughput analysis and classification of virus structure", eLife **7**, 10.7554/eLife.40183 (2018).

[113] W. Ouyang, A. Aristov, M. Lelek, X. Hao, and C. Zimmer, "Deep learning massively accelerates super-resolution localization microscopy", Nature Biotechnology **36**, 460–468 (2018).

[114] C. N. Christensen, E. N. Ward, P. Lio, and C. F. Kaminski, "ML-SIM: A deep neural network for reconstruction of structured illumination microscopy images", (2020).

[115] A. Speiser, L.-R. Müller, P. Hoess, U. Matti, C. J. Obara, W. R. Legant, A. Kreshuk, J. H. Macke, J. Ries, and S. C. Turaga, "Deep learning enables fast and dense single-molecule localization with high accuracy", Nature Methods **18**, 1082–1090 (2021).

[116] H. Wang, Y. Rivenson, Y. Jin, Z. Wei, R. Gao, H. Günaydın, L. A. Bentolila, C. Kural, and A. Ozcan, "Deep learning enables cross-modality super-resolution in fluorescence microscopy", Nature Methods **16**, 103–110 (2019).

[117]A. E. Ilesanmi and T. O. Ilesanmi, "Methods for image denoising using convolutional neural network: a review", Complex & Intelligent Systems **7**, 2179–2198 (2021).

[118]C. Qiao, D. Li, Y. Liu, S. Zhang, K. Liu, C. Liu, Y. Guo, T. Jiang, C. Fang, N. Li, Y. Zeng, K. He, X. Zhu, J. Lippincott-Schwartz, Q. Dai, and D. Li, "Rationalized deep learning super-resolution microscopy for sustained live imaging of rapid subcellular processes", Nature Biotechnology **41**, 367–377 (2023).

[119]P. Wijesinghe and K. Dholakia, "Emergent physics-informed design of deep learning for microscopy", Journal of Physics: Photonics **3**, 021003 (2021).

[120]S. Cuomo, V. S. Di Cola, F. Giampaolo, G. Rozza, M. Raissi, and F. Piccialli, "Scientific Machine Learning Through Physics–Informed Neural Networks: Where we are and What's Next", Journal of Scientific Computing **92**, 88 (2022).

[122]E. A. K. Cohen, A. V. Abraham, S. Ramakrishnan, and R. J. Ober, "Resolution limit of image analysis algorithms", Nature Communications **10**, 793 (2019).

[123]B. P. Cormack, R. H. Valdivia, and S. Falkow, "FACS-optimized mutants of the green fluorescent protein (GFP)", Gene **173**, 33–38 (1996).

[124]C. Cremer and B. R. Masters, "Resolution enhancement techniques in microscopy", The European Physical Journal H **38**, 281–344 (2013).

[125]S. Dhiman, T. Andrian, B. S. Gonzalez, M. M. E. Tholen, Y. Wang, and L. Albertazzi, "Can super-resolution microscopy become a standard characterization technique for materials chemistry?", Chemical Science **13**, 2152–2166 (2022).

[127]J. M. García-Arcos, J. Ziegler, S. Grigolon, L. Reymond, G. Shajepal, C. J. Cattin, A. Lomakin, D. Müller, V. Ruprecht, S. Wieser, R. Voituriez, and M. Piel, *Advected percolation in the actomyosin cortex drives amoeboid cell motility*, Preprint (Biophysics, July 2022).

[128] J. Ghanam, V. K. Chetty, X. Zhu, X. Liu, M. Gelléri, L. Barthel, D. Reinhardt, C. Cremer, and B. K. Thakur, "Single Molecule Localization Microscopy for Studying Small Extracellular Vesicles", Small, 2205030 (2023).

[130] S. A. Goorden, J. Bertolotti, and A. P. Mosk, "Superpixel-based spatial amplitude and phase modulation using a digital micromirror device", Optics Express **22**, 17999 (2014).

[133] R. Heintzmann, T. M. Jovin, and C. Cremer, "Saturated patterned excitation microscopy—a concept for optical resolution improvement", Journal of the Optical Society of America A **19**, 1599 (2002).

[134] R. Heintzmann, "Answers to fundamental questions in superresolution microscopy", Philosophical Transactions of the Royal Society A: Mathematical, Physical and Engineering Sciences **379**, 20210105 (2021).

[135] D. P. Hoffman and E. Betzig, *Tiled Reconstruction Improves Structured Illumination Microscopy*, Preprint (Cell Biology, Jan. 2020).

[136] F. Huang, T. M. P. Hartwich, F. E. Rivera-Molina, Y. Lin, W. C. Duim, J. J. Long, P. D. Uchil, J. R. Myers, M. A. Baird, W. Mothes, M. W. Davidson, D. Toomre, and J. Bewersdorf, "Video-rate nanoscopy using sCMOS camera–specific single-molecule localization algorithms", Nature Methods **10**, 653–658 (2013).

[137] Y. Li, H. Zhou, X. Liu, C. Xia, and L. Wang, "Correction of dichroic mirror-induced PSF distortion in STED microscopy", Journal of Modern Optics **65**, 1424–1430 (2018).

[138] S. Liu, M. J. Mlodzianoski, Z. Hu, Y. Ren, K. McElmurry, D. M. Suter, and F. Huang, "sCMOS noise-correction algorithm for microscopy images", Nature Methods **14**, 760–761 (2017).

[139] A. Ly, M. Marsman, J. Verhagen, R. Grasman, and E.-J. Wagenmakers, *A Tutorial on Fisher Information*, Oct. 2017.

[140] J. D. Manton, "Answering some questions about structured illumination microscopy", Philosophical Transactions of the Royal Society A: Mathematical, Physical and Engineering Sciences **380**, 20210109 (2022).

[144] M. Renz, "Fluorescence microscopy-A historical and technical perspective: Fluorescence Microscopy", Cytometry Part A **83**, 767–779 (2013).

[145] C. J. Sheppard, "Fundamentals of superresolution", Micron **38**, 165–169 (2007).

[146] F. Ströhl and C. F. Kaminski, "Frontiers in structured illumination microscopy", Optica **3**, 667 (2016).

[147] Y. Sun, "Localization precision of stochastic optical localization nanoscopy using single frames", Journal of Biomedical Optics **18**, 111418 (2013).

[149] L. von Diezmann, Y. Shechtman, and W. E. Moerner, "Three-Dimensional Localization of Single Molecules for Super-Resolution Imaging and Single-Particle Tracking", Chemical Reviews **117**, 7244–7275 (2017).

[152] A. G. York, S. H. Parekh, D. D. Nogare, R. S. Fischer, K. Temprine, M. Mione, A. B. Chitnis, C. A. Combs, and H. Shroff, "Resolution doubling in live, multicellular organisms via multifocal structured illumination microscopy", Nature Methods **9**, 749–754 (2012).

[153] B. Zhang, J. Zerubia, and J.-C. Olivo-Marin, "Gaussian approximations of fluorescence microscope point-spread function models", Applied Optics **46**, 1819 (2007).

Softwares

[141] *Mathematica, Version 13.2*, Wolfram Research, Inc. Champaign, Illinois, 2022.

[142] *MATLAB, Version 9.14.0 (R2023a)*, The MathWorks Inc. Natick, Massachusetts, 2023.